Stimulated Brillouin Scattering based Optical Signal Processing for Fiber-optic Communications and Sensing

WANG, Liang

A Thesis Submitted in Partial Fulfillment
of the Requirements for the Degree of
Doctor of Philosophy
in
Electronic Engineering

The Chinese University of Hong Kong
July 2013

ABSTRACT OF THESIS ENTITLED:

Stimulated Brillouin Scattering based Optical Signal Processing for Fiber-Optic Communications and Sensing

Submitted by: WANG, Liang

for the degree of Doctor of Philosophy in Electronic Engineering

at The Chinese University of Hong Kong in July 2013

Optical signal processing based on fiber nonlinearities plays an important role in both fiber-optic communications and sensing. Among various nonlinear effects, stimulated Brillouin scattering (SBS) in optical fibers has been widely employed not only in processing of high-speed communication signals, but also in constructing fiber-optic sensors. This thesis investigates new techniques of optical signal processing based on SBS for fiber-optic communications and sensing.

In the recent years, slow light has attracted considerable interest because of its numerous applications, in realizing variable true time delay and in optical information processing. Among various slow light mechanisms, the SBS based slow light shows great potential in all-optical signal processing due to the advantages of room-temperature operation and device compatibility with existing fiber systems. However, owing to the tight requirement of spectral alignment between the SBS pump and the signal, most of the published works are for the case where one SBS pump is used to delay a single channel. Hence, only one delayed channel is obtained. In this thesis, we demonstrate a technique to simultaneously generate multiple delayed signals through four-wave mixing (FWM) wavelength multicasting in a single-pump stimulated Brillouin scattering (SBS) based slow light system. The signal delay is achieved with a SBS pump while at the same time the delay is transferred to six other channels by three FWM pumps employed for wavelength multicasting. This slow light multicasting technique may find applications in parallel optical information processing such as simultaneous multichannel synchronization and time division multiplexing.

Fiber-optic sensor techniques provide a promising approach for structure health monitoring, especially the temperature and strain monitoring. The technique based on Brillouin scattering has attracted much interest in the past two decades because Brillouin fiber sensors offer advantages of high resolution, long distance sensing, and large sensing range. In the thesis, we propose and experimentally demonstrate a new method for temperature/strain sensing using stimulated Brillouin scattering based slow light. The approach relies on temperature/strain dependence of the Brillouin frequency shift in a fiber, hence the time delay of an input probe pulse. By measuring the delay, temperature/strain sensing can be realized. We achieve temperature measurement for both a 100 m single mode fiber (SMF) and a 2 m SMF. Distributed temperature/strain sensing has been demonstrated later. The temperature/strain of a particular fiber section can be monitored by setting an appropriate relative delay between the pump and probe pulses. By controlling the relative delay, we have achieved distributed profiling of the temperature/strain along the whole sensing fiber. Compared to conventional Brillouin fiber sensors, our scheme has the merits of more straightforward implementation, fast response and potential of real-time monitoring.

Wavelength conversion plays an important role in wavelength routing and switching. Among various schemes for wavelength conversion, the one based on FWM is superior as it offers advantages in being transparent to modulation formats, bit-rates, and communication protocols. However, significant FWM can occur only if the phase velocities of the interplaying waves are matched. The matching condition can hardly be satisfied over a wide spectral range and hence the conversion bandwidth is often limited. In this thesis, we propose and experimentally demonstrate an approach to dynamically control the FWM phase matching condition by using gain-transparent SBS. By introducing self-compensation of optical gain/loss with SBS pump and Stokes waves, the FWM phase matching condition can be flexibly controlled through SBS induced refractive index change without affecting the initial parameters of the FWM. The gain-transparent scheme is employed to enlarge the degenerate FWM conversion bandwidth, enhance the performance in wavelength conversion of communication signals, all-optically manipulate non-degenerate FWM conversion bandwidth, achieve both polarization-insensitive and wideband operation in a dual orthogonal pump wavelength converter, and extend the maximum optical delay of a delay line based on FWM wavelength conversion and dispersion.

Low noise and broadband amplification are possible by using optical parametric processes. Although fiber-optic parametric amplifier (FOPA) can provide gain as high as 70 dB, its operation is often confined by phase mismatch of the interplaying fields. In this thesis, we apply gain-transparent SBS to a FOPA and dynamically control its gain profile. The conventional “M” shape gain profile can be dynamically changed. Flattening of the gain profile to within 0.1 dB variation has been achieved.

摘要

基於光纖非線性效應的光學信號處理在光纖通信和傳感中起著重要作用。在各種非線性效應中，光纖中的布里淵散射不僅被廣泛應用於高速通信信號的處理，而且被用於建立光纖傳感器。本文研究基於布里淵散射的光學信號處理新技術在光通信和傳感中的應用。

近年來由於慢光技術在實現時間延遲和光學信號處理中的廣泛應用，它吸引了廣泛的注意力。 在各種實現慢光的技術中，基於布里淵散射的慢光技術展示了很大的潛力，因為它具有在常溫工作以及與現有光纖系統兼容的優勢。但是由於布里淵泵浦和信號之間嚴格的頻率要求，大多數的研究工作是建立於一個泵浦延遲一個信號的基礎上，所以只能獲得一個被延遲的信道。本文提出了一種在一個布里淵泵浦的慢光系統中實現同時產生多個延遲信號的技術。這種技術應用了基於四波混頻的廣播效應。輸入信號被布里淵泵浦延遲的同時，延遲通過三個四波混頻泵浦的廣播效應傳遞給其他六個新產生的信道。這種慢光廣播技術可以被應用於並行光學信號處理，比如實現多信道同步以及時分複用。

光纖傳感技術為結構的健康提供了一種優秀的監測方法，尤其是溫度和應力的監測。在過去的二十年間，基於布里淵散射的傳感技術吸引了大批人的興趣，因為布里淵光纖傳感器擁有高分辨率，長距離監測以及監測範圍廣的優點。本文提出了一種新的基於布里淵慢光的溫度和應力傳感技術。布里淵頻移的溫度和應力相關性使得輸入光脈衝的延遲也與溫度和應力相關，因此我們通過測量這個延遲來監測溫度和應力。我們分別實現了對 100 米和 2 米單模光纖的溫度

測量。隨後我們也實現了分佈式溫度和應力監測。通過設置泵浦和探測光脉衝之間的延遲時間，我們可以監測特定位置的光纖。因此，通過控制整個延遲時間，我們實現了對整個光纖的溫度和應力分佈的監測。相比于普通的布里淵光纖傳感器，我們這種技術擁有以下優點：更加直接簡單的實現監測，快速的反應時間以及實時監測的潛力。

波長轉換在路由和交換中起了很重要的作用。在各種波長轉換的技術中，基於四波混頻的波長轉換非常優越因為它具有對調製格式，比特率以及通信協議透明的優點。但是，四波混頻只有在各個光波的相速度匹配的情況下才能有效的產生。這種匹配條件很難在一個很寬的頻段內保持，因此四波混頻的轉換帶寬是很有限的。本文提出了一種基於零增益受激布里淵散射的方法來動態地控制四波混頻的相位匹配。 通過布里淵泵浦和斯托克斯光引入自我補償的受激布里淵增益和損耗，四波混頻的相位匹配條件可以被受激布里淵散射激發的折射率改變來靈活的控制，並且不會影響四波混頻初始的參數。我們把這種零增益受激布里淵散射應用于增大簡並四波混頻的帶寬，增強通信信息波長轉換的效果，全光調控非簡並四波混頻的帶寬，實現偏振不敏感寬帶波長轉換以及延長基於四波混頻波長轉換和色散的延遲線的最大延遲時間。

低噪聲寬帶放大可以通過光學參量過程來實現。雖然光參量放大器可以提供高至 70 分貝的增益，但是這種參量放大器經常受限於各個光波的相位不匹配。在本文中，我們把零增益受激布里淵散射用於光參量放大器來動態的控制它的增益譜。基於這種技術，我們動態地改變了傳統的“M”型增益譜，並且由此得到了非常平滑的增益譜，增益的變換量僅僅在 0.1 分貝以內。

ACKNOWLEDGEMENT

I want to take this opportunity to thank those who have helped me in my life and research during my four-year study in The Chinese University of Hong Kong.

I would like to express my greatest gratitude to my supervisor, Prof. Chester Shu, who has trained me to be a good researcher during the past 4-year PhD study. His expertise and research insight greatly benefit me in the field of fiber-optics. He has taught me how to think about problems and find ways in solving them as a PhD student. He guided me to design the experiment, analyze the experimental data, and helped me improve my skills in writing scientific papers. His useful suggestions always make me out of confusion and his kindness always encourage me to overcome the obstacles in both research and life. I really appreciate his great support to my research activities in the past 4 years. These activities are not only important in my research, but also be valuable in my future life.

I would like to thank Prof. Kam Tai Chan and Prof. Hon Ki Tsang, for their support and the running of the laboratory with well-equipped facility and harmonic atmosphere. I want to thank Ms. Lai Ching Ho, for her kind instructions on equipment use and lab safety, and her regulations of our lab.

I also thank Prof. Hon Ki Tsang, Prof. Lian Kuan Chen and Prof. Kin Seng Chiang to be my PhD defense committee.

I am very thankful to Prof. Sailing He in Zhejiang University for his helpful discussion on my sensor project. Thanks also go to Dr. Bin Zhou, who was a PhD student of Prof. Sailing He and an exchange student in our lab. He provided valuable suggestions on our fiber sensor project, and collaborated with me to design the experiment, analyze the data and write the paper.

I am also grateful to Dr. Kin Pang Lei, Dr. Yongheng Dai and Dr. Jiangbin Du. They taught me how to operate experiment equipments and discussed with me on my research topics, my experiment and my life in Hong Kong. I also appreciate Mr. Zhenzhou Cheng, Mr. Ke Xu and Mr Yimin Chen who shared with me a lot about research and life in Hong Kong and what to do next in future.

I also like to thank everyone in Opto Lab, Dr. Kejian Chen, Dr. Caiming Sun, Dr. Chao Li, Dr. Hao He, Dr. Lin Xu, Dr. Xia Chen, Dr. Zhongxiang Zhang, Mr. Chiyan Wong, Mr. Minggai Lo, Ms. Mengyu Chen, Ms. Christy Fung, Ms. Xuelei Fu, Ms. Xiaojie Guo, Ms. Zerui Shi, Ms. Jingjing Liu, Mr. Zili Ma, Mr. Bofang Zheng, Ms. Chaoran Huang, Ms. Jiaqi Wang, Ms. Bingqing Zhu, who have established a wonderful atmosphere during my four years in the lab.

My thanks are also reserved for Prof. Mable P. Fok in University of Georgia, Prof. Nan Chi in Fudan University, Prof. Minglie Hu in Tianjin University and Prof. Ming Tang in Huazhong University of Science and Technology, who offered helpful suggestions to me not only on my research, but also on my future career.

Finally, I would like to express my special thanks to my family. Thank you for providing me with a harmonious environment and giving me so much love. Thank you for giving me all your support to finish my college and my PhD study. Thank you for making my world a better place to be and witnessing each step of my growth. You have all my honors.

Thank you all !

TABLE OF CONTENT

Stimulated Brillouin Scattering based Optical Signal Processing for Fiber-Optic Communications and Sensing

1 INTRODUCTION

Since the invention of low-loss silica fibers in 1970s, the development of fiber-optics has prompted a revolution in both optical fiber communications and sensing. Optical fibers have the advantages of low transmission loss, enormous bandwidth, electrical isolation, and immunity to electromagnetic interference. The advantages make optical fibers be an excellent transmission medium for high-speed communication signals and remote sensing signals. Nowadays most of the backbone architectures in communication networks and sensing networks are made up of optical fibers, which establish huge fiber-optic networks covering our planet.

As the continuous growth of technology in laser sources, fiber fabrication and receiver design, the way of signal transmission through optical fibers changes from single wavelength to wavelength division multiplexing, from inefficient mechanism of time usage to time division multiplexing, and from single format transmission to mixed formats transmission, etc. All of these changes lead to the increasing transmission speed per channel from hundreds of Mbit/s to over 10 Tb/s [1, 2]. With the increasing transmission speed, the processing of the optical signal becomes more difficult and complicated. At low transmission speed, the optical signal is usually converted to electrical signal and then back to optical signal after electrical signal processing. This is the so called O/E/O conversion. However, at high transmission speed the electrical signal processing reaches its limits as it relies on the mobility of electrons in semiconductor materials. To overcome the bottleneck of electrical signal processing, all optical signal processing based on optic-electric effects or nonlinear optical effects, which exploits photons propagating with the speed of light and directly processes the optical signal, provides a power-efficient way of processing high speed signal without O/E/O conversion. The optical signal processing have the potential to operate in the femtosecond (10^{-15} s) time domain [3] and thus the processing speed is far beyond the limitation of electronic devices. Therefore, optical signal processing would be a desirable candidate for future high-speed fiber-optic networks. This thesis focuses on innovative all-optical signal processing techniques mainly based on stimulated Brillouin scattering effect in optical fibers for fiber-optic networks. In this chapter, an overview of optical signal processing is given in section 1.1, and then the thesis outline is described in section 1.2.

1.1 Overview of Optical Signal Processing

Stimulated by the development of optical fiber technologies, a variety of optical devices have been developed rapidly. Among which are semiconductor lasers, photodetectors, semiconductor optical amplifiers (SOAs), optical modulators, switches, filters and so on. Besides the above devices, optical fiber itself is also found to be a good material of optical components, e.g. fiber amplifiers, lasers, interferometers, nonlinear element, etc. The emergence of various new optical devices and components makes the optical signal processing more easier and prosperous for both optical communications and sensing.

Most of the widely used optical signal processing methods are based on nonlinear optical effects in fiber-based or non-fiber-based devices. Among non-fiber-based devices, SOAs are popular in processing optical signals. As an example, to deal with the rapid growth of traffic in optical networks, the function of optical switching for the routing of the optical signal is often achieved by wavelength conversion using the cross-phase modulation (XPM), cross-gain modulation (XGM) and four-wave mixing (FWM) effects in SOAs [4-6]. Although SOAs may suffer from the relatively slow response, their advantages of compact size and compatibility for integration with other devices make them suitable for the design of large scale photonic circuits and implementation of complicated functions. Meanwhile, several techniques have also been developed to improve the speed performance of the SOAs [7-10].

Compared with the slow response time in SOAs, the nonlinear effects in optical fibers are instant, which is good for ultrafast processing of high-speed optical signal.

The nonlinear effects in optical fibers can be roughly classified into two categories: elastic and inelastic nonlinear effects. The elastic nonlinear effects are governed by the third-order susceptibility $\chi^{(3)}$, where no energy is exchanged between the electromagnetic field and the dielectric medium [11]. The nonlinear effects in this category include self-phase modulation (SPM), XPM, FWM, third-harmonic generation and so on. The second class of nonlinear effects originates from stimulated inelastic scattering in which the optical field has energy transfer to the nonlinear medium [11]. Two major nonlinear effects in optical fibers fall in this category: stimulated Raman scattering (SRS) and stimulated Brillouin scattering (SBS). Examples of the applications of fiber nonlinearities in fiber-optic communications are wavelength conversion [12, 13], multicasting [15, 16], multiplexing [17], regeneration [18], clock recovery [19], format conversion [20], slow light [21, 22] and so on. On the other hand, in the field of optical sensing, Raman and Brillouin scattering in optical fibers have been used to implement distributed temperature and strain sensing [23, 24]. Especially the Brillouin scattering based optical sensing techniques have attracted more and more attention in recent years. Various configurations and schemes are developed to satisfy different requirements, such as Brillouin optical time-domain analysis (BOTDA) [25], Brillouin optical frequency-domain analysis (BOFDA) [26] and Brillouin optical correlation-domain analysis (BOCDA) [27], etc.

As the fiber nonlinearity plays important role in optical signal processing, design of optical fibers with high nonlinear coefficient is essential to improve the processing performance. Conventional single-mode fibers (SMFs) have a relatively small nonlinear coefficient of ~ 2/(W·km) at 1550 nm [11], thus a length of several kilometers is usually required to introduce significant nonlinearity. But using such a long fiber to process optical signals will have serious limitations due to the practical issues of the size and stability of the setup. To shorten the fiber length, highly nonlinear fiber (HNLF) with a smaller effective mode field diameter, and hence, a larger nonlinear coefficient of ~ 10/(W·km) has been designed [28]. Therefore, 1 km length is usually enough to offer sufficient nonlinearity for optical signal processing. Although the use of HNLF largely reduces the fiber length, 1 km length is still very long and it suffers from low SBS threshold due to its high nonlinearity and still long length. To overcome the restriction, tailoring either the fiber structure or the material or a combination of both is a good way of achieving large nonlinearity in a very short fiber, such as silica-based photonic crystal fibers [29, 30], highly nonlinear bismuth oxide fiber [31] and so on. These specially designed fibers offer a convenient and practical solution to optical signal processing.

1.2 Outline of the Thesis

The thesis research focuses on development of all-optical signal processing techniques for optical communications and sensing, mainly based on the effect of stimulated Brillouin scattering in optical fibers. In Chapter 1, an overview of optical signal processing is given. The all-optical processing techniques provide a way of processing optical signals in optical domain and remove the constraint of O/E/O conversion, which largely improve the processing speed and contribute to the future all-optical networking. In Chapter 2, physical mechanism of stimulated Brillouin scattering (SBS) in optical fibers has been introduced, together with the coupled equations governing the phenomenon under steady-state conditions, the Brillouin gain and the threshold of Brillouin scattering in optical fibers.

Slow light in nonlinear media has attracted considerable interest because of its numerous applications in optical signal processing. Using fibers to achieve slow light offers the advantages of room-temperature operation and device compatibility with existing fiber systems. Among various slow light mechanisms, the SBS based slow light attracts lots of attention. In Chapter 3, a technique to simultaneously generate multiple delayed signals through four-wave mixing wavelength multicasting in a single-pump SBS based slow light system is demonstrated. The signal delay is achieved with a SBS pump while at the same time the delay is transferred to six other channels by three FWM pumps employed for wavelength multicasting. The delay performances of all output channels are analyzed. Relationship of the delay between the original signal and the multicast outputs is investigated and verified experimentally.

Fiber-optic sensor is an excellent candidate for the monitoring of temperature and strain over long distances. In particular, Brillouin fiber sensors have attracted much interest in the past two decades, as these conventional fiber sensors provide advantages of high resolution, long distance sensing, and large sensing range. In Chapter 4, we associate SBS based slow light with temperature sensing for the first time, and demonstrate a new method for temperature sensing using SBS based slow light. The temperature sensing are achieved in both long and short fiber segments using different pump configurations. The temperature resolution is analyzed using the simulation and experimental results. The scheme offers more straightforward implementation using an oscilloscope for the detection with fast response time, and is potentially applicable for distributed sensing.

Distributed fiber-optic sensors provide an efficient way of simultaneously achieving multi-points sensing by a convenient and low-cost configuration. Among the different types of distributed fiber-optic sensors, distributed Brillouin fiber sensors have attracted much research interest and are now widely used in structural health monitoring. Chapter 5 extends the research work discussed in Chapter 4. In this chapter, distributed temperature and strain sensing have been achieved by spatially resolved measurement of the probe time delay resulted from SBS based slow light. The temperature or strain of a particular fiber section can be monitored by setting an appropriate relative delay between the pump and probe pulses. A spatial resolution of 15 m and a temperature (strain) resolution of 0.7 ^{o}C (13 $\mu\varepsilon$) are obtained. Suggestions for the enhancement of the spatial, temperature and strain resolutions are also discussed. This scheme provides an alternative way for distributed temperature or strain sensing with the potential of real-time temperature or strain monitoring.

All-optical wavelength conversion is considered as a key functionality in future wavelength division multiplexing (WDM) networks. Four-wave mixing (FWM) based wavelength converter is considered as one of the most promising wavelength converters since it offers unique advantages in being transparent to modulation formats, bit-rates, and communication protocols. In Chapter 6, we address the problem of phase matching in FWM wavelength conversion with the use of gain-transparent SBS for phase control. The phase matching of FWM can be dynamically controlled by the SBS induced phase mismatch without affecting the initial parameters of the FWM due to the gain-transparent scheme. The resulted achievements based on this scheme include enlargement of degenerate FWM conversion bandwidth, enhanced performance in wavelength conversion of communication signals, all-optical manipulation of non-degenerate FWM conversion bandwidth, simultaneously polarization-insensitive and wideband wavelength conversion in a dual orthogonal pump wavelength converter, and the extension of the maximum optical delay of a delay line based on FWM wavelength conversion and dispersion. Besides these achievements, limitations of this scheme and noise performance are also discussed. Potential use of the scheme in other applications is described as well.

Compared to erbium-doped fiber amplifier (EDFA), fiber optical parametric amplifier (FOPA) offers low-noise amplification and large gain over a wide spectral range. However, its gain performance is often limited by phase mismatch of the interplaying fields. In certain applications, a flexible gain profile in a FOPA can be desirable such that one may choose the optimal profile according to the specific requirements. Chapter 7 addresses the phase matching in a single-pump FOPA. We use gain-transparent SBS to control the relative phase difference among the interacting fields, and achieve dynamic gain profiles in a FOPA. The scheme offers operational flexibility in randomly synthesizing the profile to satisfy different requirements and can benefit other applications of parametric processes.

Finally a summary of the thesis is given in Chapter 8, and suggested future work for improvement of the investigated techniques is also covered in this chapter.

References

[1] T. Richter, E. Palushani, C. Schmidt-Langhorst, M. Nölle, R. Ludwig, and C. Schubert, "Single wavelength channel 10.2 Tb/s TDM-data capacity using 16-QAM and coherent detection," in Proc. OFC/NFOEC 2011, Los Angeles, paper PDPA9.

[2] J. Sakaguchi, Y. Awaji, N. Wada, A. Kanno, T. Kawanishi, T. Hayashi, T. Taru, T. Kobayashi, and M. Watanabe, "109-Tb/s (7x97x172-Gb/s SDM/WDM/PDM) QPSK transmission through 16.8-km homogeneous multi-core fiber," in Proc. of OFC/NFOEC 2011, Los Angeles, paper PDPB6.

[3] T. Schneider, *Nonlinear Optics in Telecommunications*, Springer, 2004.

[4] J. Leuthold, C.H. Joyner, B. Mikkelsen, G. Raybon, J.L. Pleumeekers, B.I. Miller, K. Dreyer and C.A. Burrus, "100 Gbit/s all-optical wavelenth conversion with integrated SOA delayed-interference configuration," Electron. Lett., vol. 36, no. 13, pp. 1129 – 1131, June 2000.

[5] M. Matsuura, O. Raz, F. G. Agis, N. Calabretta, and J. S. Dorren, "320-Gb/s wavelength conversion based on cross-gain modulation in a quantum-dot SOA," in Proc. of ECOC 2011, Geneva, paper Mo.1.A.1.

[6] M. Matsuura, and N. Kishi, "High-Speed Wavelength Conversion of RZ-DPSK Signal Using FWM in a Quantum-Dot SOA," IEEE Photon. Technol. Lett., vol. 23, no. 10, pp. 615 – 617, May 2011.

[7] S. Bischoff, M. L. Nielsen, and J. Mørk, "Improving the All-Optical Response of SOAs Using a Modulated Holding Signal," IEEE J. Lightw. Technol., vol. 22, no.5, pp. 1303 – 1308, May 2004.

[8] R. Giller, R. J. Manning, and D. Cotter, “Gain and Phase Recovery of Optically Excited Semiconductor Optical Amplifiers,” IEEE Photon. Technol. Lett., vol. 18, no. 9, pp.1061 – 1067, January 2006.

[9] E. Tangdiongga, Y. Liu, H. de Waardt, G. D. Khoe, and H. J. S. Dorren, “320-to-40-Gb/s Demultiplexing Using a Single SOA Assisted by an Optical Filter,” IEEE Photon. Technol. Lett., vol. 18, no. 8, pp. 908 – 910, April 2006.

[10] Y. Liu, E. Tangdiongga, Z. Li, S. Zhang, H. Waardt, G. D. Khoe, and H. J. S. Dorren, “Error-Free All-Optical Wavelength Conversion at 160 Gb/s Using a Semiconductor Optical Amplifier and an Optical Bandpass Filter,” IEEE J. Lightw. Technol., vol. 24, no.1, pp. 230 – 236, January 2006.

[11] G. P. Agrawal, *Nonlinear Fiber Optics*, The Netherlands: Elsevier, Amsterdam, 2009.

[12] A.-L. Yi, L.-S. Yan, B. Luo, W. Pan, and J. Ye, “Wavelength Conversion of RZ-OOK PDM Signals Based on XPM in Highly Nonlinear Fiber,” IEEE Photon. Technol. Lett., vol. 23, no. 6, pp. 341 – 343, March 2011.

[13] Md. Nur-Al-Safa Bhuiyan, M. Matsuura, H. N. Tan, and N. Kishi, “Polarization-insensitive and widely tunable wavelength conversion for polarization shift keying signal based on four wave mixing in highly non-linear fiber,” Opt. Express., vol. 18, no. 3, pp. 2467 – 2476, February 2010.

[14] M. P. Fok, and C. Shu, “Multipump Four-Wave Mixing in a Photonic Crystal Fiber for 6 × 10 Gb/s Wavelength Multicasting of DPSK Signals,” IEEE Photon. Technol. Lett., vol. 19, no. 15, pp. 1166 – 1168, August 2007.

[15] Guo-Wei Lu, K. S. Abedin, and T. Miyazaki, “DPSK multicast using multiple-pump FWM in Bismuths highly nonlinear fiber with high

[16] multicast efficiency," Opt. Express., vol. 16, no. 26, pp. 21964 – 21970, December 2008.

[17] X. Wu,1, J. Wang, O. F. Yilmaz, S. R. Nuccio, A. Bogoni, and A. E. Willner, "Bit-rate-variable and order-switchable optical multiplexing of high-speed pseudorandom bit sequence using optical delays," Opt. Lett., vol. 35, no. 18, pp. 3042 – 3044, September 2010.

[18] R. Slavík, F. Parmigiani, J. Kakande, C. Lundström, M. Sjödin, P. A. Andrekson, R. Weerasuriya, S. Sygletos, A. D. Ellis, L. Grüner-Nielsen, D. Jakobsen, S. Herstrøm, R. Phelan, J. O'Gorman, A. Bogris, D. Syvridis, S. Dasgupta, P. Petropoulos, and D. J. Richardson, "All-optical phase and amplitude regenerator for next-generation telecommunications systems," Nature Photon., vol. 4, pp. 690–695, October 2010.

[19] J. Li, T. Huang, and L. R. Chen, "Detailed Analysis of All-Optical Clock Recovery at 10 Gb/s Based on a Fiber Optical Parametric Oscillator," IEEE J. Sel. Topics Quantum Electron., vol. 18, no. 2, pp. 701 – 708, March/April 2012.

[20] L. Wang, Y. Dai, K. P. Lei, J. Du, and C. Shu, "All-Optical RZ-to-NRZ and NRZ-to-PRZ Format Conversions Based on Delay-Asymmetric Nonlinear Loop Mirror," IEEE Photon. Technol. Lett., vol. 23, no. 6, pp. 368 – 370, March 2011.

[21] Y. Okawachi, M. S. Bigelow, J. E. Sharping, Z. Zhu, A. Schweinsberg, D. J. Gauthier, R. W. Boyd, and A. L. Gaeta, "Tunable All-Optical Delays via Brillouin Slow Light in an Optical Fiber," Phys. Rev. Lett., vol. 94, 153902, April 2005.

[22] K. Y. Song, M. G. Herráez, and L. Thévenaz, “Observation of pulse delaying and advancement in optical fibers using stimulated Brillouin scattering,” Opt. Express., vol. 13, no. 1, pp. 82-88, January 2005.

[23] M. A. Farahani and T. Gogolla, “Spontaneous Raman Scattering in Optical Fibers with Modulated Probe Light for Distributed Temperature Raman Remote Sensing,” IEEE J. Lightw. Technol., vol. 17, no. 8, pp. 1379 – 1391, August 1999.

[24] S. M. Maughan, H. H. Kee, and T. P. Newson, “57-km single-ended spontaneous Brillouin-based distributed fiber temperature sensor using microwave coherent detection,” Opt. Lett., vol. 26, no. 6, pp. 331 – 333, March 2001.

[25] H. Liang, W. Li, N. Linze, L. Chen, and X. Bao, “High-resolution DPP-BOTDA over 50 km LEAF using return-to-zero coded pulses,” Opt. Lett., vol. 35, no. 10, pp. 1503 – 1505, May 2010.

[26] R. Bernini, A. Minardo, and L. Zeni, “Stimulated Brillouin scattering frequency-domain analysis in a single-mode optical fiber for distributed sensing,” Opt. Lett., vol. 29, no. 17, pp. 331 – 333, September 2004.

[27] M. Belal, and T. P. Newson, “Enhanced Performance of a Temperature-Compensated Submeter Spatial Resolution Distributed Strain Sensor,” IEEE Photon. Technol. Lett., vol. 22, no. 23, pp. 1705 – 1707, December 2010.

[28] G. Berrettini, G. Meloni, A. Bogoni, and L. Poti, “All-Optical 2 × 2 switch based on Kerr effect in highly nonlinear fiber for ultrafast applications,” IEEE Photon. Technol. Lett., vol. 18, no. 23, pp. 2439 – 2441, December 2006.

[29] P. S. J. Russell, “Photonic-crystal fibers,” IEEE J. Lightw. Technol., vol. 24, no. 12, pp. 4729 – 4749, December 2006.

[30] K. K. Chow, C. Shu, C. Lin, and A. Bjarklev, “Polarization-insensitive widely tunable wavelength converter based on four-wave mixing in a dispersion-flattened nonlinear photonic Crystal fiber,” IEEE Photon. Technol. Lett., vol. 17, no. 3, pp. 624 – 626, March 2005.

[31] M. P. Fok, and C. Shu, “Recent Advances in Optical Processing Techniques Using Highly Nonlinear Bismuth Oxide Fiber,” IEEE J. Sel. Topics Quantum Electron., vol. 14, no. 3, pp. 587 – 598, May/June 2008.

2 STIMULATED BRILLOUIN SCATTERING IN OPTICAL FIBERS

The French scientist Leon Brillouin first investigated the scattering of light by acoustic waves in the 1920s, since then this scattering effect was named after him. Brillouin scattering has not attracted much attention until the invention of laser sources in 1960s, as strong scattered fields usually require high intensity light sources. Later, with the development of optical fiber technologies, Brillouin scattering has been intensively studied in optical fibers for its use in optical signal processing. At the same time, despite its wide applications in fiber-optic networks, the impairments of Brillouin scattering on communication and sensing systems have also been investigated.

In this chapter, the physical mechanism of Brillouin scattering is presented first in section 2.1, then the stimulated Brillouin scattering under steady-state conditions is discussed in section 2.2. The characteristics of Brillouin gain and corresponding threshold are introduced in section 2.3 and 2.4, respectively. The last section shows applications of Brillouin scattering and its impact on fiber-optic networks.

2.1 Physical Process of Brillouin Scattering

Brillouin scattering is a result of interaction between the incident light field and the optical medium. The incident pump light induces density fluctuations of the optical medium which is responsible for the scattering. The density fluctuations propagate along the medium with the speed of sound, and can be seen as acoustic waves or phonons [1]. The periodic density modulation will in turn modulate the refractive index of the optical medium. This pump-induced index grating scatters the incident pump light through Bragg diffraction, as shown in Fig. 2.1 (a). As the density modulation moves at the acoustic velocity, the scattered wave (Stokes wave) experiences a frequency shift due to the Doppler effect. In the field of quantum mechanics, the same scattering process can be described as follows: a photon is annihilated and simultaneously a new photon with a downshifted frequency and a phonon are created, as shown in Fig. 2.1 (b). During the whole scattering process, both the energy and momentum must be conserved, thus the frequencies and the wave vectors of the pump, Stokes and acoustic waves are related by

$$\Omega_B = \omega_p - \omega_s \tag{2-1}$$

$$\overrightarrow{k_A} = \overrightarrow{k_p} - \overrightarrow{k_s} \tag{2-2}$$

where ω_p, ω_s and Ω_B are the frequencies, and $\mathbf{k_p}$, $\mathbf{k_s}$ and $\mathbf{k_A}$ are the wave vectors, of the pump, Stokes and acoustic waves, respectively. As the frequency of the acoustic wave is much smaller than the frequency of the pump wave, it is reasonable to assume that the magnitudes of the wave vectors for the pump and the Stokes wave are approximately equal ($|\mathbf{k_p}| \approx |\mathbf{k_s}|$). According to the vector diagram in Fig. 2.1 (a), the magnitude of the wave vector of the acoustic wave is

$$\left|\overrightarrow{k_A}\right| \approx 2\left|\overrightarrow{k_p}\right| \sin\frac{\theta}{2} \tag{2-3}$$

in which θ is the angle between the pump and Stokes waves. On the other hand, $|\mathbf{k_A}|=\Omega_B/v_A$ and $|\mathbf{k_p}|=2\pi n_p/\lambda_p$, v_A is the acoustic velocity, λ_p is the pump wavelength and n_p is the effective mode index at the pump wavelength. Thus the acoustic frequency is

$$\Omega_B = 2\pi\frac{2v_A n_p}{\lambda_p}\sin\frac{\theta}{2} \tag{2-4}$$

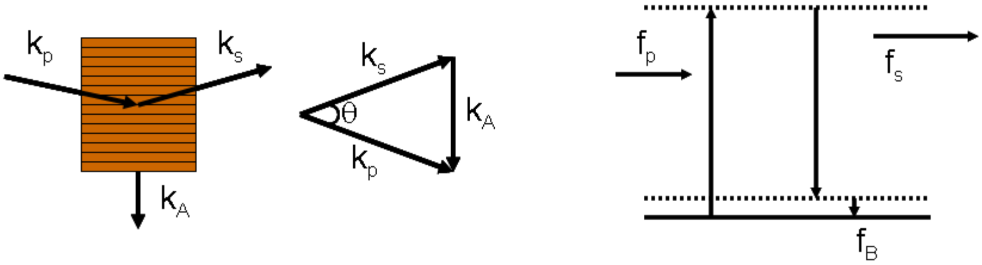

Fig. 2.1. (a) Scattering by an index grating moving at the acoustic velocity and corresponding vector diagram; (b) quantum mechanical model of Brillouin scattering.

Equation (2-4) shows that the frequency shift of the Stokes wave is related to the scattering angle. And Ω_B becomes maximum in the backward direction (θ=π) and is zero in the forward direction (θ=0). In a single-mode optical fiber, there are only relevant forward and backward directions. For this reason, SBS occurs only in the backward direction and hence the Brillouin frequency shift is

$$\nu_B = \frac{\Omega_B}{2\pi} = \frac{2v_A n_p}{\lambda_p} \tag{2-5}$$

To obtain a quantitative view of Brillouin frequency shift, we use v_A=5.96 km/s and n_p=1.45 for silica fibers, then $\nu_B \approx$11.1 GHz at λ_p=1.55 μm. Note that forward Brillouin scattering will also happen in specially designed fiber, e.g. holey fibers [2].

2.2 Stimulated Brillouin Scattering Under Steady-State Conditions

If the incident pump light is so weak that the optical properties of the material system are not altered, the scattering process is caused by the density fluctuations mainly resulting from the thermal motions of the material molecules. This scattering process is named as spontaneous Brillouin scattering [1]. In spontaneous scattering regime, the amount of scattering is proportional to the intensity of the incident pump light. Hence it is always very weak. On the other hand, if the pump light is high such that the fluctuations are strongly excited and the power transfer to the Stokes wave increases in an exponential way, a stimulated scattering process occurs, which is the stimulated Brillouin scattering (SBS). In this section, we mainly talk about the SBS and its characteristics under steady-state conditions.

Under steady-state conditions, SBS is governed by the following two coupled equations [3]:

$$\frac{dI_p}{dz} = -g_B I_s I_p - \alpha I_p \tag{2-6}$$

$$-\frac{dI_s}{dz} = g_B I_p I_s - \alpha I_s \tag{2-7}$$

where g_B is the Brillouin gain coefficient, α is the fiber loss, I_p and I_s are the intensities of the pump and Stokes waves, respectively. Two simplifications are made to obtain Equations (2-6) and (2-7): $\omega_p \approx \omega_s$ due to the fact that the Brillouin frequency shift is too small compared to the frequencies of the pump and Stokes waves, and for the same reason, $\alpha_p \approx \alpha_s$ meaning fiber losses are nearly the same for the pump and

Stokes waves. The negative sign at the left side of Equation (2-7) indicates that the Stokes wave is counterpropagating with the pump wave. Note that the two equations assume implicitly that the pump and Stokes waves are co-polarized and maintain their states of polarization along the fiber, i.e. when the two waves are polarized along one principal axis of a polarization-maintaining fiber. For the case where the pump intensity is not high, the pump depletion can be neglected. Thus the first term in Equation (2-6) disappears and the pump intensity is only determined by the fiber loss:

$$I_p(z) = I_p(0)e^{-\alpha z} \tag{2-8}$$

Taking Equation (2-8) into Equation (2-7) and integrating it over the fiber length L, the intensity of the Stokes wave is found to be

$$I_s(0) = I_s(L)\exp(g_B P_0 L_{eff} / A_{eff} - \alpha L) \tag{2-9}$$

in which A_{eff} is the effective core area of the fiber, $P_0=I_p(0)A_{eff}$ is the input pump power, and L_{eff} is the effective fiber length defined as $L_{eff}=(1-e^{-\alpha L})/\alpha$. Equation (2-9) shows how a Stokes wave incident at $z=L$ grows exponentially in the backward direction due to energy transfer from the pump wave, which originates from the Brillouin scattering. In practice, unless the fiber is used as a Brillouin amplifier where a signal is fed, the Stokes wave grows from the noise provided by the spontaneous Brillouin scattering. The noise power can be viewed as injection of a fictitious photon per mode at a distance where the gain exactly compensates the fiber loss [3]. Fig. 2.2 also plots the exponential amplification of the Stokes wave along the fiber using Equation (2-9). Typical values for fiber parameters are used, i.e. $g_B=5\times10^{-11}$ m/W, $A_{eff}=50$ μm^2, and $\alpha=0.2$ dB/km. The input powers of the pump and Stokes waves are 1.5×10^{-3} W and 1×10^{-10} W, respectively. As can be seen from the figure, the power of the backscattered wave starts to grow exponentially when the fiber length is beyond 30 km, and the growth will stop when the attenuation in the fiber is higher than the amplification of the Stokes wave from SBS, that is when the fiber length is beyond 75 km. Since the obtaining of Fig. 2.2 is based on the assumption that the pump intensity is high, so that the pump depletion can be neglected. Therefore we can not see the saturation of the Stokes wave due to the pump depletion. The saturation effect will happen when the pump depletion is considered and hence Equations (2-6) and (2-7) should be used to calculate the Stokes wave power.

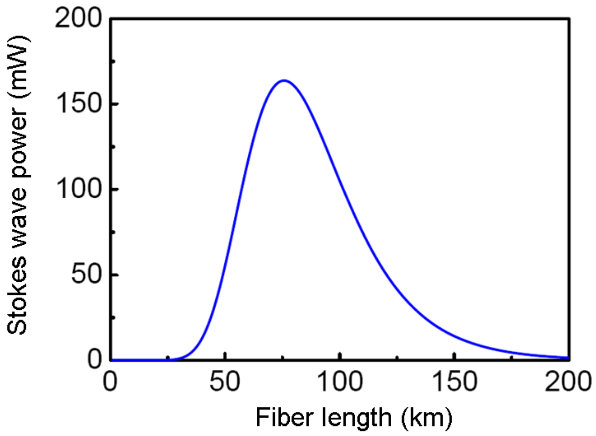

Fig. 2.2. Exponential power increase of the Stokes wave during stimulated Brillouin scattering process along the fiber length.

2.3 The Brillouin Gain

The SBS process provides a way of amplifying a weak signal whose frequency is within the Brillouin gain bandwidth. The gain value of the SBS depends on the Brillouin gain coefficient, the pump intensity and the effective fiber length. The intrinsic Brillouin gain bandwidth is within several tens of MHz, which is very small compared to that for Raman scattering. Therefore, SBS is usually used to achieve narrowband amplification.

2.3.1 Complex Brillouin Gain

In most of the literature, the Brillouin gain indicates the intensity amplification of the Stokes wave or a probe signal. However, during the scattering process, not only the intensity amplification happens, but also the refractive index change of the optical fiber takes place simultaneously. To represent the two phenomena, the complex Brillouin gain coefficient is defined as [4]:

$$g_B(\delta) = \frac{g_0}{1 - i\delta} = \frac{g_0}{1 - i\dfrac{(\omega_p - \omega_s - \Omega_B)}{\Gamma_B/2}} \tag{2-10}$$

in which g_0 is the peak value of the gain coefficient, ω_p and ω_s are the frequencies of the SBS pump and Stokes wave, $\Omega_B=2\pi\nu_B$ is the Brillouin frequency shift, Γ_B is the gain bandwidth and $\delta=(\omega_p-\omega_s-\Omega_B)/(\Gamma_B/2)$ is the normalized frequency detuning from the Brillouin resonance. The real part of $g_B(\delta)$ is

$$\mathrm{Re}[g_B(\delta)] = \frac{g_0}{1+\delta^2} = \frac{g_0(\Gamma_B/2)^2}{(\omega_p - \omega_s - \Omega_B)^2 + (\Gamma_B/2)^2} \tag{2-11}$$

which describes the narrowband amplification and thus the conventional Brillouin gain spectrum. The blue curve in Fig. 2.3 shows the normalized Brillouin gain versus the normalized frequency detuning. The gain spectrum has a Lorentzian shape with a peak value at δ=0, that is when the frequency of the Stokes wave has a downshift frequency equal to the Brillouin frequency shift from the pump wave. The Brillouin gain spectrum or the real part of the complex Brillouin gain will be discussed in detail in the next section. On the other hand, the imaginary part of $g_B(\delta)$ can be expressed as

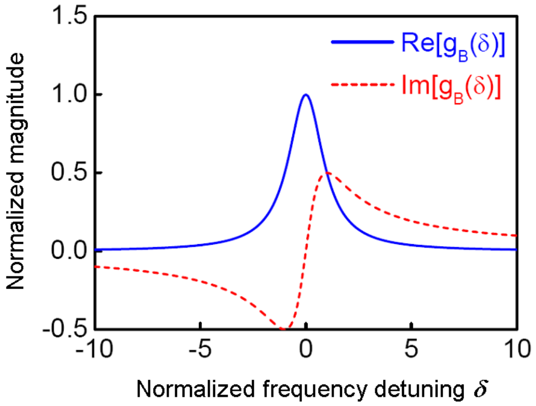

Fig. 2.3. Real and imaginary parts of the complex Brillouin gain coefficient.

$$\mathrm{Im}[g_B(\delta)] = \frac{g_0\delta}{1+\delta^2} = \frac{g_0(\omega_p-\omega_s-\Omega_B)(\Gamma_B/2)}{(\omega_p-\omega_s-\Omega_B)^2+(\Gamma_B/2)^2} \tag{2-12}$$

It accounts for the refractive index change accompanied by the amplification of the Stokes wave during SBS. The red dashed curve in Fig. 2.3 plots the relationship between the frequency detuning and the imaginary part of the complex Brillouin gain. Im[$g_B(\delta)$] is the origin of slow and fast light based on SBS [4, 5] and it will be discussed in Chapter 3.

2.3.2 Brillouin Gain Spectrum

As described in Equation (2-11) and Fig. 2.3, the Brillouin gain has a Lorentzian spectrum with its peak centered at a frequency which is downshift for a Brillouin frequency shift from the frequency of the pump wave. Fig. 2.4 shows a measured Brillouin gain spectrum of a conventional single-mode fiber (SMF) using the heterodyne method at room temperature [6]. Three parameters are usually used to characterize the Brillouin gain spectrum: the peak value of the gain coefficient g_0, the Brillouin frequency shift ν_B, and the gain bandwidth $\Delta\nu_B = \Gamma_B/2\pi$. As shown in Fig. 2.4 the measured Brillouin frequency shift is 10.575 GHz and the gain bandwidth is 40 MHz.

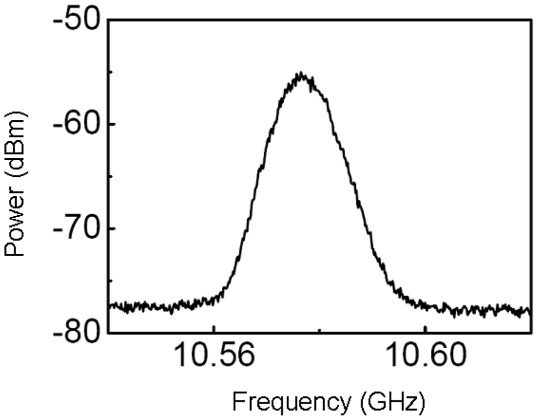

Fig. 2.4. Measured Brillouin gain spectrum of a conventional single-mode fiber at room temperature.

For continuous wave (CW) and quasi-CW pump, g_0 can be expressed as [3]

$$g_0 = \frac{8\pi^2\gamma_e^2}{n_p\lambda_p^2\rho_0 c v_A \Gamma_B} \qquad (2\text{-}13)$$

where v_A is the acoustic velocity, λ_p is the pump wavelength, n_p is the effective mode index at the pump wavelength, c is the speed of light in vacuum and Γ_B is the

Brillouin gain bandwidth; $\gamma_e \approx 0.902$ is the electrostrictive constant of silica and $\rho_0 \approx 2210$ kg/m^3 is its density [3]. Here, quasi-CW pump means a pulsed pump with temporal duration much longer than the phonon life time $T_B=1/\Gamma_B$, which is typically smaller than 10 ns. Typical parameter values of silica fibers can be used in Equation (2-13) to calculate g_0, and it is in the range 3×10^{-11}~5×10^{-11} m/W. If we compare this value with the gain coefficient for Raman scattering, we can find that it is larger by nearly three orders of magnitude than the Raman gain coefficient (3.1×10^{-14} m/W). That is why the SBS gain is usually higher than the Raman gain and thus its threshold is lower than that of Raman scattering. g_0 is related to both the waveguide characteristics and the material properties. In 1997, M. Nikles et al. measured g_0 for fibers with different doping levels of GeO_2 [7]. The values of g_0 under different doping levels are summarized in Table 2.1. As most of the parameters in Equation (2-13) depend on the material properties in the fiber, the dopant concentrations play an important role in the value of g_0, hence different doping levels will result in

Table 2.1 : Measured g_0, ν_B and $\Delta\nu_B$ for fibers with different doping levels of GeO_2 [7]

GeO_2-core content (wt. %)	Spot size (µm)	g_0 (m/W)	ν_B (GHz)	$\Delta\nu_B$ (MHz)
Bulk Silica		5.00E-11	13.1	23
0 (F-doped cladding)	4.4	1.73E-11	12.9896	50.74
2.65	5.04	2.62E-11	12.8527	35.5
2.94	4.64	2.27E-11	12.7974	37.5
2.94	4.82	2.60E-11	12.8082	35.5
4.71	4.16	2.62E-11	12.7191	34.5
6.18	3.44	2.24E-11	12.3882	40.4
6.50	3.2	2.15E-11	12.4178	45.94
8.24	2.96	1.63E-11	12.3343	42.1
9.41	3	3.05E-11	12.134	44.2
10.00	3.1	2.51E-11	12.054	45
17.65	1.84	1.93E-11	11.504	55

different values for g_0, as shown in Table 2.1. The spot size also affects the value of g_0.

Apart from the dependence of g_0 on the waveguide design and the material properties, the linewidth of the pump source is another factor that influences g_0. If the temporal duration of the pump pulses is much larger than the phonon life time or the linewidth of the pump source is much smaller than the intrinsic Brillouin gain bandwidth, then g_0 is mainly dependent on the material properties, rather than on the pump source. While if the duration of the pump pulses is smaller than the phonon life time or the linewidth of the pump source is broader than the intrinsic Brillouin gain bandwidth, the expression of g_0 should be changed to [1, 3]:

$$g_0 = \frac{8\pi^2\gamma_e^2}{n_p\lambda_p^2\rho_0 c v_A \Gamma_B}\left(\frac{\Delta\nu_B}{\Delta\nu_B \otimes \Delta\nu_p}\right) \tag{2-14}$$

where $\Delta\nu_p$ is the linewidth of the pump source, and $\otimes$ denotes the convolution operation between the pump linewidth and Brillouin gain bandwidth. For Gaussian distribution of the pump spectrum, we have

$$\Delta\nu_B \otimes \Delta\nu_p = \sqrt{\Delta\nu_B^2 + \Delta\nu_p^2} \tag{2-15}$$

while for a Lorentzian distribution, the corresponding equation is:

$$\Delta\nu_B \otimes \Delta\nu_p = \Delta\nu_B + \Delta\nu_p \tag{2-16}$$

No matter what the pump source is, i.e. CW or pulse, Gaussian or Lorentzian spectrum distribution, Equation (2-14) can be always simplified to Equation (2-13) as long as $\Delta\nu_B >> \Delta\nu_p$. It should be noted that Equation (2-14) shows that the peak value of the gain coefficient g_0 is reduced considerably if the pump source has a linewidth greater than the intrinsic Brillouin gain bandwidth. Therefore, the Brillouin gain is substantially reduced for the case where the pump linewidth exceeds $\Delta\nu_B$ or the pump pulse width is much smaller than the phonon life time. This phenomenon has been widely employed to suppress SBS in optical fibers [8, 9].

As shown in Equation (2-5), the Brillouin frequency shift ν_B is dependent on the pump wavelength, the acoustic velocity of the longitudinal mode and the refractive index of the fiber. Since both the acoustic velocity and the refractive index of the fiber are related to the fiber design (i.e. waveguide characteristics and dopant concentration), and external environment (i.e. temperature and strain on the fiber), the Brillouin frequency shift differs a lot depending on the particular conditions of the fiber. A larger dopant concentration reduces the acoustic velocity in the material, whereas it increases the refractive index [1]. The rate of decrease in acoustic velocity at increasing dopant concentration is higher than that of increase in refractive index. Hence, the Brillouin frequency shift becomes smaller at higher dopant concentration. This is verified in Table 2.1 where the fibers with the highest GeO_2 concentration have the smallest Brillouin frequency shift. Furthermore, the waveguide characteristics of the fiber (i.e. different spot size) also take an effect on the frequency shift of the Brillouin scattering, as shown in Table 2.1. Beside the fiber design, the temperature and strain also have influences on the Brillouin frequency shift, which have been widely used to construct Brillouin fiber sensors [10, 11]. The Brillouin fiber sensors will be discussed in Chapter 4.

The intrinsic gain bandwidth $\Delta\nu_B$ is related to the phonon life time. At a pump wavelength of 1550 nm, this natural Lorentzian shaped spectrum shows a width in the range of 30~40 MHz [1] in pure silica glass. A larger bandwidth for silica-based fibers has been observed [3]. The guided nature of acoustic modes in optical fibers partially contributes to the broadening of the bandwidth. The bandwidth increase is mainly attributed to inhomogeneities in the fiber-core cross section along the fiber length [3]. Furthermore, the numerical aperture of the fiber also has an effect on expanding the SBS gain spectrum [3]. The dopant concentration changes the properties of the fibers and thus affects the bandwidth as well, as shown in Table 2.1. Hence $\Delta\nu_B$ is determined by specific parameters of the fibers and is generally different for different fibers. Beside the fiber characteristics, another factor that affects the gain bandwidth is the linewidth of the pump source $\Delta\nu_p$. For the case where $\Delta\nu_B >> \Delta\nu_p$, the gain bandwidth is the intrinsic gain bandwidth; while for the case where $\Delta\nu_B < \Delta\nu_p$, the gain bandwidth is determined by the convolution of the pump linewidth and the intrinsic Brillouin gain bandwidth, as shown in Equation (2-15) and (2-16) [12].

The above discussion refers to the dominant peak of the Brillouin gain spectrum. The peak is located at a frequency determined by the Brillouin frequency shift and originates from the longitudinal acoustic mode propagating along the axes of an optical fiber. In general, Brillouin gain spectrum may contain multiple peaks that result from the additional transversal vibrational modes supported by the optical fibers [1, 3]. These modes can also scatter the pump light to generate the Stokes wave. As each transversal acoustic mode has a different propagation speed, it also leads to a different Brillouin frequency shift. Therefore, the Brillouin gain spectrum has several peaks. The number of peaks and the corresponding frequency shifts are determined by the details of the fiber design. Table 2.2 gives the Brillouin gain resonance frequencies for different fiber types [1]. The core diameters of the four fibers are 7.2 μm for TrueWave fiber (TW), 8.1 μm for AllWave fiber (AW), 1.7 μm for dispersion-compensating fiber (DCF) and 2.5 μm for highly germanium doped fiber (HG). Furthermore, the refractive index distribution of the four fibers are different with DCF, HG and AW showing uniform refractive index distribution in the core, and the TW fiber having a parabolic distribution. On the other hand, the peaks of the additional resonances of the core and cladding modes decrease as the input pump power increases. If the input pump power is higher than the threshold of SBS, the main resonance peak is enhanced continuously with increase in input power, while the other resonance peaks will decrease and eventually vanish [1].

Table 2.2 : Brillouin gain resonance frequencies in GHz for different fiber types measured at a pump wavelength of 1552 nm (AW=AllWave, TW=TrueWave, DCF=dispersion-compensating fiber, HG=highly Ge-doped) [1]

Fiber type	Main res.	2nd res.	3rd res.	4th res.	5th res.
AW	10.83	10.95	11.05	11.2	-
TW	10.7	10.82	10.9	-	-
DCF	9.77	10.28	10.68	10.78	10.89
HG	8.9	9.65	10.6	11.21	11.25

2.4 Threshold of Brillouin Scattering

The Brillouin threshold is defined as the input pump power at which the backscattered Stokes power is equal to the pump power at the fiber output [1, 3, 13]. According to Ref. [13], the Brillouin threshold is found to occur at a critical pump power P_{cr} expressed as

$$P_{cr} \approx 21 \frac{K_B \times A_{egff}}{g_0 L_{eff}} \tag{2-17}$$

Here, g_0 the peak value of the gain coefficient, A_{eff} and L_{eff} are the effective mode area of the fiber core and effective fiber length, respectively. K_B is a factor determined by the polarization relationship between the pump and Stokes waves and has a value between 1 and 2. If the pump and Stokes waves propagate along the fiber always with the same polarization, for example in polarization-maintaining fibers, then K_B =1. And if both waves propagate with completely random polarization then K_B =1.5. In conventional single mode fibers K_B shows a value of 2 [1].

To estimate the SBS threshold power, we first assume the pump and Stokes waves always keep the same polarization during their propagation along the fiber, and consider a long fiber section with a length L>50 km (e.g. long-haul transmission). This is always the case in a typical optical fiber link operating around 1.55 μm. Becasue $\alpha L>>1$ under such conditions, we can employ $L_{eff}=1/\alpha$, hence $P_{cr}=21\alpha A_{eff}/g_0$. If we adopt typical values for fiber parameters, i.e. $A_{eff}=50\ \mu m^2$, $\alpha=0.2$ dB/km, and $g_0=5\times10^{-11}$ m/W, the calculated critical pump power is $P_{cr}\approx1$ mW. The Brillouin threshold maintains such a low level due to the long fiber length. If the fiber length is largely shortened, for example L=1 m, the critical power is increased to 20 W. To further increase the threshold one may consider to use fibers with larger effective mode area.

References

[1] T. Schneider, *Nonlinear Optics in Telecommunications*, Springer, 2004.

[2] No. Shibata, A. Nakazono, N. Taguchi, and S. Tanaka, " Forward Brillouin Scattering in Holey Fibers," IEEE Photon. Technol. Lett., vol. 18, no. 2, pp. 412–414, January 2006.

[3] G. P. Agrawal, *Nonlinear Fiber Optics*, The Netherlands: Elsevier, Amsterdam, 2009.

[4] Y. Okawachi, M. S. Bigelow, J. E. Sharping, Z. Zhu, A. Schweinsberg, D. J. Gauthier, R. W. Boyd, and A. L. Gaeta, “Tunable All-Optical Delays via Brillouin Slow Light in an Optical Fiber,” Phys. Rev. Lett., vol. 94, 153902, April 2005.

[5] K. Y. Song, M. G. Herráez, and L. Thévenaz, “Observation of pulse delaying and advancement in optical fibers using stimulated Brillouin scattering,” Opt. Express., vol. 13, no. 1, pp. 82 – 88, January 2005.

[6] A. Yeniay, M.-M. Delavaux, and J. Toulouse, “Spontaneous and stimulated Brillouin scattering gain spectra in optical fibers,” IEEE J. Lightwave Tech., vol. 20, no. 8, 1425–1432, August 2002.

[7] M. Nikles, L. Thevenaz, and P. A. Robert, “Brillouin Gain Spectrum Characterization in Single-Mode Optical Fibers,” IEEE J. Lightw. Technol., vol. 15, no. 10, pp. 1842 – 1851, October 1997.

[8] A. Mussot, A. Durécu-Legrand, E. Lantz, C. Simonneau, D. Bayart, H. Maillotte, and T. Sylvestre, “Impact of Pump Phase Modulation on the Gain of Fiber Optical Parametric Amplifier,” IEEE Photon. Technol. Lett., vol. 16, no. 5, pp. 1289–1291, May 2004.

[9] S. Takasaka, Y. Mimura, M. Takahashi, R. Sugizaki, and H. Ogoshi, “Flat and Broad Amplification by Quasi-Phase-Matched Fiber Optical Parametric Amplifier,” in Proc. OFC/NFOEC 2012, Los Angeles, March 2012, paper OTh1C.4.

[10] S. M. Maughan, H. H. Kee, and T. P. Newson, “57-km single-ended spontaneous Brillouin-based distributed fiber temperature sensor using microwave coherent detection,” Opt. Lett., vol. 26, no. 6, 331–333 (2001)

[11] S. M. Lopez, M. A. Camas, F. Rodriguez, P. Cooredera, J. D. A. Castañon, L. Thévenaz, and M. G. Herraez, “Brillouin optical time-domain analysis assisted by second-order Raman amplification,” Opt. Express., vol. 18, no. 18, 18769–18778, August 2010.

[12] M. G. Herráez, K. Y. Song, and L. Thévenaz, “Aibitrary-bandwidth Brillouin slow light in optical fibers,” Opt. Express., vol. 14, no. 4, 1395–1400 (2006)

[13] R. G. Smith, “Optical Power Handling Capacity of Low Loss Optical Fibers as Determined by Stimulated Raman and Brillouin Scattering,” Appl. Opt., vol. 11, no. 11, 2489–2494, November 1972.

3 SLOW LIGHT BASED ON SBS IN OPTICAL FIBERS

Slow light in nonlinear media has attracted considerable interest because of its numerous applications, such as variable true time delay, optical synchronization, optical multiplexing/demultiplexing, and optical equalization [1]. In early slow light research, several commonly used techniques are electromagnetically induced transparency (EIT) [2], coherent population oscillations (CPO) [3], and waveguiding in photonic crystals [4]. In 2005, Okawachi et al. [5] and Song et al. [6] achieved slow light in optical fibers via stimulated Brillouin scattering (SBS). Using fibers to achieve slow light offers the advantages of room-temperature operation and device compatibility with existing fiber systems. Later, by exploiting pump spectral broadening techniques [7-9], SBS slow light has been used to support ~GHz signal bandwidth. The technique resulted in many demonstrations on the delay of ~Gbit/s communication data [10-15]. At the same time, slow light induced signal distortion has also been intensively studied and plenty of methods have been applied to minimize the distortion [16-21]. Apart from communications, SBS slow light has also been applied to other areas such as fiber sensing [22, 23].

This chapter is structured as follows. A brief introduction to slow light is given first in section 3.1, including the fundamentals of slow light, techniques to achieve slow light, and applications of slow light. Then the slow light technique based on SBS is discussed in detail in section 3.2. Last, generation of multichannel delayed pulses by FWM multicast in an SBS based slow light system is demonstrated in section 3.3.

3.1 Introduction to Slow Light

Slow light is a technique to reduce the group velocity of an optical pulse or information in propagation. In principle, slow light is generally realized by tailoring the dispersion of a nonlinear medium within a narrow spectral resonance. The key feature of the slow light effect is that a relatively large refractive index change is introduced to the nonlinear medium where the optical signal experiences the change when passing through it. Different frequency components of the optical signal travel with different velocities, resulting in a significant increase or decrease of group velocity. For group velocity decrease, it refers to slow light effect; while for the increase of group velocity, it is fast light effect. Both fast and slow light effects open up great opportunities to manipulate the transmitting speed of the optical information, and hence provide various potential applications in optical signal processing. Here, we focus mainly on slow light since it is more commonly used compared to fast light in the processing of optical signals in fiber communications and sensing [1, 7-15].

To have a clear understanding of slow light, it is important to first distinguish phase velocity and group velocity. For a monochromatic continuous-wave optical light with a frequency of ω_c, the phase velocity can be written as,

$$v_p = \frac{c}{n(\omega)}\Big|_{\omega=\omega_c} \tag{3-1}$$

where $n(\omega)$ is the frequency dependent refractive index, c is speed of light in vacuum. The phase velocity indicates the velocity at which the wavefront (surface formed by points of constant phase) travels. In general, the optical signal which carries optical information consists of a group of frequencies. In a dispersive medium, different frequency components have their own phase velocities and propagate at different speed. The phase velocity no longer stands for the propagation speed of the optical information. Accordingly, the group velocity is defined to represent the propagation speed of the optical information in a dispersive medium, which is the speed of the envelope of the optical signal. The expression of the group velocity is

$$v_g = \frac{c}{n_g} = \frac{c}{n(\omega) + \omega \frac{dn(\omega)}{d\omega}} \Big|_{\omega=\omega_c} \tag{3-2}$$

where ω_c is the central frequency and n_g is the group index of the material, expressed as

$$n_g = n(\omega) + \omega \frac{dn(\omega)}{d\omega} \tag{3-3}$$

From Equation (3-2) and (3-3) we can see the group velocity is strongly dependent on the change of refractive index with respect to the frequency. Therefore, if there is a rapid variation of refractive index (increase or decrease) within a narrow spectral range, the group velocity is increased or decreased significantly, corresponding to fast light or slow light effect.

Consider an optical signal passing through an optical medium with a length of L, as shown in Fig. 3.1. The time it takes for the signal to pass through the optical medium is known as the group delay T_g

$$T_g = \frac{L}{v_g} = \frac{Ln_g}{c} \tag{3-4}$$

This situation is given in the upper figure of Fig. 3.1. Then, if the slow light effect is introduced on the optical signal such that the group index increases to n_g' , as shown in the bottom half of Fig. 3.1, the group delay is increased to $T_g'=Ln_g'/c$. Consequently, a relative group delay T_{del} is found to be

$$T_{del} = T_g' - T_g = \frac{L}{c}(n_g' - n_g) = \frac{L}{c}\Delta n_g \tag{3-5}$$

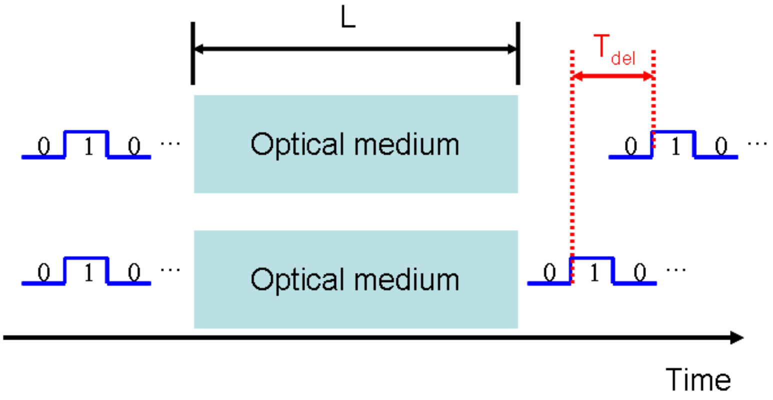

Fig. 3.1. The concept of tunable delay introduced by slow light.

where Δn_g is the increase of the group index. T_{del} shows the tunable delay from slow light effect and can be controlled by the group index change. In order to maximize the tunable delay, one may consider to have the optical medium as long as possible. But in practical situation, the length cannot be enlarged infinitely since the absorption losses and the dispersion-induced distortion limit the effective length of the optical medium. Thus the enhancement of tunable delay relies mainly on the increase of the group index, which requires a sharp variation of the refractive index that occurs within a narrow spectral resonance.

The key feature of the slow light technique is to introduce a sharp change of refractive index within a narrowband spectral resonance. By making the dispersion of the optical medium sufficiently strong in the vicinity of the resonance, the group velocity can be significantly reduced, leading to a large controllable delay. To date, various techniques have been proposed in achieving slow light, including electromagnetically induced transparency (EIT) [2], coherent population oscillations

(CPOs) [3], optical parametric amplification (OPA) [25], stimulated Brillouin [5, 6] and Raman scattering [26, 27], waveguiding in photonic crystals [4], coupled resonator optical waveguide [28, 29], and so on. Among those techniques, the slow light based on SBS has attracted much attention and has widely employed in optical signal processing. This is because the technique offer the advantages of room-temperature operation, the compatibility with existing fiber systems, simple configuration, arbitrary wavelength operation and easily tunable optical delay. In the following sections, we focus on the slow light effect based on SBS.

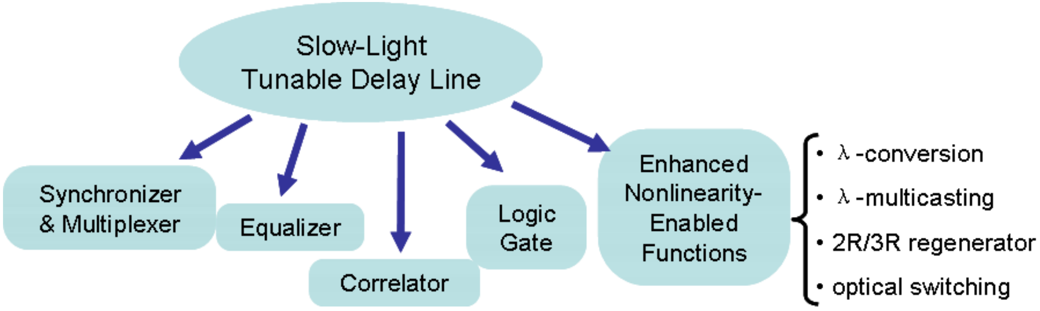

Fig. 3.2. Applications of slow-light based tunable delay line in optical signal processing [1].

It is worth mentioning that a number of all-optical signal processing techniques are based on slow light. Fig. 3.2 summarizes some of the applications of a tunable delay line based on slow light. They include optical synchronization and multiplexing [14, 30], optical equalization [31], optical correlation [32, 33], optical logic gates [34] and enhanced nonlinear interaction [35, 36].

3.2 Slow Light based on SBS in Optical Fibers

Since the SBS based slow light has the advantages of wavelength independent operation, low power consumption, room-temperature operation and compatibility with existing fiber-optic system, it is widely employed in all-optical signal processing [7-23]. Significant refractive index change takes place within a narrow spectral range during the amplification of the optical signal, leading to a controllable delay experiencing by the signal.

3.2.1 Mathematical Description

In absorbing systems, the nonlinear refractive index and absorption coefficient are related by the real and imaginary parts of the third-order susceptibility [37], e.g. the real part of the third-order susceptibility determines the refractive index while the imaginary part determines the absorption coefficient. The origin for this can be understood in a microscopic view as depicted in the following (quoted from Wikipedia):

“At the microscale, an electromagnetic wave's phase speed is slowed in a material because the electric field creates a disturbance in the charges of each atom (primarily the electrons) proportional to the electric susceptibility of the medium. (Similarly, the magnetic field creates a disturbance proportional to the magnetic susceptibility.) As the electromagnetic fields oscillate in the wave, the charges in the material will be "shaken" back and forth at the same frequency. The charges thus radiate their own electromagnetic wave that is at the same frequency, but usually

with a phase delay, as the charges may move out of phase with the force driving them (see sinusoidally driven harmonic oscillator). The light wave traveling in the medium is the macroscopic superposition (sum) of all such contributions in the material: The original wave plus the waves radiated by all the moving charges. This wave is typically a wave with the same frequency but shorter wavelength than the original, leading to a slowing of the wave's phase speed. Most of the radiation from oscillating material charges will modify the incoming wave, changing its velocity. However, some net energy will be radiated in other directions or even at other frequencies (see scattering).”

As discussed in Chapter 2, if the frequency of the Stokes wave is within the Brillouin gain bandwidth, it will experience a complex gain given by Equation (2-10). The real part of $g_b(\delta)$, $\mathrm{Re}[g_b(\delta)]$, represents the narrowband amplification while the imaginary part $\mathrm{Im}[g_b(\delta)]$ accounts for a sharp change of refractive index and is the origin of slow and fast light in fibers. The refractive index change is [38]

$$\Delta n_{SBS} = \frac{P_p \cdot c}{2A_{eff}\omega_s} \cdot \mathrm{Im}[g_b(\delta)] = \frac{P_p \cdot c}{2A_{eff}\omega_s} \cdot \frac{g_0 \delta}{1+\delta^2} \tag{3-6}$$

where c is the speed of light in vacuum, P_p is the power of the SBS pump, A_{eff} is the effective area of the fiber, g_0 is the peak value of the gain coefficient, and $\delta=(\omega_p-\omega_s-\Omega_B)/(\Gamma_B/2)$ is the normalized frequency detuning from the Brillouin resonance with ω_p and ω_s as the frequencies of the SBS pump and Stokes wave, $\Omega_B=2\pi\nu_B$ as the Brillouin frequency shift and Γ_B as the gain bandwidth. Equation (3-6) shows the refractive index variation during the SBS process and it happens within the Brillouin gain banwidth which is narrowband. Thus it will induce a large group index change experienced by the Stokes wave. The total refractive index under SBS is $n'=n+\Delta n_{SBS}$ with n as the original refractive index of the optical fiber in the absence of SBS. According to Equation (3-3) the group index under SBS becomes

$$\begin{aligned} n_g' &= n' + \omega_s \frac{dn'}{d\omega_s} = n_g + (\Delta n_{SBS} + \omega_s \frac{d\Delta n_{SBS}}{d\omega_s}) \\ &= n_g + (\frac{g_0 c P_p}{\Gamma_B A_{eff}}) \cdot \frac{1-\delta^2}{(1+\delta^2)^2} \end{aligned} \tag{3-7}$$

where $n_g=n+\omega_s dn/d\omega_s$ is the group index without SBS. Obviously if δ is in the range of -1 ~ 1, the group index is increased, meaning the propagation speed of the Stokes wave is slowed down. Fig. 3.3 shows the SBS induced refractive index change (Δn_{SBS}) and the resulting group index change ($\Delta n_g = n_g' - n_g$) versus the normalized frequency detuning δ. The parameters used to obtain Fig. 3.6 are $g_0=5\times10^{-11}$ m/W, $A_{eff}=50\ \mu m^2$,

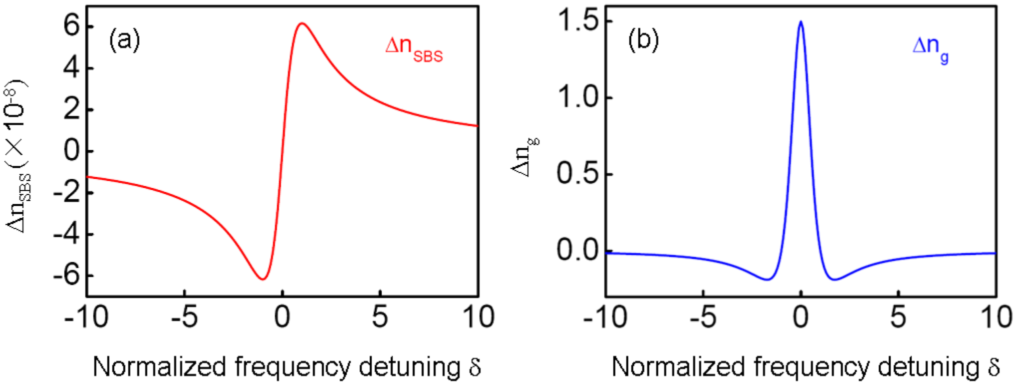

Fig. 3.3. (a) SBS induced refractive index change; (b)corresponding group index change.

P_p=1 W, λ=1.55 μm, c=3×10^8 m/s and $\Gamma_B=2\times10^8$ (the phonon life time $T_B=1/\Gamma_B$=5 ns). At this pump power level, the refractive index change is ~10^{-8}, but the group index change is as large as 1.5, almost two times of its original value. And the group index change can be further enhanced by improving the power of the pump light. Since the propagation speed of the Stokes wave is reduced, according to Equation (3-

5) and (3-7) the group delay or tunable delay introduced by the SBS based slow light can be found to be

$$T_{del} = (\frac{g_0 P_p L}{\Gamma_B A_{eff}}) \cdot \frac{1-\delta^2}{(1+\delta^2)^2} \tag{3-8}$$

The maximum delay is

$$\Delta T_{\max} = \frac{g_0 P_p L}{\Gamma_B A_{eff}} \tag{3-9}$$

achieved at δ=0 where the frequency of the Stokes wave is downshifted by a Brillouin frequency shift from the pump wave. From Equation (3-9) we can see ΔT_{max} is only determined by the power of the pump wave once the optical fiber is chosen. Therefore, the tunability of the delay is usually realized by controlling the pump power. However, the achievable maximum delay is limited by the distortion of the optical signal when the pump power is too large. The origin of the distortion comes from the SBS induced dispersion within the narrowband resonance, and it will be discussed in Section 3.2.3.

3.2.2 Delay of Optical Signals by SBS based Slow Light

The first demonstration of delaying optical pulses through SBS based slow light is achieved by K. Y. Song et al. [5] and Y. Okawachi et al. [6] in 2005. In Ref. [5], the optical pulse with a width of 100 ns is delayed by 30 ns at a gain of 30 dB in a standard single-mode fiber (SMF) while in a dispersion shifted fiber (DSF) it has a maximum delay of 18 ns obtained under a gain of 25 dB. Fig. 3.4 shows the main results in Ref. [5]. As is expected from Equation (3-9), the delay time is linearly

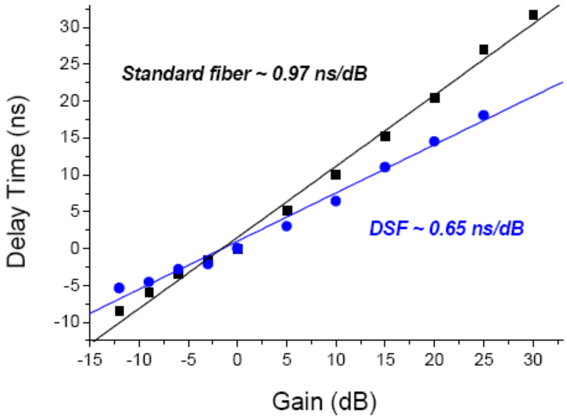

Fig. 3.4. Delay time versus the gain for standard fiber and dispersion shifted fiber (DSF) [5].

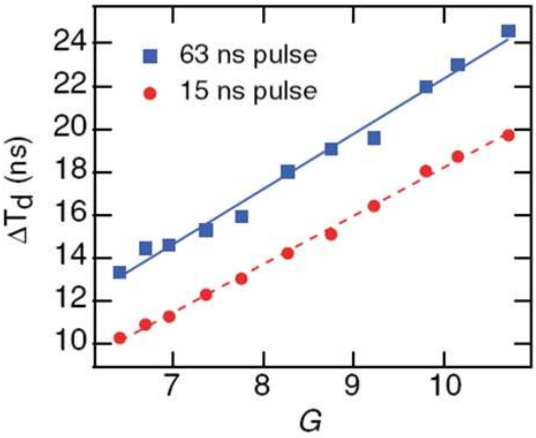

Fig. 3.5. Delay time versus the gain parameter in a single-mode fiber for optical pulses with two different input width [6].

proportional to the pump power or the Brillouin gain in logarithmic scale (Brillouin gain in dB: 10log[exp(g_0P_pL/A_{eff})]=4.34 g_0P_pL/A_{eff}). The only difference between the delay in SMF and DSF lies in the different Brillouin gain bandwidth. On the other hand, a maximum delay of 25 ns for a 63 ns optical pulse and 20 ns for a 15 ns pulse were obtained in Ref. [6], as shown in Fig. 3.5. The authors also observed pulse broadening of the delayed pulses and found that the distortion becomes significant as the pulse width is reduced to below 10 ns.

However, the intrinsic SBS gain bandwidth is several tens of MHz, such that the early demonstrations of SBS based slow light can only be used to delay optical pulses with width much longer than the phonon life time (typical value <10 ns). For communication signals, the bandwidth is usually in the range of ~GHz, thus the intrinsic SBS gain bandwidth can not support the delay of signals with ~GHz bandwidth. In order to make the SBS based slow light practical in delaying communication data, the broadening of the SBS gain bandwidth becomes indispensable. Recent breakthroughs by exploiting pump spectral broadening techniques [7-9] enable the SBS slow light to support the delay of ~Gbit/s communication data [10-15]. When the pump is broadened, the Brillouin gain spectrum is given by the convolution of the pump spectrum and the intrinsic Brillouin gain spectrum [7]. Assume the pump spectrum has a Lorentzian distribution with a linewidth of $\Delta\nu_p$ after broadening, then the effective Brillouin gain bandwidth becomes the sum of the pump linewidth and the intrinsic Brillouin gain bandwidth. The effective Brillouin gain parameter is given by [7]

$$\mathrm{G}=\frac{g_0 P_p L}{A_{eff}}\cdot\frac{\Delta\nu_B}{\Delta\nu_B+\Delta\nu_p} \tag{3-10}$$

in which $\Delta\nu_B=\Gamma_B/2\pi$ is the intrinsic Brillouin gain bandwidth. The maximum delay in Equation (3-9) is now modified to be

$$\Delta T_{\max}=\frac{G}{2\pi(\Delta\nu_B+\Delta\nu_p)}=\frac{g_0 P_p L\Delta\nu_B}{2\pi A_{eff}(\Delta\nu_B+\Delta\nu_p)^2} \tag{3-11}$$

From Equation (3-11) we can see if the bandwidth is a tenfold increase, the delay has hundredfold reduction at the same pump power level. There are several methods to broaden the pump spectrum, including (1) direct modulation of the pump laser using pseudo-random bit sequence (PRBS) data [7] or Gaussian noise [8]; (2) external phase modulation of the pump [9]; (3) using incoherent filtered ASE source as the pump [15]. All of these techniques make the delay of multi-Gbit/s data signals possible through the SBS slow light medium, which enables the SBS mechanism practical in a real optical communication systems.

It is worth mentioning that due to the dispersion happening within the narrow spectral resonance, the delayed signals will be distorted, which will affect the performance of the tunable delay. This slow light induced signal distortion has also been intensively studied and plenty of methods have been applied to minimize the distortion [16-21]. Furthermore, there is a trade-off between the signal delay and signal quality which originates from the delay–bandwidth product. This has set a fundamental limitation in slow light systems [1]. For example, although delay values of several pulse periods have been demonstrated based on SBS slow light, the maximum achievable delay suffers from a fundamental delay-bandwidth product for a given signal bandwidth [1]. This tradeoff has also been extensively studied and reported in many literatures [1].

3.3 Generation of Multichannel Delayed Pulses by FWM Assisted SBS Slow Light System

Owing to the tight requirement of spectral alignment between the SBS pump and the signal, most of the published works are for the case where one SBS pump is used to delay a single channel. Hence, only one delayed channel is obtained. If multiple delayed signals can be simultaneously generated with a single SBS pump, the potential for multichannel signal processing can be unveiled. Examples of parallel processing with multiple pulsed or data outputs are multichannel synchronization, multichannel time division multiplexing and multichannel regeneration. A common approach of generating multichannel signals is by four wave mixing (FWM) wavelength multicast through which the information carried by a single signal is copied to different wavelengths [39-41]. In this section, we demonstrate simultaneous generation of multichannel delayed pulses by using FWM in a single-pump SBS slow light system. The SBS delay of the signal is successfully transferred to six channels through FWM wavelength multicast. It is worth mentioning that FWM has previously been used to perform single-channel slow light conversion [42]. However, there was no report on analyzing the relationship between the delay of the idler and that of the original signal. Here, we demonstrate simultaneous multichannel slow light conversion using a single SBS pump. Both theoretical and experimental investigations of the delay performance of the six output channels have been carried out. The relationship of the time delay between the original signal and that of the multicast outputs is analyzed.

3.3.1 Principle and Experimental Setup

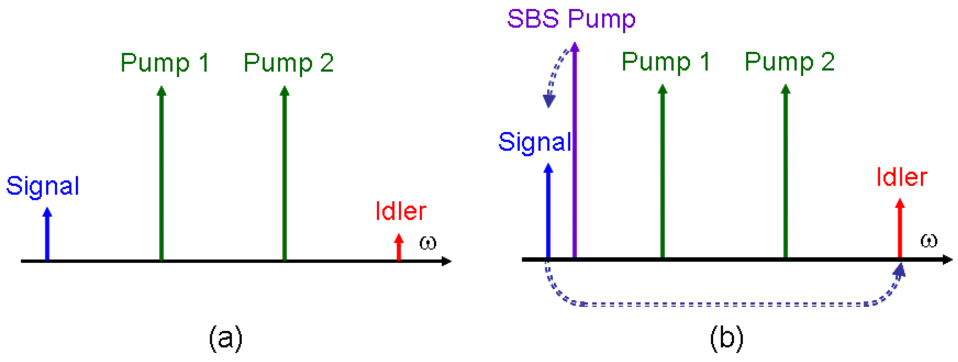

Fig. 3.6. Spectral assignment in (a) conventional nondegenerate FWM; (b) nondegenerate FWM with slow light transferred from signal to idler.

The spectral plot for a conventional nondegenerate FWM process is illustrated in Fig. 3.6. The index grating caused by the beating between the signal and pump 1 scatters pump 2 to generate an idler. If the pumps remain undepleted during the FWM process, the power of the converted idler can be expressed as [38, 43]

$$P_i(L) = \eta(\kappa)\gamma^2 L_{eff}^2 P_1 P_2 P_s e^{-\alpha L} \tag{3-12}$$

Here, γ is the nonlinear coefficient of the fiber, P_1, P_2 and P_s are the power of pump 1, pump 2, and signal, respectively, L is the fiber length, α is the attenuation coefficient, $L_{eff} = [1-\exp(-\alpha L)]/\alpha$ is the effective fiber length, $\eta(\kappa)$ is the FWM efficiency and $\kappa = \Delta k + \gamma(P_1 + P_2)$ is defined as the effective phase mismatch with Δk representing the linear phase mismatch. When the phase matching is perfect ($\kappa=0$), $\eta(\kappa)$ reaches its maximum value. For SBS to take place, the signal and the SBS pump should counter-propagate in the fiber where the signal is amplified and delayed by the slow light effect. The real part of the complex Brillouin gain coefficient Re[$g_B(\delta)$] is related to the gain of the signal, causing it to grow exponentially if pump depletion is neglected. Thus,

$$P_s(L) = P_s(0)\,\mathrm{e}^{\mathrm{Re}(g_B)P_p L_{eff}/A_{eff} - \alpha L} \tag{3-13}$$

where P_p is the SBS pump power and A_{eff} is the fiber effective mode area. The imaginary part $\mathrm{Im}[g_B(\delta)]$ accounts for the slow light effect and the time delay is given in Equation (3-8) and (3-9). ΔT_{max} is only dependent on the gain parameter $G= g_0LP_p/A_{eff}$ and the gain bandwidth Γ_B. We now consider the case where a counter-propagating SBS pump is introduced to delay the signal, as shown in Fig. 3.9 (b). Owing to SBS-FWM interaction, the phase mismatch will become [44]

$$\kappa = \Delta k + \gamma(P_1 + P_2) - \mathrm{Im}[g_B(\delta)]P_p \tag{3-14}$$

and the power of the idler will be

$$P_i(L) = \eta(\kappa)\gamma^2 L_{eff}^2 P_1 P_2 P_s\,\mathrm{e}^{\mathrm{Re}(g_B)P_p L_{eff}/A_{eff}}\, e^{-\alpha L} \tag{3-15}$$

Equation (3-14) implies that the phase mismatch can be controlled by adjusting the frequency detuning δ[44]. Compared to the case without SBS described by Equation (3-12), not only the signal power is increased but the FWM efficiency is also affected. As the idler power is proportional to the signal power, the SBS gain to the signal ($\mathrm{Re}(g_B)$) will be completely transferred to the idler. Hence, the idler should experience the same SBS gain as that of the signal, although its net gain may differ due to the change in FWM efficiency. Furthermore, the phase change of the signal ($\mathrm{Im}(g_B)$) caused by SBS should also be copied to the idler because FWM is a phase transparent process. Since both the real and imaginary parts of the complex Brillouin gain coefficient are transferred by the FWM process, the idler and the signal should have almost identical time delay. Therefore, when multiple pumps are introduced for FWM wavelength multicast in the presence of a single SBS pump for slow light, multiple copies of the delayed signal can be simultaneously produced. It is important to note that the SBS time delay transferred to the idlers depends only on the SBS gain parameter rather than on the net gain of the idlers, which is also determined by the FWM efficiency.

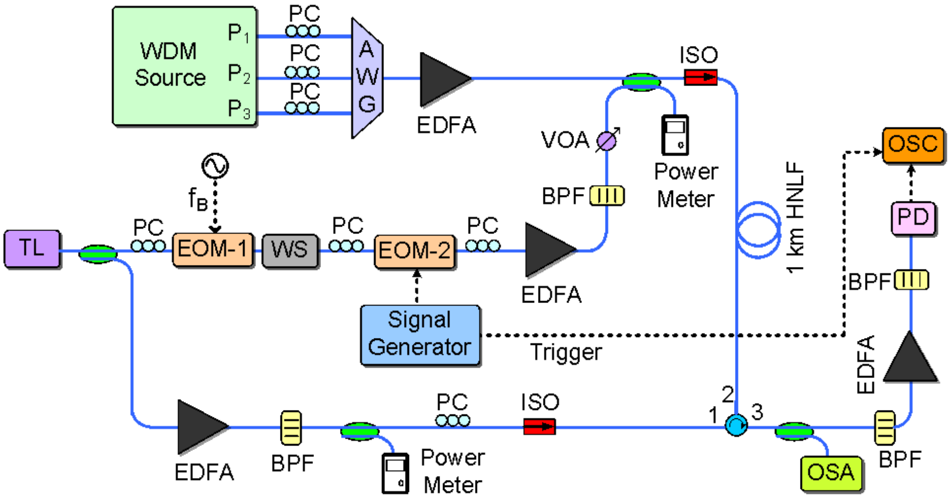

Fig. 3.7. Experimental setup for the generation of multichannel delayed signals. TL: tunable laser; AWG: arrayed waveguide grating; EOM: electro-optic intensity modulator; WS: wave shaper; EDFA: erbium-doped fiber amplifier; PC: polarization controller; VOA: variable optical attenuator; BPF: band pass filter; HNLF: highly nonlinear fiber; ISO: isolator; OSA: optical spectrum analyzer; PD: photo-detector; OSC: oscilloscope.

The experimental setup is shown in Fig. 3.7. The output of a tunable laser is split into two branches. The lower branch is amplified by an erbium-doped fiber amplifier (EDFA) and serves as the SBS pump. The amplified spontaneous emission (ASE) noise from the EDFA is filtered out by a bandpass filter (BPF). The upper branch is first modulated by an electro-optic intensity modulator (EOM-1) biased to suppress the optical carrier and driven at a frequency equal to the Brillouin frequency shift (ν_B

$=\Omega_B/2\pi$). The optical spectrum after the modulation is depicted in Fig. 3.8 (a). The carrier suppression ratio is over 23 dB. Next, a waveshaper is used as a narrowband filter to select the longer wavelength sideband (1547.66 nm) as shown in Fig. 3.8 (b). This sideband is then intensity modulated by EOM-2 to produce a 40 ns signal pulse. The signal passes through another EDFA and a variable optical attenuator (VOA) to facilitate control of its power. To introduce FWM, three optical pumps are provided from a wavelength division multiplexing (WDM) transmitter. They are amplified by an EDFA to a total power of 130 mW and are combined with the signal through a 3 dB coupler. The three FWM pumps are set at unequally spaced wavelength of 1548.58 nm, 1551.66 nm and 1557.58 nm to minimize crosstalk from pump beatings. The signal together with the three pumps are directed to a 1 km highly nonlinear fiber (HNLF) where FWM takes place in the presence of the counter-propagating SBS pump. The HNLF has a nonlinear coefficient of 11/(W•km), a dispersion coefficient of –0.4 ps/(nm•km) and a dispersion slope of 5.7×10^{-3} ps/(nm^2•km) at ~1550 nm. The Brillouin frequency shift and gain bandwidth of the HNLF are

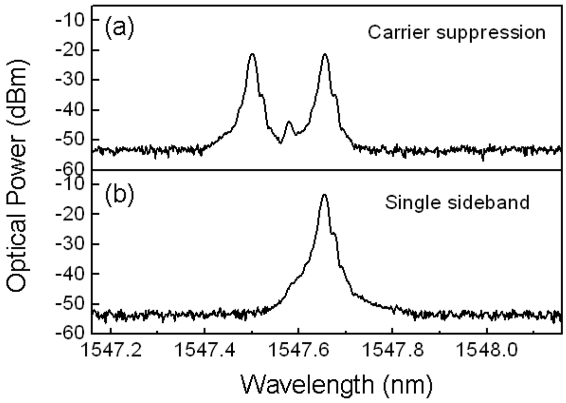

Fig. 3.8. Optical spectrum of (a) carrier suppressed modulated output; (b) filtered sideband at longer wavelength.

measured to be 9.71 GHz and 40 MHz, respectively. As the signal is slowed down by the SBS pump, its delay is transferred to all the multicasting channels (converted idlers) through FWM. A 0.3-nm BFP is used at port 3 of the optical circulator to extract individual channels, which are then amplified and analyzed.

3.3.2 Results and Discussion

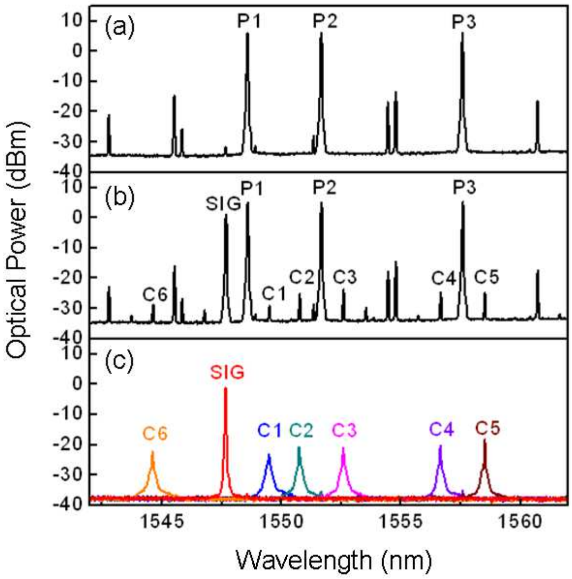

Fig. 3.9. Optical spectra showing (a) FWM without SBS pump; (b) FWM in the presence of a 26.5 mW SBS pump; (c) delayed signal and multicast outputs.

Fig. 3.9 (a) plots the FWM spectrum (measured at port 3 of the optical circulator) when the signal power is intentionally reduced and the SBS pump is turned off. The FWM components are mainly caused by beatings among the three FWM pumps. After the SBS pump is turned on, the resultant spectrum is shown in Fig. 3.9 (b). The signal is amplified and delayed by the SBS pump, while at the same time it is copied to six wavelengths from channel 1 to channel 6. The degenerate FWM between the signal and pump 1 generates channel 1. The index grating produced by the beating between the signal and pump 1 scatters pump 2 to generate channel 2 and channel 3, and scatters pump 3 to generate channel 4 and channel 5. Channel 6 is generated through scattering of the signal by the index grating originated from the beating of pump 1 and pump 2. The conversion efficiencies from channel 1 to channel 6 are -30 dB, -25.22 dB, -24.48 dB, -25.66 dB, -25.75 dB and -29.64 dB, respectively. The relatively low optical signal-to-noise ratio (OSNR) of the converted idlers observed in Fig. 3.9 (b) may be caused by non-optimized polarization states of the three FWM pumps and the finite spectral resolution (0.1 nm) of the optical spectrum analyzer. Another reason is that although the SBS gain of the signal should be transferred to the idlers, the power increase of the idlers are actually smaller because the SBS process also changes the FWM efficiency by increasing the phase mismatch. To enhance the output OSNR, one may consider to increase the input signal power. However, the achievable maximum delay will be reduced because the signal gain will be saturated at a lower level [5]. A trade-off should thus be adopted. Fig. 3.9 (c) shows the spectra (measured just before the photo-detector) of the individually extracted channels including the signal by tuning the center wavelength of the bandpass filter. Other higher order FWM components are not selected due to the low conversion efficiencies.

To investigate the performance of the time delay for each individual channel, we fix the center wavelength of the bandpass filter to select one channel at a time. The time delay is measured at different SBS pump power levels. The results are presented in Fig. 3.10 (a) and (b). For the signal itself, different time delays are obtained at

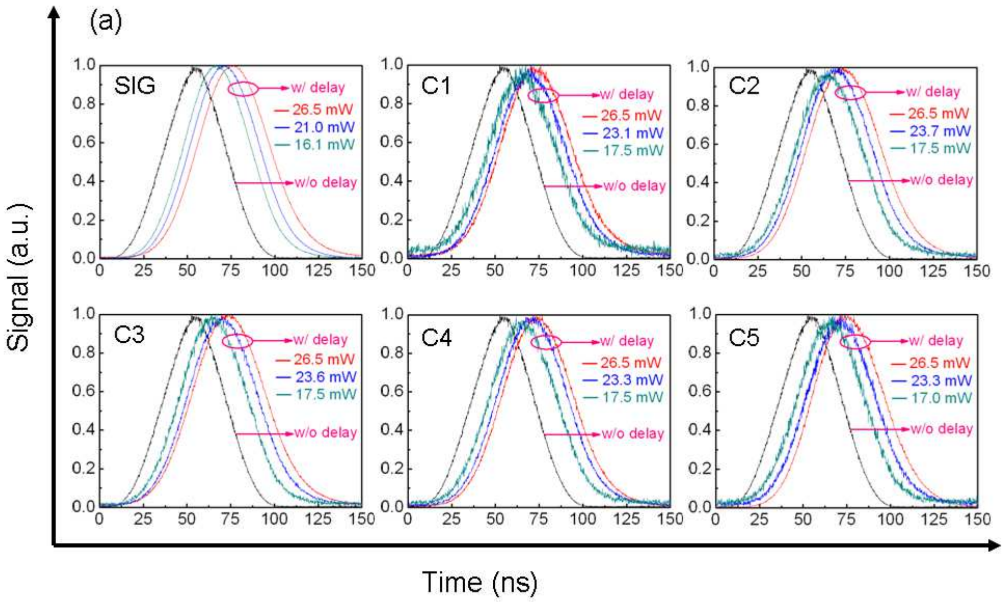

Fig. 3.10. (a) Measured delayed pulse waveforms for individual channels including the signal and channels 1 to 5 (SIG, C1 to C5) at different SBS pump power levels. Black curves (w/o delay) are for the cases without SBS pump; red, blue and green curves (w/ delay) are for the cases with SBS pump at different power levels.

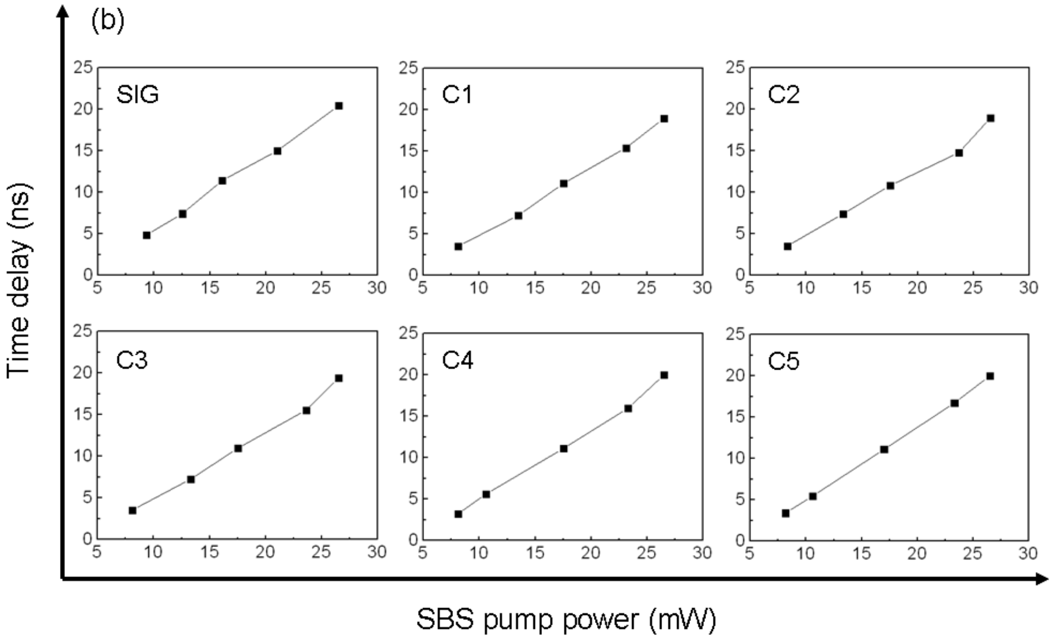

Fig. 3.10. (b) Time delay versus SBS pump power for individual channels including the signal and channels 1 to 5 (SIG, C1 to C5).

different SBS pump power levels (shown as the red, blue and green curves in Fig. 3.10 (a)-SIG). The time delay grows linearly with the increase of the SBS pump power as shown in Fig. 3.10 (b)-SIG. The maximum time delay is ~20 ns and is achieved at 26.5 mW SBS pump power. At higher input pump power, the delay will not change much owing to gain saturation of the signal as well as saturation of the pump field caused by SBS generation of a Stokes field at the output fiber end [5]. It is noticed that the time delay is accompanied by a slight pulse broadening. From Fig. 3.10 (a)-C1 to C5, we can see clearly that all the converted channels are delayed and the time delay is also related to the SBS pump power. This relationship between the delay and the SBS pump power is found to be linear as well, as shown in Fig. 3.10 (b)-C1 to C5. The result concludes that the slow light effect on the signal is transferred successfully to all converted channels through the FWM multicasting

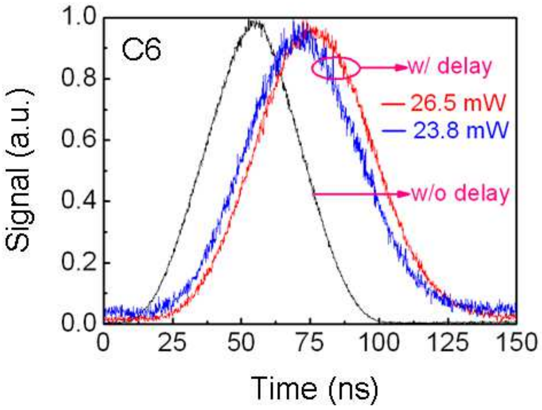

Fig. 3.11. Measured delayed pulse waveforms for channel 6 at two different SBS pump power levels. The black curve (w/o delay) is for the case without SBS pump; the red and blue curves (w/ delay) are for the cases with SBS pump at different power levels.

process. Here in Fig. 3.10 (a), we note that the delayed signal exhibits higher optical signal-to-noise ratio (OSNR) than those of the delayed channels 1 to 5. It is because the power of the SBS amplified signal is much higher than those of the multicast channels, of which the powers are limited by the FWM conversion efficiency. Accordingly, channel 1 is slightly noisier than other channels due to its low conversion efficiency. Furthermore, for each channel including the signal, the OSNR degrades as the SBS pump power is reduced to provide a smaller optical gain. Similar to channel 1, channel 6 exhibits a relatively low conversion efficiency. Hence, we only measure its pulse waveforms at two SBS pump power levels, as depicted in Fig. 3.11.

From our theoretical analysis, the time delay of the converted channels should be almost the same as that of the delayed signal. To clearly compare their time delays and waveforms, we fix the SBS pump power and tune the center wavelength of the bandpass filter to select each channel in turn for the measurement. The results are plotted in Fig. 3.12. Fig. 3.12 (a) to (c) show the delayed pulse waveforms of the signal and channels 1 to 5 at three fixed SBS pump power levels: 12.5 mW, 18.3 mW and 24.4 mW. As mentioned before, the OSNR is smaller at lower SBS pump power levels. Consequently, the delayed pulses in Fig. 3.12 (a) are noisier than those in (b) and (c). At each SBS pump power level, the delayed pulse waveforms of the converted channels almost overlap completely with that of the signal, implying that they all experience approximately the same time delay. In Fig. 3.12 (d), we show the delays of each channel at the three SBS pump power levels. The average delays at the pump levels are 6.39 ns, 12.47 ns, and 18.27 ns, respectively. The maximum time delay difference among all the channels is 0.89 ns and may be caused by measurement errors and SBS pump power fluctuations.

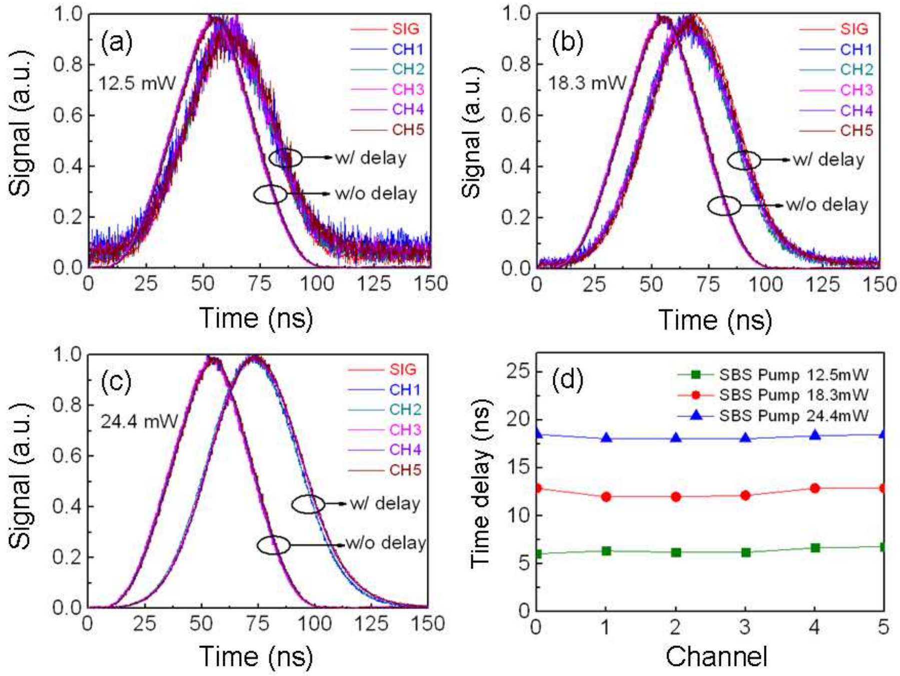

Fig. 3.12. Measured delayed pulse waveforms from the signal to channel 5 (SIG to CH5) at three fixed SBS pump power levels: (a) 12.5 mW; (b) 18.3 mW; (c) 24.4 mW. The curves labelled "w/o delay" are for the case without SBS pump; the curves labelled "w/ delay" are for the case with SBS pump. (d) time delay vs. channel at three fixed SBS pump power levels; channel 0 is the signal.

In conclusion, using FWM wavelength multicast in a single-pump SBS slow light system, we have demonstrated simultaneous generation of six delayed signals in a highly nonlinear fiber. The time delay performance of the multicasting channels is almost identical to that of the original signal. The maximum delay achieved is about 20 ns, and the maximum delay difference among the channels is 0.89 ns. To apply the technique for the delay of communication data, one simply needs to enlarge the SBS gain bandwidth by spectral broadening of the SBS pump. This slow light multicasting technique may find applications in parallel optical information processing such as simultaneous multichannel synchronization and time division multiplexing.

References

[1] A. E. Willner, B. Zhang, L. Zhang, L. Yan, and I. Fazal, “Optical signal processing using tunable delay elements based on slow light,” IEEE J. Sel. Topics Quantum Electron., vol. 14, no. 3, pp. 691-705, May 2008.

[2] L. V. Hau, S. E. Harris, Z. Dutton, and C. H. Behroozi, “Light speed reduction to 17 meters per second in an ultracold atomic gas,” Nature 397, pp. 594-598, February 1999.

[3] M. S. Bigelow, N. N. Lepeshkin, and R. W. Boyd, “Superluminal and slow light propagation in a roomtemperature solid,” Science 301, pp. 200-202, July 2003.

[4] M. Notomi, K. Yamada, A. Shinya, J. Takahashi, C. Takahashi, and I. Yokohama, “Extremely large group-velocity dispersion of line-defect waveguides in photonic crystal slabs,” Phys. Rev. Lett., vol. 87, 253902, December 2001.

[5] Y. Okawachi, M. S. Bigelow, J. E. Sharping, Z. Zhu, A. Schweinsberg, D. J. Gauthier, R. W. Boyd, and A. L. Gaeta, “Tunable all-optical delays via Brillouin slow light in an optical fiber,” Phys. Rev. Lett., vol. 94, 153902, April 2005.

[6] K. Y. Song, M. G. Herráez, and L. Thévenaz, “Observation of pulse delaying and advancement in optical fibers using stimulated Brillouin scattering,” Opt. Express., vol. 13, no. 1, pp. 82-88, January 2005.

[7] M. G. Herráez, K. Y. Song, and L. Thévenaz, “Aibitrary-bandwidth Brillouin slow light in optical fibers,” Opt. Express., vol. 14, no. 4, pp. 1395-1400, February 2006.

[8] Z. Zhu, A. M. C. Dawes, D. J. Gauthier, Lin Zhang, and A. E. Willner, “Broadband SBS slow light in an optical Fiber,“ IEEE J. Lightw. Technol., vol. 25, no. 1, pp. 201-206, January 2007.

[9] A. Cheng, M. P, Fok, and C. Shu, “Wideband SBS slow light in a single mode fiber using a phase-modulated pump,” in CLEO 2007, Baltimore, MA, May 2007, Paper JWA49.

[10] B. Zhang, L. Zhang, L. Yan, I. Fazal, J. Yang, and A. E. Willner, “Continuously-tunable, bit-rate variable OTDM using broadband SBS slow-light delay line,” Opt. Express., vol. 15, no. 13, pp. 8317-8322, June 2007.

[11] L. Yi, L. Zhan, W. Hu, and Y. Xia, “Delay of broadband signals using slow light in stimulated brillouin scattering with phase-modulated pump,” IEEE Photon. Technol. Lett., vol. 19, no. 8, pp. 619-621, April 2007.

[12] B. Zhang, L. Yan, I. Fazal, L. Zhang, A. E. Willner, Z. Zhu, and D. J. Gauthier, “Slow light on Gbit/s differential-phase-shift-keying signals,” Opt. Express., vol. 15, no. 4, pp. 1878-1883, February 2007.

[13] B. Zhang, L. Yan, L. Zhang, S. Nuccio, L. Christen, T. Wu, and A. E. Willner, “Spectrally efficient slow light using multilevel phase-modulated formats,” Opt. Lett., vol. 33, no. 1, pp. 55-57, Jan. 2008.

[14] B. Zhang, L Yan, J. Yang, I. Fazal, and A. E. Willner, “A single slow-light element for independent delay control and synchronization on multiple Gb/s data channels,” IEEE Photon. Technol. Lett., vol. 19, no. 14, pp. 1081-1083, July 2007.

[15] B. Zhang, L Yan, L. Zhang, and A. E. Willner, “Multichannel SBS slow light using spectrally sliced incoherent pumping,” IEEE J. Lightw. Technol., vol. 26, no. 23, pp. 3763 -3769, December 2008.

[16] E. Shumakher, N. Orbach, A. Nevet, D. Dahan, and G. Eisenstein, “On the balance between delay, bandwidth and signal distortion in slow light systems based on stimulated Brillouin scattering in optical fibers,“ Opt. Express., vol. 14, no. 13, pp. 5877-5884, June 2006.

[17] L. Zhang, T. Luo, C. Yu, W. Zhang, and A. E. Willner, “Pattern dependence of data distortion in slow-light elements,” IEEE J. Lightw. Technol., vol. 25, no. 7, pp. 1754 -1760, July 2007.

[18] T. Schneider, R. Henker, K. Lauterbach, and M. Junker, “Distortion reduction in slow light systems based on stimulated Brillouin scattering,“ Opt. Express., vol. 16, no. 11, pp. 8280-8285, May 2008.

[19] S. Wang, L. Ren, Yu Liu, and Y. Tomita, “Zero-broadening SBS slow light propagation in an optical fiber using two broadband pump beams,” Opt. Express., vol. 16, no. 11, pp. 8067-8076, May 2008.

[20] S. Chin, M. G. Herráez, and L. Thévenaz, “Complete compensation of pulse broadening in an amplifier-based slow light system using a nonlinear regeneration element,” Opt. Express., vol. 17, no. 24, pp. 21910-21917, November 2009.

[21] A. Wiatrek, K. Jamshidi, R. Henker, S. Preußler, and T. Schneider, ”Nonlinear Brillouin based slow-light system for almost distortion-free pulse delay,” J. Opt. Soc. Am. B, vol. 27, no. 3, pp. 544-549, March 2010.

[22] L. Wang, B. Zhou, C. Shu, and S. He, “Stimulated Brillouin scattering slow-light-based fiber-optic temperature sensor, ” Opt. Lett., vol. 36, no. 3, pp. 427-429, February 2011.

[23] L. Wang, and C. Shu, “Demonstration of distributed strain sensing with the use of stimulated Brillouin scattering-based slow light,” IEEE Photon. J., vol. 3, no. 6, pp. 1164-1170, December 2011.

[24] R. W. Boyd and D. J. Gauthier, “Slow and fast light,” in Progress in Optics, E.Wolf, ed. (Elsevier, Amsterdam), vol. 43, chap. 6, pp. 497, 2002.

[25] D. Dahan and G. Eisenstein, “Tunable all optical delay via slow and fast light propagation in a Raman assisted fiber optical parametric amplifier: a route to all optical buffering,” Opt. Express, vol. 13, pp. 6234, August 2005.

[26] Y. Okawachi, M. Foster, J. Sharping, A. Gaeta, Q. Xu, M. Lipson, “All-optical slow-light on a photonic chip,” Opt. Express, vol. 14, pp. 2317, March 2006.

[27] J. E. Sharping, Y. Okawachi, and A. L. Gaeta, “Wide bandwidth slow light using a Raman fiber amplifier,” Opt. Express, vol. 13, pp. 6092, 2005.

[28] M. F. Yanik and S. Fan, “Stopping light all optically,” Phys. Rev. Lett., vol. 92, pp. 083901-1, February 2004.

[29] J. K. S. Poon, J. Scheuer, Y. Xu, and A. Yariv, “Designing coupled-resonator optical waveguide delay lines,” J. Opt. Soc. Am. B, vol. 21, pp. 1665, September 2004.

[30] I. Fazal, O. Yilmaz, S. Nuccio, B. Zhang, A. E.Willner, C. Langrock, and M. M. Fejer, “Optical data packet synchronization and multiplexing using a tunable optical delay based on wavelength conversion and inter-channel chromatic dispersion,” Opt. Express, vol. 15, pp. 10492–10497, 2007.

[31] A. H. Gnauck, C. R. Doerr, P. J. Winzer, T. Kawanishi, “Optical equalization of 42.7-Gbaud bandlimited RZ-DQPSK signals,” IEEE Photon. Technol. Lett., vol. 19, pp. 1442, October 2007.

[32] M. C. Cardakli, S. Lee, A. E. Willner, V. Grubsky, D. Starodubov, J. Feinberg, "Reconfigurable optical packet header recognition and routing using time-to-wavelength mapping and tunable fiber Bragg gratings for correlation decoding," IEEE Photon. Technol. Lett., vol. 12, pp. 552, May 2000.

[33] A. E. Willner, D. Gurkan, A. B. Sahin, J. E. McGeehan, M. C. Hauer, "All-optical address recognition for optically-assisted routing in next-generation optical networks," IEEE Communications Magazine, vol. 41, pp. S38, 2003.

[34] A. J. Poustie, K. J. Blow, A. E. Kelly and R. J. Manning, "All-optical parity checker with bit-differential delay," Optics Comm., vol. 162, pp. 37, April 1999.

[35] M. Soljacic, S. G. Johnson, S. Fan, M. Ibanescu, E. Ippen, and J. D. Joannopoulos, "Photonic-crystal slow-light enhancement of nonlinear phase sensitivity," J. Opt. Soc. Am. B, vol. 19, pp. 2052, 2002.

[36] H. Schmidt and R. J. Ram, "All-optical wavelength converter and switch based on electromagnetically induced transparency," Appl. Phys. Lett., vol. 76, pp. 3173, May 2000.

[37] Raul del Coso and J. Solis, "Relation between nonlinear refractive index and third-order susceptibility in absorbing media," J. Opt. Soc. Am. B, vol. 21, no. 3, pp. 640-644, 2004.

[38] G. P. Agrawal, *Nonlinear Fiber Optics*, The Netherlands: Elsevier, Amsterdam, 2009.

[39] G. Contestabile, M. Presi, and E. Ciaramella, "A fiber-based 1:6 WDM multicast converter at 10 Gbit/s," Opt. Commun., vol. 241, no. 4-6, pp. 499 - 502, November 2004.

[40] J. Wang, Q. Sun, and J. Sun, “All-optical 40 Gbit/s CSRZ-DPSK logic XOR gate and format conversion using four-wave mixing,” Opt. Express., vol. 17, no. 15, pp. 12555-12563, July 2009.

[41] J. Wang, S. R. Nuccio, J. Yang, X. Wu, A. Bogoni, and A. E. Willner, “High-speed addition/subtraction/complement/doubling of quaternary numbers using optical nonlinearities and DQPSK signals,” Opt. Lett., vol. 37, no. 7, pp. 1139-1141, April 2012.

[42] J. Liu, T. Cheng, Y. Yeo, Y. Wang, L. Xue, W. Rong, L. Zhou, G. Xiao, D. Wang, and X. Yu, “Stimulate Brillouin scattering based broadband tunable slow-light conversion in a highly nonlinear photonic crystal fiber,” IEEE J. Lightw. Technol., vol. 27, no. 10, pp. 1279 -1285, May 2009.

[43] N. Shibata, R. P. Braun, and R. G. Waarts, “Phase-mismatch dependence of efficiency of wave generation through four-wave mixing in a single-mode optical fiber,” IEEE J. Quantum Electronl., vol. 23, no. 7, pp. 1205 -1210, July1987.

[44] E. Mateo, F. Yaman, and G. Li, “Control of four-wave mixing phase-matching condition using the Brillouin slow-light effect in fibers,” Opt. Lett., vol. 33, no. 5, pp. 488-390, March 2008.

4 SBS SLOW-LIGHT-BASED FIBER-OPTIC SENSOR

Over the past twenty years the fiber-optic communications industry has greatly revolutionized the telecommunications industry by offering higher-performance, wider-bandwidth, and more reliable data transmission links with decreasing cost. The fast development of fiber-optic communications is boosted by the rapid growth in technology of optoelectronic devices, such as lasers, modulators, amplifiers, various types of fibers and so on. This revolution has brought many benefits to the users by building up the information superhighway.

On the other hand, in parallel with the developments in fiber-optic communications, fiber-optic sensor [1] technology has been well advanced since the technology shares almost the same components as those used in fiber-optic communications. Many of the components associated with fiber-optic communications are often employed for fiber-optic sensor applications. In turn, fiber-optic sensor technology has also promoted the development and subsequent mass production of components to support these industries. The potential of fiber-optic sensor in replacing other kinds of traditional sensors has been enhanced due to the reduction in component prices and the improvement on component quality. More and more optoelectronic devices become affordable, yet with better performance than before. One of the examples is the laser diode, which cost ~$3,000 in 1979 with lifetimes in hours is now sold at a few dollars and possesses a lifetime of tens of thousands of hours [1]. Another example is the single-mode fiber that costs $20/m in 1979, but now the price is reduced significantly to less than $0.1/m, with greatly enhanced optical and mechanical properties. Therefore, although in the early days, fiber-optic sensors were deployed in places where traditional sensors were marginal or nonexistent, the situation has been changing. Fiber-optic sensors are now widely deployed for measurements, such as electric and magnetic field measurement, temperature, strain, linear and angular position, humidity, viscosity, chemical measurements, etc. As these trends continue, the fiber-optic sensor technology will ensure a full frame of sensor networks around the world, providing prominent detection and measurement for nearly all fields of our life.

In this chapter, we will give an introduction to fiber-optic sensors in section 4.1 with an emphasis on the advantages of fiber sensors, their applications in various fields, and classifications of fiber sensors. Our focus will be on the SBS slow-light-based fiber-optic sensor. The principle is described in section 4.2 and its performance on temperature sensing of a whole segment of fiber is investigated in section 4.3.

4.1 Introduction to Fiber-Optic Sensors

After the invention of fiber, the community gradually discovered that fiber itself is a good material to sense external physical changes and hence its sensitivities were exploited to develop a variety of fiber sensors. In a fiber-optic sensor system, optical fibers not only serve as the sensing element, but also are responsible for the transport of the detected signals to the receiver end. Fiber-optic sensors have promising advantages over traditional sensors. The unique merits include the following [2]:

- Small size and weight
- Environmental robustness, water- and moist-proof
- Immunity to electromagnetic interference and radio frequency interference
- Capability of remote sensing and distributed sensing
- Safe and convenient; integration with signal transportation
- Capability of multiplexing and multiparameter sensing
- Large bandwidth and higher sensitivity
- Lower cost and economic effectiveness

Due to the excellent features of optical fiber sensors, they have found wide applications in human social activities and daily living, from industrial production to cultural activities, from civil engineering to transportation, from medicine and health care to scientific research, and from residence security to national defense [2]. Several examples of these applications include: to provide feedback signals for controlling operations, monitoring of stress and strain, vibrations, and temperature changes, detection and transmission of biochemical information, etc. Other applications are specified in Ref. [2] and they are quoted in the following "Fiber-optic sensors are widely used in manufacturing automation, production quality control; in oil well, tank, and pipeline monitoring, power system monitoring, and communication network monitoring; in building status monitoring and seismological observation; in navigation and vehicle status monitoring; in metrology and scientific instruments; in antiterrorist activities and intrusion alarming; and in many military applications."

Since there are plenty of methods to construct fiber-optic sensors, the classification of optical fiber sensors can be based on different mechanisms. The following classification is quoted from Ref. [2]:

1. *Basic effects of materials*: photoelastic effect and thermal photo effect (strain-induced and thermally induced refractive index change), thermal expansion of materials in optical path.
2. *Fiber interferometers*: Mach-Zehnder interferometers, Michelson interferometers, Fabry-Perot interferometers, Sagnac interferometers, Fizeau interferometer, and so on.
3. *Polarization dependences*: polarization maintaining fiber interferometers, strain-induced birefringence of the fiber, Faraday effect, and so on.
4. *Gratings and filters*: fiber gratings, spectral dependence of fiber couplers, wavelength converters, Doppler effect, and so on.
5. *Nonlinear optical effect and scattering*: Rayleigh scattering, Raman scattering, Brillouin scattering, Kerr effect, self-phase modulation and cross-phase modulation, and so on.
6. *Mode coupling*: mode coupling by evanescent field, axial mode coupling, and so on.

7. *Loss-related mechanism*: fiber attenuation, end coupling, fiber bending loss, and so on.
8. *Aided with transducers*: various mechanical structures to convert the measurands to parameters of sensor elements.
9. *Aided with external materials*: reactants and fluorescence.

Among different types of fiber sensors, we mainly discuss the fiber-optic sensor based on SBS in this thesis. In the following sections, we employ SBS slow light effect to construct fiber sensors for the monitoring of temperature for a whole segment of fiber. Distributed temperature and strain sensing based on SBS slow light are also demonstrated in Chapter 5.

4.2 Principle of Fiber-Optic Sensor based on SBS Slow Light

Characteristics of spontaneous and stimulated Brillouin scattering are determined mostly by the material properties of the optical fiber. According to Equation (2-5), the amount of Brillouin frequency shift is related to the acoustic velocity and the refractive index, which are dependent on both the temperature and the strain of the fiber. The temperature and strain dependence of the Brillouin frequency shift have been demonstrated in Reference [3-5]. And in Ref. [5] it shows that the Brillouin frequency shift has a linear relationship with both the temperature and strain. The relationship between the Brillouin frequency shift and the temperature and the strain can be expressed as [6]

$$\delta\nu_B = C_\varepsilon \delta\varepsilon + C_T \delta T \tag{4-1}$$

where $\delta\nu_B$, $\delta\varepsilon$, amd δT are the change of the Brillouin frequency shift, strain and temperature, respectively. C_ε and C_T are the strain and temperature coefficient, representing the slope of the Brillouin frequency shift change versus that of the strain and temperature.

Due to the temperature dependence of the Brillouin frequency shift, the time delay obtained in slow light is also temperature dependent. Hence temperature sensing can be realized by measuring the time delay. Here, we demonstrate such a fiber sensing scheme by measuring the delay of the probe pulse. Previously, fiber sensors based on Brillouin scattering have been realized with the configuration of Brillouin optical time-domain reflectometer (BOTDR) [7]. In addition, since the Brillouin gain/loss is temperature dependent, fiber sensors using the configurations of Brillouin optical time-domain analysis (BOTDA) [8] and Brillouin optical frequency-domain analysis (BOFDA) [9] have also been demonstrated. These conventional fiber sensors provide advantages of high resolution, long distance sensing, and large sensing range. Compared to BOTDR [7] and BOTDA [8], our scheme offers more straightforward implementation using an oscilloscope for the detection; in addition, the response is fast and the configuration is simple in comparison to BOFDA [9]. As the oscilloscope in our work has a temporal resolution of ~1 ps, a precise measurement can be obtained, resulting in a relatively high temperature sensitivity. More importantly, the scheme has the potential for use in distributed sensing.

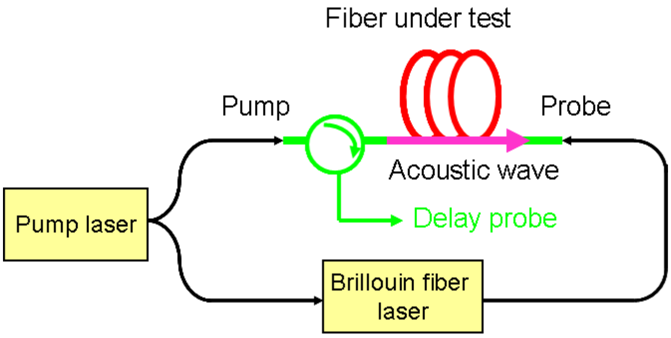

Fig. 4.1 Schematic illustration of the SBS slow light based temperature sensing scheme.

Fig. 4.1 illustrates our sensing scheme. A pump laser is divided into two branches. The upper branch serves as the pump for SBS slow light and the lower branch is used as the pump for a Brillouin fiber laser, as described in our previous work [10]. The Brillouin laser produces an output at the Stokes downshift frequency of the optical fiber used in the cavity. The output acts as probe pulses in SBS slow light. The slow light medium is a fiber under test and is of the same type of fiber used in the Brillouin laser. Hence, if the two fibers are at the same temperature, the probe frequency will be automatically aligned to the Stokes downshift frequency of the fiber under test. When the pump light is scattered by acoustic waves generated through electrostriction in the fiber, the probe is amplified and delayed by the slow light effect. The time delay induced by SBS slow light is given by Equation (3-8) as follows:

$$T_{del} = \Delta T_{\max} \cdot \frac{1-\delta^2}{(1+\delta^2)^2} = (\frac{g_0 P_p L}{\Gamma_B A_{eff}}) \cdot \frac{1-\delta^2}{(1+\delta^2)^2} \tag{4-2}$$

where g_0 is the Brillouin gain coefficient, L is the fiber length, P_p is the pump power, $\Gamma_B/2\pi$ is the gain bandwidth, A_{eff} is the fiber effective mode area, $\Delta\Omega=\omega_p-\omega_s-\Omega_B$ is the frequency detuning of the probe from the Stokes downshift frequency of the fiber under test with ω_p and ω_s as the frequencies of the SBS pump and probe, $\Omega_B=2\pi\nu_B$ as the Brillouin frequency shift, $\delta=\Delta\Omega/(\Gamma_B/2)$ is its normalized value, $\Delta T_{max}=g_0LP_p/(\Gamma_B A_{eff})$ is the maximum time delay. When ΔT_{max} is fixed, the delay will be determined only by the temperature dependent parameter δ, expressed as

$$\delta = \frac{\Delta\Omega}{\Gamma_B/2} = \frac{2C_T[MHz/^o C]\times(T-T_0)[^o C]}{(\Gamma_B/2\pi)[MHz]} \tag{4-3}$$

where C_T is the temperature slope coefficient of the Brillouin frequency shift, T is the temperature of the fiber under test, and T_0 is the room temperature. From Equation. (4-2) and (4-3), we can obtain temperature dependence of the delay. At the room temperature, $\delta=0$ and the probe frequency is located exactly at the Stokes downshift frequency, resulting in the maximum delay $T_{del}=\Delta T_{max}$. When the temperature is changed, the probe frequency will no longer be aligned to the Stokes downshift frequency, leading to different values of δ and hence different probe delays. The increase and decrease of the temperature will produce δ of opposite signs but will have the same effect on the delay. In our experiment, the fiber under test is heated from the room temperature while the delay of the probe pulse is measured. Note that if the temperature increase is sufficient to make $\delta>1$, the delay will be negative and result in fast light. The negative delay is caused by a reduction of the group index when the change in Stokes shift is sufficiently large and falls within a specific range. Our measurement is performed up to the fiber temperature that causes the probe pulse to experience a certain negative delay. However, we consider the temperature region for positive time delay ($0\leq\delta\leq1$) as our main sensing range. Hence, the frequency detuning $\Delta\Omega$ should meet $0\leq\Delta\Omega\leq\Gamma_B/2$ and thus $\Gamma_B/2$ determines the maximum sensing temperature.

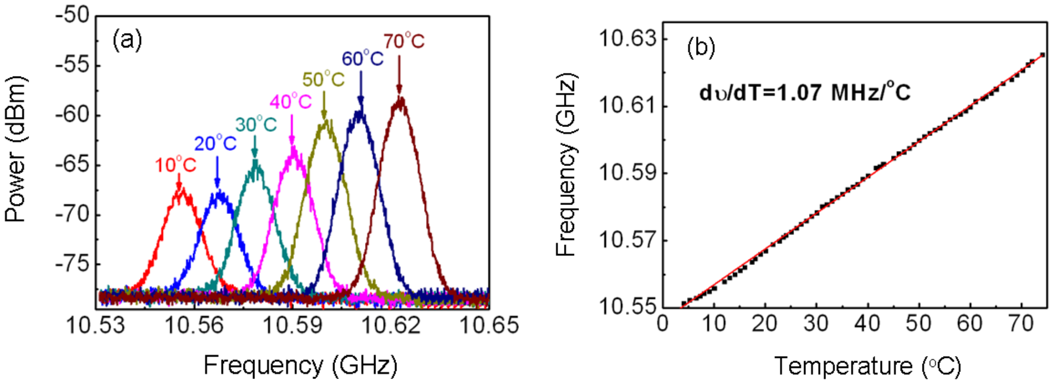

Fig. 4.2 (a) Measured Brillouin gain under different temperatures using the heterodyne method; (b) measured Stokes frequency shift versus temperature.

Before experimentally applying SBS slow light for sensing, we first measure temperature dependence of the Stokes frequency shift using the heterodyne method [11]. The Brillouin gain spectra at different temperatures displayed in Fig. 4.2 (a) reveal a slight reduction of the gain bandwidth as the temperature increases. As shown in Fig. 4.2 (b), the downshift frequency changes linearly with the temperature at a rate of C_T =1.07 MHz/°C from 4 to 75 °C.

4.3 Temperature Sensing by SBS Slow Light for a Whole Segment of Fiber

In this section, we employ the SBS based slow light to monitor the temperature of the fiber under test by measuring the time delay of the probe pulse. The demonstration is first carried on in a 100 m SMF with a CW pump to delay the probe pulse. Then the 100 m SMF is replaced by a 2 m SMF and the temperature sensing is achieved in this short fiber segment. To delay the probe pulse in such as short fiber, a pulsed pump is employed to increase the peak power of the pump. Experimental details on the measurement error, the temperature sensitivity, and the temperature resolution are provided.

4.3.1 Temperature Sensing for a 100 m Single-Mode Fiber

To investigate the performance, we employ a 100 m single mode fiber (SMF) as the fiber under test in the initial experiment, followed by replacing the fiber with a 2m SMF. Fig. 4.3 shows our setup. The CW pump laser at 1550 nm is split into two branches. An erbium-doped fiber amplifier (EDFA) is used in the lower branch to amplify the CW light that serves as the pump for a Brillouin fiber laser constructed with 40m SMF [10]. The amplified light is directed to a band pass filter to reduce the ASE noise. The output of the Brillouin fiber laser is intensity-modulated by an electro-optic intensity modulator (EOM) to produce a 50 ns triangular probe pulse. The pulse then propagates through the 100 m SMF under test, where SBS slow light is introduced by the counter-propagating CW pump in the upper branch. The delayed probe pulse is then detected by a photodetector and displayed on an oscilloscope. To ensure that there is only one probe pulse propagating within the 100m SMF, the repetition period is set to be 2 μs. With an initial gain fixed at 20, 30 or 40 dB in our experiment, we measure the output pulse profile and the delay of the pulse peak caused by slow light as the temperature is increased.

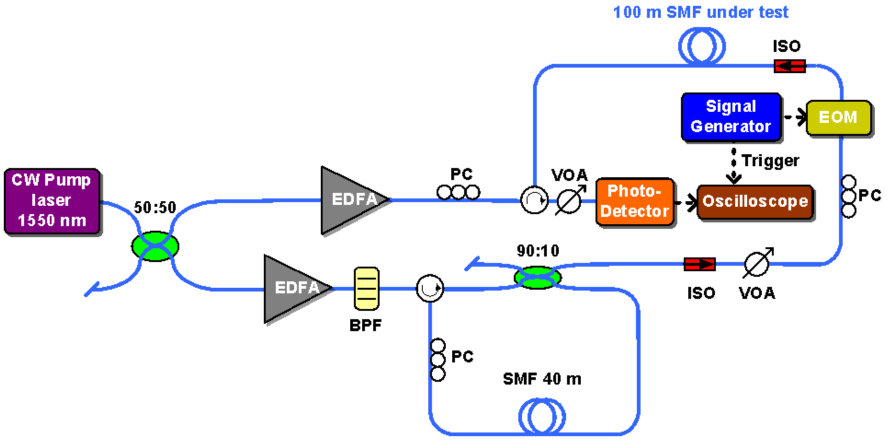

Fig. 4.3 Experimental setup for temperature sensing of 100 m SMF. PC: polarization controller; VOA: variable optical attenuator; BPF: band pass filter; EOM: electro-optic modulator.

The results are depicted in Fig. 4.4. The measurement is taken from 23.0 (room temperature) to 44.0 ^{o}C, but the main sensing range defined above is from 23.0 to 41.0 ^{o}C, limited by $\Gamma_B/2\pi$ ~40 MHz. Fig. 4 (a) shows the delayed probe pulse when the SMF is placed at different temperatures for an initial SBS gain of 30 dB. As the temperature increases, the pulse experiences a shorter delay. The pulse profile becomes more noisy and distorted owing to reduced gain and limited gain bandwidth. A maximum delay of 29.90 ns is achieved at room temperature and is shown as the blue curve in Fig. 4.4 (a). As predicted, the probe pulse shows a negative time delay when the temperature of the 100 m SMF is raised beyond 41.0 ^{o}C. The phenomenon also appears in the cases of 20 and 40 dB initial SBS gains, as shown in Fig. 4.4 (b). In the figure, we plot both the experimental data and the fitted curves of the delay versus temperature for different initial SBS gains. The fitted curves are obtained from Equation (4-2) and (4-3) using C_T =1.07 MHz/ ^{o}C, T_0=23.0 ^{o}C, $\Gamma_B/2\pi$=40 MHz and ΔT_{max}=20.40 ns, 29.90 ns and 40.00 ns obtained from the experimental data for initial SBS gains of 20, 30, and 40 dB, respectively. The corresponding temperature sensitivities (calculated from the linear part of the experimental data in Fig. 4.4 (b))

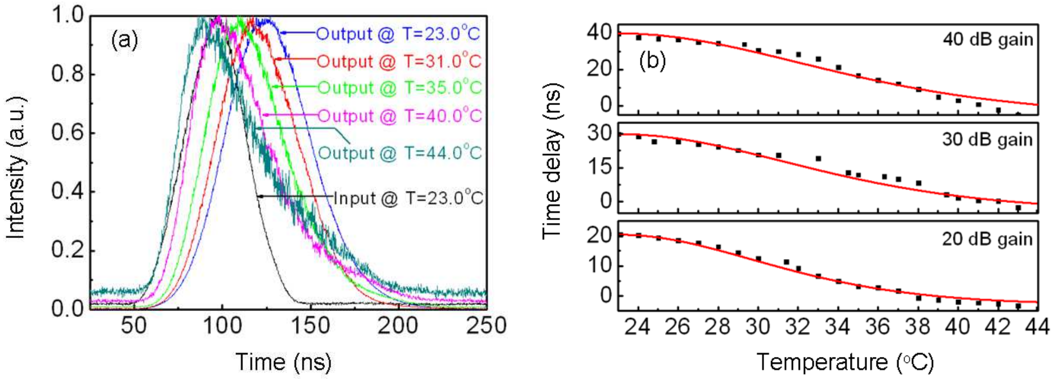

Fig. 4.4 Experimental setup for temperature sensing. PC: polarization controller; VOA: variable optical attenuator; BPF: band pass filter; EOM: electro-optic modulator.

of the delay are 1.45, 1.62, and 2.27 ns/^{o}C, respectively. Hence, a higher SBS gain is favorable in providing a higher temperature sensitivity. The fitted curves approximate the experimental data quite well except for a minor deviation occurring at high temperatures. The slight mismatch is mainly caused by the fact that the actual SBS gain bandwidth is not a constant under different temperatures, as shown in Fig. 4.2 (a). The impact of the dependence of SBS bandwidth on temperature and the measurement noise can be approximated by the root-mean-square (RMS) deviations between the experimental data and the fitted curves in Fig. 4.4 (b). We calculate the RMS deviations for 20, 30, and 40 dB initial gains and obtain the values of 0.88, 1.19, and 1.38 ns, respectively. With these data, the temperature resolution achieved for the corresponding gain values are 0.6, 0.7, and 0.6 ^{o}C. One should notice that the noise levels for these three cases are different because of different initial gains (the higher initial gain has larger noise). To improve the signal-to-noise ratio, the averaging function of the oscilloscope can be advantageously used [7].

4.3.2 Temperature Sensing for a 2 m Single-Mode Fiber

To investigate the approach for temperature sensing in a 2m SMF, it is necessary to employ a pulsed pump instead of a CW pump to warrant sufficient peak power to introduce SBS slow light. In the setup shown in Fig. 4.5, we add an electro-optic modulator together with a polarization controller to produce a pulsed pump that is synchronized with the probe pulse in the 2 m SMF. The repetition period of both the pump and probe pulses are 10 μs. The pump pulse is rectangular with a 100 ns width and is longer than twice of the pulse propagation time in the 2 m SMF. Consequently, the probe pulse sees a constant pump power while it propagates within the SMF [12]. The measurement results are shown in Fig. 4.6. Fig. 4.6 (a) depicts the delayed probe pulse when the 2 m SMF is maintained at different temperatures. The initial SBS gain is 20 dB and is the maximum initial gain that can be obtained from the 2 m SMF at room temperature (21.0 ^{o}C). The maximum delay is about 21.00 ns (shown as the blue curve in Fig. 4.6 (a)). Fig. 4.6 (b) shows the experimental data and the fitted curve relating the time delay and the temperature. The fitted curve is obtained using an approach similar to that of the case of 100 m SMF, except for some changes in parameters such as T_0=21.0 ^{o}C, $\Gamma_B/2\pi$=50 MHz and ΔT_{max}=21.00 ns.

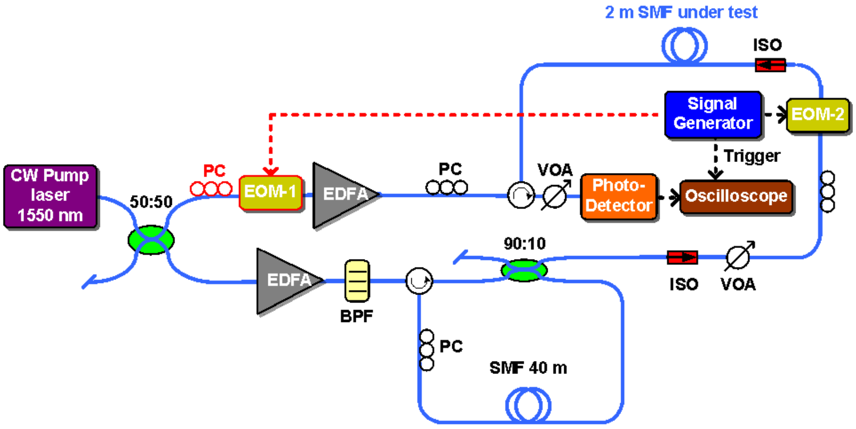

Fig. 4.5 Experimental setup for temperature sensing of 2 m SMF. PC: polarization controller; VOA: variable optical attenuator; BPF: band pass filter; EOM: electro-optic modulator.

The temperature sensitivity of the delay time is 0.90 ns/ ^{o}C and the RMS deviation between the experimental data and the fitted curve in Fig. 4.6 (b) is 0.65 ns. Hence, the achieved temperature resolution is 0.7 ^{o}C. In Fig. 4.6 (b), the measurement is taken from 21.0 to 50.0 ^{o}C but the main sensing range covers 21.0 to 46.0 ^{o}C. Compared to the results obtained from the 100 m SMF, the most noticeable change is the increase of the sensing range up to ~25 ^{o}C from the room temperature. The improvement is explained by the influence of the spectral width of the pump pulse. The spectral width of the CW pump in the 100 m SMF experiment can be neglected compared to the intrinsic SBS gain bandwidth ($\Gamma_B/2\pi$ ~40 MHz). However, the spectral width (~10 MHz) of the pulsed pump in the 2 m SMF experiment is of the same order of magnitude as the gain bandwidth. Thus, the effective SBS gain bandwidth should be obtained from the convolution of the pump spectrum and the intrinsic SBS gain spectrum [13], leading to an actual gain bandwidth of around ~50 MHz. Hence, the main temperature sensing range is increased.

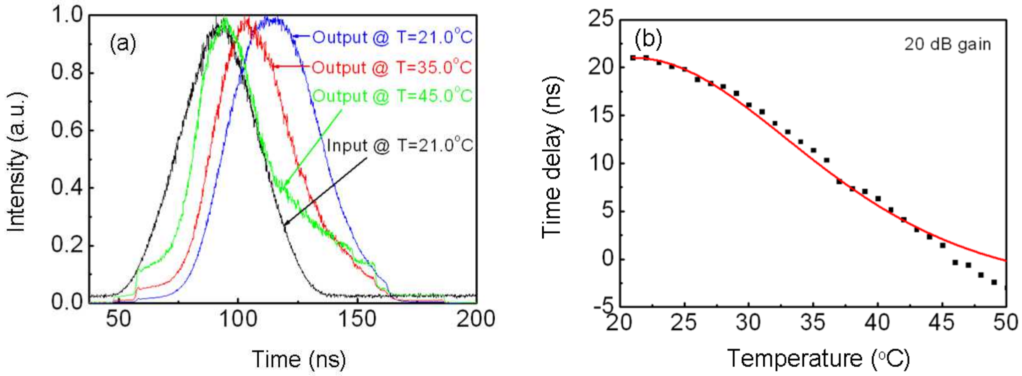

Fig. 4.6 (a) Measured output delayed pulses at different temperatures of the 2m SMF. (b) experimental data (dark squares) and fitted curves on the time delay versus temperature at 20 dB initial SBS gain.

To determine the sign of the temperature change, the experimental parameters can be modified to introduce a slight offset between the Brillouin resonance and the frequency of the probe pulse. An increase in temperature will cause the gain peak to shift to a longer wavelength. Hence, if the probe is placed on the long wavelength side of the Brillouin gain peak, an additional delay will be obtained. On the contrary, a temperature drop will result in a smaller amount of delay. It is worth mentioning that our SBS slow light scheme is potentially useful for distributed sensing in a long fiber. By tuning the delay between the pump and probe pulses, one can select the particular segment of fiber to be monitored. Consequently, dynamic profiling of the temperature can be achieved along the whole fiber. The implementation of this modified scheme is depicted in the next chapter.

It is worth mentioning that the fiber attenuation will affect the signal gain or loss, thus influence the accurate measurement of the gain or loss. While the time delay from slow light suffers less from the fiber attenuation because the original Brillouin gain rather than the real gain on the signal (related to fiber loss) determines the delay. Therefore, to measure the delay has better accuracy than to measure the gain or loss for temperature or strain sensing. We also should note that the temperature value in our experiment is measured by using a digital multimeter (UNI-T UT58E) which has a measurement range from -40°C to 1000 °C with a resolution of 1 °C. The specification of the temperature sensor in the multimeter is not given by the manufacturer, but from its temperature sensing range, it may be a R or S type thermocouple with an accuracy of ± 1 °C. Since the sensing fiber is under water which is heated and exposed to air, the temperature calibration would result in some errors. To improve the accuracy, it is better to use temperature oven to maintain the temperature.

In conclusion, using time domain analysis of the probe pulse, a new fiber sensor interrogation system has been achieved with SBS slow light. The temperature sensing approach has been demonstrated first in a 100 m SMF and subsequently in a 2 m SMF. The main temperature sensing range, limited by the intrinsic SBS gain bandwidth, is ~18 ^{o}C using a CW pump in the former configuration, and is ~25 ^{o}C using a pulsed pump in the latter configuration. Our scheme offers a relatively high temperature sensitivity and provides a resolution of 0.6 to 0.7 ^{o}C depending on the pump power and configuration.

References

[1] T. S. Yu, and S. Yin, *Fiber Optic Sensors*, MARCEL DEKKER, INC., 2002.

[2] Z. Fang, K. K. Chin, R. Qu, and H. Cai, *Fundamentals of Optical Fiber Sensors*, WILEY, 2012.

[3] D. Culverhouse, F. Farahi, C. N. Pannell and D. A. Jackson, "Potential of stimulated Brillouin scattering as sensing mechanism for distributed temperature sensors", Electron. Lett. **25**, 913-915 (1989).

[4] D. Culverhouse, F. Farahi, C. N. Pannell and D. A. Jackson, "Stimulated Brillouin scattering: a means to realize tunable microwave generator or distributed temperature sensor", Electron. Lett. **25**, 915-916 (1989).

[5] M. Nikles, L. Thevenaz, and P. A. Robert, "Brillouin Gain Spectrum Characterization in Single-Mode Optical Fibers," IEEE J. Lightw. Technol., vol. 15, no. 10, pp. 1842 – 1851, October 1997.

[6] T. R. Parker, M. Farhadiroushan, V. A. Handerek, and A. J. Rogers, "Temperature and strain dependence of the power level and frequency of spontaneous Brillouin scattering in optical fibers," Opt. Lett., vol. 22, no. 11, 787–789, June 1997.

[7] S. M. Maughan, H. H. Kee, and T. P. Newson, "57-km single-ended spontaneous Brillouin-based distributed fiber temperature sensor using microwave coherent detection," Opt. Lett., vol. 26, No. 6, 331-333 (2001).

[8] S. M. Lopez, M. A. Camas, F. Rodriguez, P. Cooredera, J. D. A. Castañon, L. Thévenaz, and M. G. Herraez, "Brillouin optical time-domain analysis assisted by second-order Raman amplification," Opt. Express., vol. 18, No. 18, 18769–18778 (2010).

[9] D. Garus, K. Krebber, F. Schliep, and T. Gogolla, “Distributed sensing technique based on Brillouin optical-fiber frequency-domain analysis” Opt. Lett., vol. 21, no. 17, 1402-1405 (1996).

[10] A. Cheng, M. P. Fok, and C. Shu, “Wavelength-transparent, stimulated-Brillouin-scattering slow light using cross-gain-modulation-based wavelength converter and Brillouin fiber laser” Opt. Lett., vol. 33, no. 22, 2596-2598 (2008)

[11] A. Yeniay, M.-M. Delavaux, and J. Toulouse, “Spontaneous and stimulated Brillouin scattering gain spectra in optical fibers,” J. Lightwave Tech., vol. 20, no. 8, 1425-1432 (2002).

[12] M. G. Herráez, K. Y. Song, and L. Thévenaz, “Optically controlled slow and fast light in optical fibers using stimulated Brillouin scattering,” App. Phys. Lett., vol. 87, 081113 (2005).

[13] M. G. Herráez, K. Y. Song, and L. Thévenaz, “Aibitrary-bandwidth Brillouin slow light in optical fibers,” Opt. Express., vol. 14, no. 4, 1395–1400 (2006).

5 DISTRIBUTED TEMPERATURE & STRAIN SENSING USING SBS-BASED SLOW LIGHT

Traditional single point sensors provide accurate detection of the measurand at the position where the sensors are deployed. Sometimes it is necessary to obtain the information of the measurand for multiple points at different locations. In this case, the number of single point sensors required to be installed should be sufficient to cover all the locations that need to be sensed. In another case, if the spatial distribution of the measurand is needed, then to deploy as many sensors as possible to achieve an adequate sampling of the distribution of interest seems to be a good choice. However, on one hand, the cost for large number of sensor arrays is high and the installation of these sensors is a big and complicated project; on the other hand, there is always the case that the information of the location between two sampling points is missed by the sensor array. Considering the cost and complexity, the number of the sensors installed is minimized, leading to inadequate sampling and hence insufficient information to retrieve the spatial distribution. Therefore, single point sensors are seldom used in the case where multiple locations or spatial distribution of the measurand needs to be measured.

In contrast, distributed fiber-optic sensors take the advantage of the high intrinsic bandwidth of the optical fibers and allow all locations along the long single optical fiber to be measured simultaneously. The distributed sensing scheme far exceeds the capacity of other schemes relying on multiplexing the measured results from all the single point sensors. In a distributed fiber-optic sensor system, the optical fiber not only acts as the sensing element, but also as the transmission medium for the detected signal. Since a large number of measured points share the same equipment, the cost of the equipment per measured point can be very low. In many practical cases, the cost of the distributed fiber-optic sensor is dominated by the cost of the fiber itself and the deployment of the sensor. As the price for optical fibers is reduced greatly due to the development of the technology, the cost mainly comes from the installation of the sensor system. The approach of distributed fiber-optic sensors provides an efficient way of simultaneously achieving multi-points sensing under a convenient and low-cost configuration.

Among the different types of distributed fiber-optic sensors, distributed Brillouin fiber sensors have attracted much research interest in the past two decades [2-11] and are now widely used in structural health monitoring. This chapter addresses the distributed temperature and strain sensing using the SBS-based slow light. The organization of this chapter is as follows: Section 5.1 gives a brief introduction to the distributed fiber-optic sensors based on Brillouin scattering; the configurations of distributed temperature and strain sensing based on SBS slow light are then described in Section 5.2 and 5.3, respectively. Both principles and experimental results are analyzed in detail.

5.1 Introduction to Distributed Brillouin Fiber Sensor

Characteristics of spontaneous and stimulated Brillouin scattering are determined mostly by the material properties of the optical fiber. The amount of Brillouin frequency shift is related to the acoustic velocity and the refractive index, which are dependent on both the temperature and the strain of the fiber. Based on this principle, Brillouin fiber sensors have been demonstrated using the Brillouin optical time-domain reflectometer (BOTDR) configuration [2]. In addition, owing to the temperature and strain dependence of the frequency shift, the Brillouin gain or loss is also temperature and strain dependent, giving rise to Brillouin gain/loss based sensors, such as the configurations for Brillouin optical time-domain analysis (BOTDA) [3-7] and Brillouin optical frequency-domain analysis (BOFDA) [8, 9]. The technique of Brillouin optical correlation-domain analysis (BOCDA) [10, 11] has also been used for Brillouin sensors to achieve centimetric resolution. These conventional Brillouin fiber sensors are promising for long distance sensing with high resolution.

Here, we give a detailed introduction to two typical implementations of distributed Brillouin fiber sensors [12]:

1. Brillouin optical time-domain reflectometer (BOTDR)

The main purpose of a distributed Brillouin fiber sensor is to obtain the distribution of the Brillouin frequency shift along the fiber, and hence retrieve the temperature and strain distribution. Since the BOTDR employs the spontaneous Brillouin scattering, it is very important to extract the Brillouin signal from the strong Rayleigh background. In order to avoid the interference from the Rayleigh scattered signal, heterodyne detection is usually used: the backscattered signal is mixed with the pump coherently at the photodetector end and their beat frequency is examined on a spectrum analyzer.

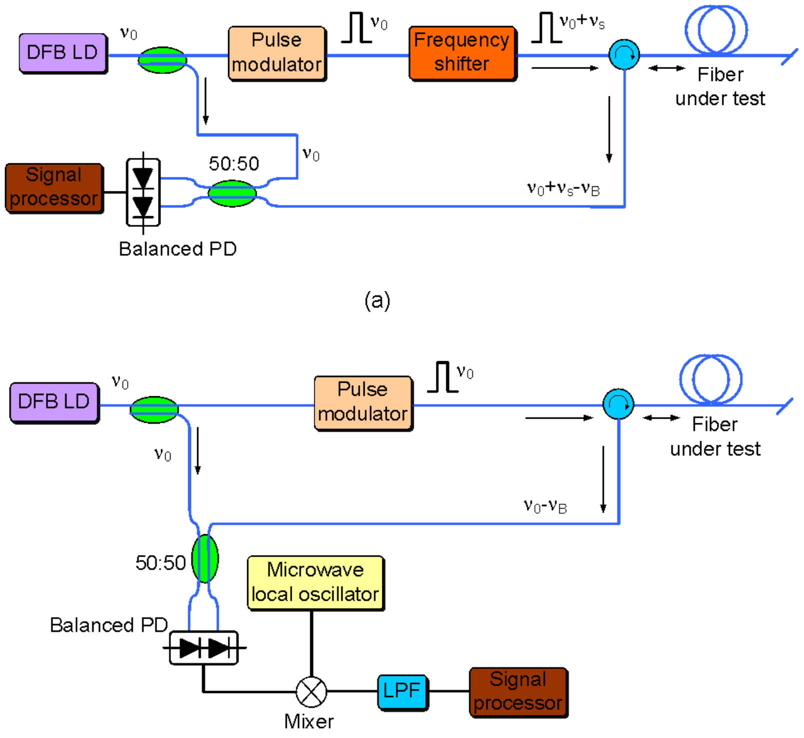

(a)

(b)

Fig. 5.1 Two similar configurations for BOTDR [12] (a) without local oscillator; (b)with local oscillator to avoid detection of signals at a high frequency.

Fig. 5.1 shows two basic BOTDR systems schematically [12]. In Fig. 5.1 (a), the output of a DFB laser diode is divided into two branches. The upper branch is modulated to generate an optical pulse which is frequency shifted to $\nu_0+\nu_s$ ($\nu_s \approx \nu_B$) and directed to the fiber under test after amplification. The backscattered signal with a frequency of $\nu_0+\nu_s-\nu_B$ is sent to the photodetector together with the pump wave through a 3-dB coupler. The arrival time of the backscattered signal determines the position of the sensing point and the beating frequency $\nu_B - \nu_s$ measured on a spectrum analyzer contains the temperature or strain information of the sensing point. Data acquisition for the beating frequency at different locations of the fiber under test is achieved and analyzed on the signal processor. Therefore, the distribution of the Brillouin frequency shift can be obtained along the whole fiber and the temperature or strain information is retrieved.

In Fig. 5.1 (b), the configuration is modified a little. The optical pulse is not frequency shifted, thus the beating frequency is at ν_B. As ν_B is generally around 11 GHz, a high-speed photodetector (or preferably a balanced photodetector) and an RF spectrum analyzer have to be used [2]. To avoid detection and analysis of signals at such a high frequency, a microwave local oscillator (LO) at a fixed frequency of ν_L is employed to mix the signal in the electrical domain again, as shown in the figure. Then the signal is analyzed by a spectrum analyzer before the data acquisition on the signal processor.

Several important parameters evaluate the performance of BOTDR systems in the practical applications: the spatial resolution, the frequency resolution, the measurement range, maximum fiber sensing length and the data acquisition time or response time. These parameters are generally in trade-off [12].

2. Brillouin optical time-domain analysis (BOTDA)

BOTDA makes use of the stimulated Brillouin scattering, and hence a pair of pump and probe is needed. Fig. 5.2 (a) shows the concept of a BOTDA system [12], where the output of a pulsed laser with a frequency of ν_0 is injected into the fiber under test from one end, and a cw output of a tunable laser is also directed to the fiber under test but from the opposite end. The frequency of the tunable laser is tuned to be $\nu_{cw}=\nu_0\pm\nu_B$, in which ν_B is the Brillouin frequency shift of the fiber under test. In the case of $\nu_{cw}=\nu_0+\nu_B$, the pulse will be amplified by SBS, whereas the cw beam experiences the loss due to the energy transfer to the pulse, which is usually called Brillouin loss [12]. On the other hand, if $\nu_{cw}=\nu_0-\nu_B$, the pulse will serve as the SBS pump and amplify the cw beam, called Brillouin gain. The intensity evolutions of the cw beam is detected by a photodetector and tracked on an oscilloscope or a computer-aided processor. Fig. 5.2 (b) and (c) give two basic configurations of BOTDA systems in practical applications [12]. The only difference between the two configurations is the source of the cw beam in Fig. 5.2 (a). In configuration (b) the cw beam is provided by another tunable laser (slave laser) whose frequency is tuned by an optical phase locked loop (OPLL). Both frequencies of the two lasers are monitored by a spectrum analyzer for the exact control of their frequency difference. While in configuration (c) only one laser is used. The cw beam is offered by one of the two divided outputs of the laser and is frequency shifted by carrier-suppressed modulation or other methods. The advantage of using only one laser lies in its stability of the frequency difference between the pump and probe, despite of the frequency drift of the laser itself. In both configurations, the cw beam has a frequency shift of ν_s from the optical pulse which has a frequency of ν_0. ν_s is adjusted around the Brillouin frequency shift of the fiber under test. For a given value of ν_s, the amplitude of the cw beam is recorded in the time domain by using a photodetector and an oscilloscope or a computer-aided data processor, thus the gain or loss experienced by the cw beam on each location can be analyzed. Then the frequency difference ν_s is scanned step-by-step and the local amplification or

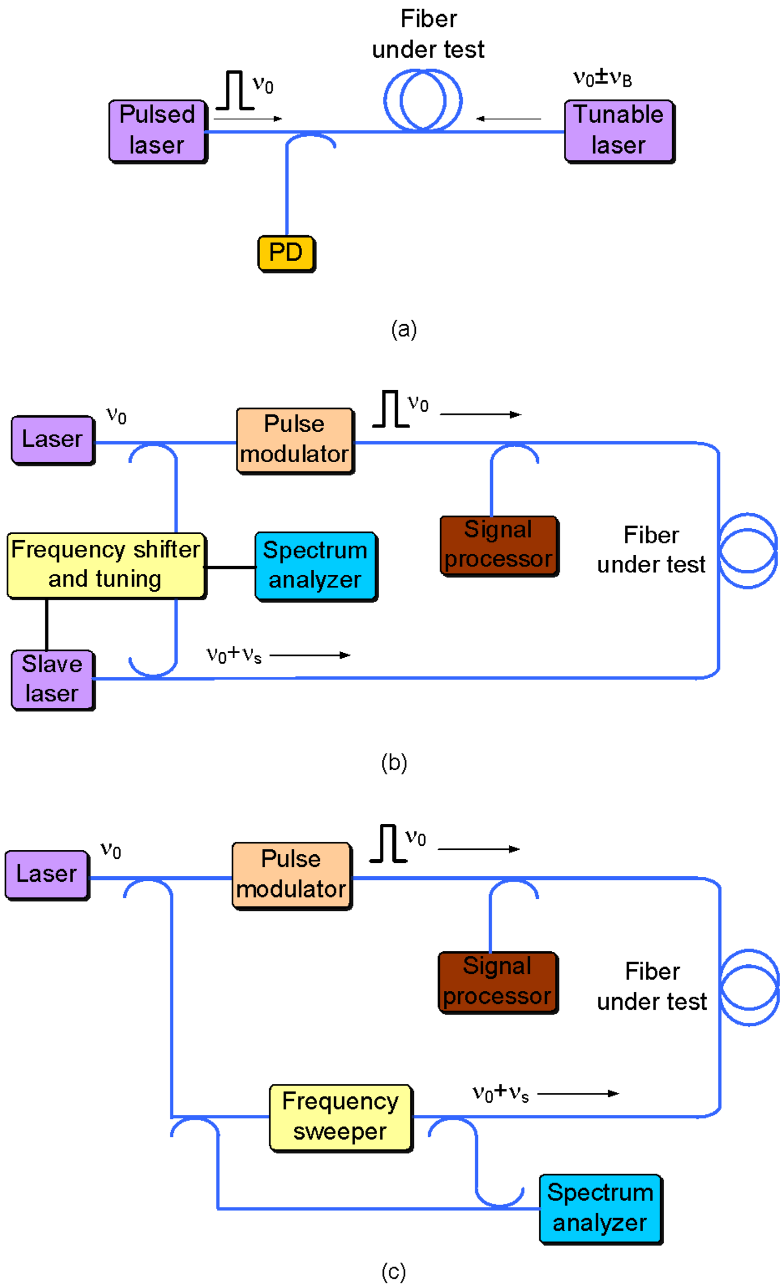

Fig. 5.2 (a) Concept of BOTDA; (b) and (c) two typical configurations of BOTDA systems [12].

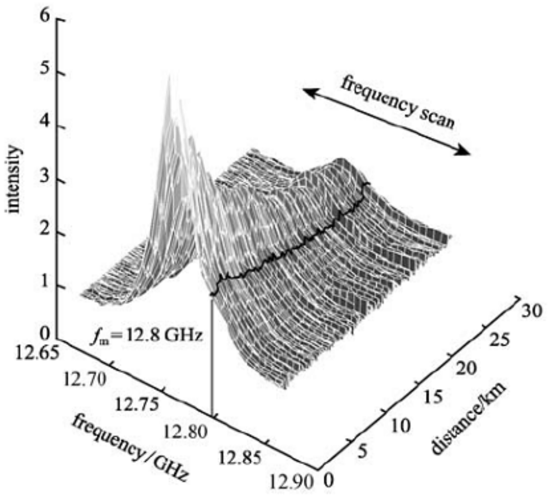

Fig. 5.3 Principle of data acquisition in a BOTDA system (local gain or loss is retrieved in time domain and converted into distance units; typical time trace for a pump-probe frequency difference set at 12.800 GHz is highlighted; local gain or loss spectrum at each position can then be reconstructed after a full frequency scan) [25].

depletion of the cw beam for each value of ν_s can be retrieved. After the scanning of ν_s, the acquired gain information at a given location as a function of frequency can be used to reconstruct the local gain spectrum. Fig. 5.3 shows a typical gain spectrum distribution for each position along the fiber after the frequency scanning [25]. At each location, the frequency with the highest gain indicates the Brillouin frequency shift of this point.

One of the advantages of BOTDA over BOTDR is the longer sensing distance, especially in case of $\nu_{cw}=\nu_0+\nu_B$, where the loss to the pulse can be compensated by the amplification, resulting in longer propagation distance. Similar to BOTDR, shorter pulse width is required to achieve higher spatial resolution. However, the signal-to-noise ratio (SNR) will be degraded for shorter pulses [12]. Additionally, a short pulse has broad spectrum which leads to lower precision of frequency measurement, the same problem also appearing in BOTDR. Several proposals have been demonstrated to improve the spatial resolution, such as the pre-pump [13], the double pulse [14], the dark pulse [15], and coded pulses [16]. Through theses schemes, the resolution has been enhanced to a value of centimeters. Other methods based on signal processing techniques are also proposed for the purpose of spatial resolution enhancement, e.g. the second-order partial derivative and the differential pulse-width pair schemes [17-19]. To improve the performance of BOTDA, other nonlinear effects, such as the parametric amplification, Raman amplification, and FWM are also employed to assist the sensing process [6, 20-23]. Furthermore, since SBS is polarization dependent, the effect of the polarization states on the measurement can be analyzed according to Reference [24] which gives a theoretical analysis on the polarization properties of Brillouin scattering.

In practical use of BOTDA, because temperature and strain have almost the same effect on the Brillouin frequency shift, it is needed to distinguish the two contributions separately. The power of the detected signal of BOTDA is affected by many factors, such as the amplification or loss due to SBS, fiber attenuation, etc. It is hard to use the power as a parameter to separate the two origins of Brillouin frequency shift change. In practice, two parallel fibers are paved in such a way that one of them is free of strain and used as a control element; another possibility is to use two fibers with different characteristics.

It is worth mentioning that commercial BOTDA products are now available, such as NBX-6000 series (NEUBREX Co., Ltd.) which has a spatial resolution of 2 cm, a temperature resolution of 0.3 ^{o}C, and a strain resolution of 7 με.

5.2 Distributed Fiber-Optic Temperature Sensor Using SBS-based Slow Light

Despite various applications of SBS based slow light in optical fiber communications, slow light is rarely associated with temperature or strain sensing. In Chapter 4, we have demonstrated the feasibility of fiber temperature sensing taking advantage of SBS based slow light, which is considered elsewhere as a penalty in traditional sensors [26]. The temperature was monitored by measuring the delay time of the probe pulse. A temperature resolution better than 1 ^{o}C was obtained. As mentioned in Chapter 4, compared to BOTDR and BOTDA, this scheme offers more straightforward implementation using an oscilloscope for the detection; in addition, the response is fast and the configuration is simple in comparison to BOFDA. More importantly, the scheme has the potential for use in distributed sensing. In this chapter, we further demonstrate the use of SBS slow light for distributed temperature sensing. By operating the pump in a pulsed mode and by controlling the relative delay time between the pump and probe pulses, dynamic measurement [27] can be obtained at any particular fiber location. That is to say, instead of static measurement of temperature or strain like conventional Brillouin sensors, this approach offers a potential means for fast dynamic real-time monitoring of a particular position. The temperature variation should be within a certain range (~25 ^{o}C in our case) where the probe frequency falls within the SBS gain bandwidth. On the other hand, for the measurement on static temperature distribution along the whole fiber, one just needs to combine the results obtained at different relative delay times.

5.2.1 Principle and Experimental Setup

Fig. 5.4 shows the working principle of our distributed temperature sensing scheme. A CW pump laser is divided into two branches. The upper branch is used for the generation of pump pulses for SBS slow light, whereas the lower branch is applied as the pump for a Brillouin fiber laser. The fiber laser output is modulated to produce a probe pulse for SBS slow light. The probe pulse operates at the Stokes frequency of the fiber in the Brillouin laser cavity, which is of the same type of fiber under test. The arrangement provides automatic spectral alignment for wavelength transparent slow light [28]. In our demonstration, we divide the fiber under test into three sections. The temperature of the middle section (section 2) is varied and the other two sections (sections 1 and 3) are maintained at the room temperature. The slow light effect is introduced in the fiber under test. The duration and the length of interaction are determined by the widths of the counter-propagating pump and probe pulses. If the two pulses cross at sections 1 or 3, the probe will experience the maximum delay because its frequency is automatically aligned to the Stokes frequency in the sections. If the two pulses cross at section 2, the probe pulse will experience a slow light delay dependent on the fiber temperature. The underlying principle is that the Brillouin frequency shift in section 2, hence the SBS gain of the probe, is determined by the temperature. By controlling the relative delay between the pump and probe pulses, the crossover point can be set at any arbitrary position along the fiber. One can monitor a fixed crossover point in real time. Certainly, through measuring the SBS probe delay for different crossover points, the temperature distribution along the whole sensing fiber can be observed.

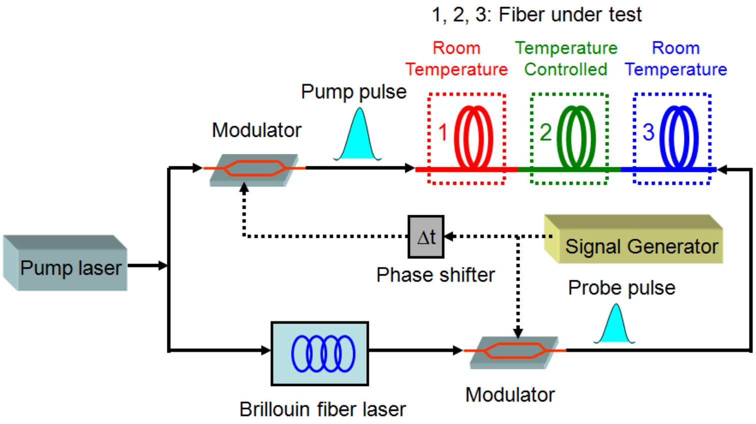

Fig. 5.4. Schematic illustration of the proposed distributed temperature sensing scheme based on SBS slow light.

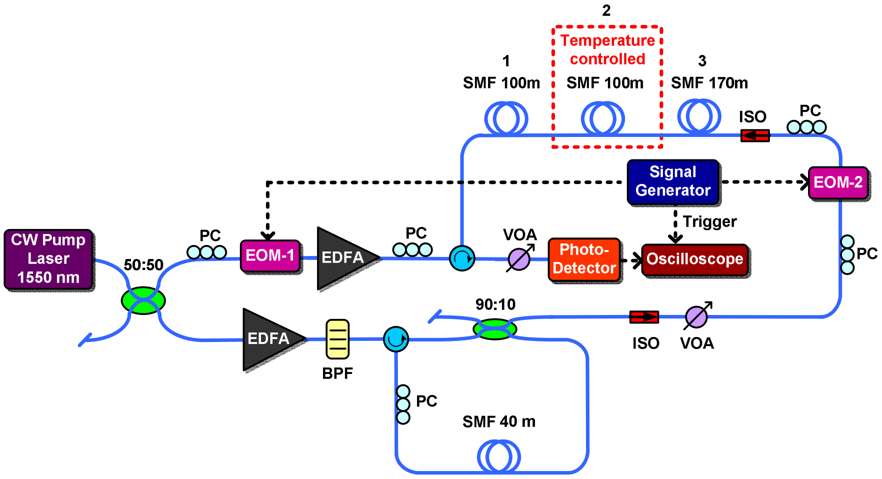

Fig. 5.5. Experimental setup for distributed temperature sensing. EOM: electro-optic intensity modulator; EDFA: erbium-doped fiber amplifier; PC: polarization controller; VOA: variable optical attenuator; BPF: band pass filter; SMF: single mode fiber; ISO: isolator.

The experimental setup is shown in Fig. 5.5. The composition of the fiber under test are two sections of 100 m single-mode fibers (SMFs) and one section of 170 m SMF. The temperature of the middle 100 m SMF section is varied during the experiment while the other two sections are kept at the room temperature. A CW pump laser at 1550 nm is split into two branches. The upper branch is intensity-modulated by an electro-optic intensity modulator (EOM-1) to provide a 100 ns pump pulse. After amplification, the polarization of the pump pulse is optimized with a polarization controller. Alternatively, a polarization scrambler can be used to minimize polarization-induced noise [29] as was demonstrated with strain sensing [30]. The lower branch is amplified to pump a Brillouin fiber laser constructed with 40 m SMF. The laser output is intensity-modulated by EOM-2 to produce a 50 ns probe pulse. The pump and probe pulses are synchronized with a repetition period of 20 μs. Their relative delay can be controlled by the electrical signal generator. The relative delay determines the crossover point of the two counter-propagating pulses in the fiber under test, where SBS slow light is introduced. The probe pulse is then measured by a photodetector connected to an oscilloscope to determine the SBS slow light delay.

5.2.2 Results and Discussion

Fig. 5.6 plots the profiles of the delayed probe pulses when the crossover of the pump and probe occurs at different positions along the fiber: length L=50 m, 150 m and 250 m, corresponding to crossover at section 1, 2, and 3, respectively. In this measurement, the temperature of section 2 is fixed at room temperature (22.4 ^{o}C). The red, green, and blue curves in Fig. 3 show that the probe pulses experience almost the same amount of delay. The result is expected as the three sections of the fiber under test are all maintained at the room temperature. The achievable maximum gain is ~20 dB and the maximum delay time is ~20.0 ns. The output profiles appear to be smoother than the input one because the number of average used in the measurement is four times that of the input. Next, we change the temperature of section 2 to 26.0, 30.0, 35.0 and 41.0 ^{o}C and repeat the measurement. The delayed probe pulses are shown in Fig. 5.7. The SBS delay is almost unchanged (~20.0 ns,

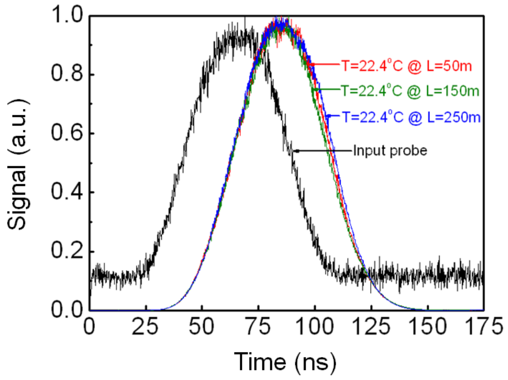

Fig. 5.6. Measured output probe pulses for three different crossover (sensing) points at section 1 (L=50 m), section 2 (L=150 m), and section 3 (L=250 m) when section 2 is maintained at room temperature.

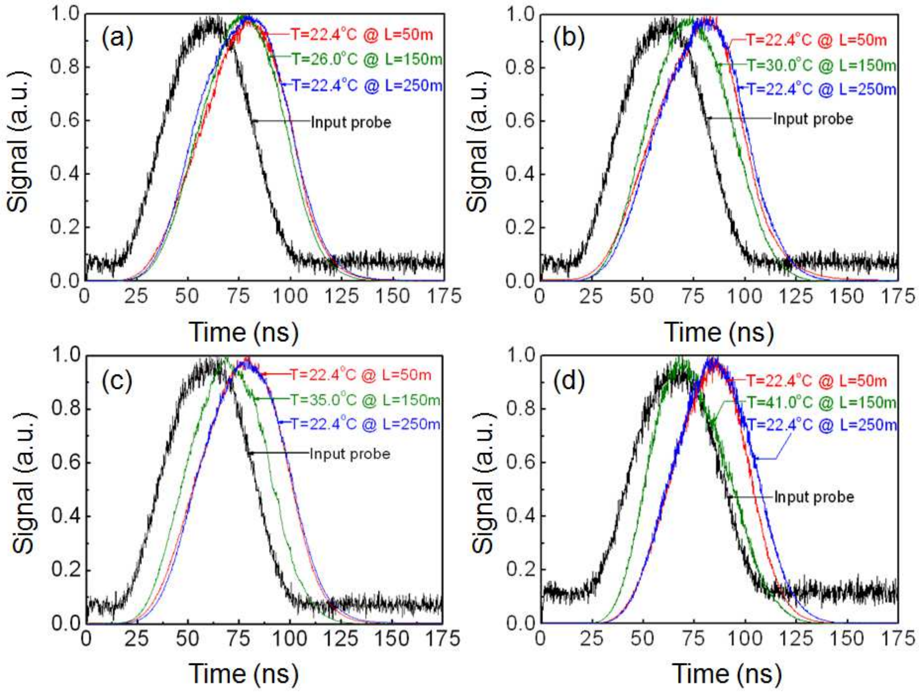

Fig. 5.7. (a)-(d) Measured output probe pulses for crossover (sensing) points at the three sections of fibers when section 2 is maintained at (a) 26.0, (b) 30.0, (c) 35.0, and (d) 41.0 ^{o}C.

shown as the red and blue curves) for the cases when the crossover occurs at section 1 or 3. However, the delay is reduced when the crossover is at section 2 as the temperature is increased. The results are displayed as the green curves. From both Fig. 5.6 and Fig. 5.7, at fixed crossover points (fiber length L=50 m, 150 m and 250 m), we can expect the potential of this scheme for dynamic real-time monitoring. A slight distortion of pulses is observed and is attributed mainly to the limited SBS gain bandwidth. The signal-to-noise ratio (SNR) can be further improved by increasing the averaging times (64 averaging times in our results) on the oscilloscope.

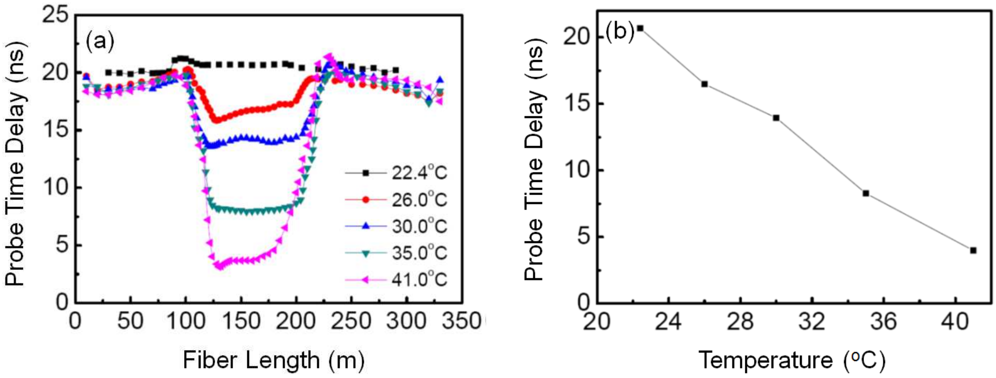

Fig. 5.8 (a) Delay time of the probe pulse when the pump and probe pulses cross over at different positions along the sensing fiber. The temperatures of section 2 are set at 22.4, 26.0, 30.0, 35.0, and 41.0 ^{o}C, respectively; (b) average values of the SBS probe delay at section 2 as derived from the data in (a).

To obtain the static temperature distribution along the sensing fiber, we also measure the SBS probe delay for other crossover positions. The measurement steps vary from 2 to 10 m, depending on the temperature gradient at the particular position. For each set of measured data along the sensing fiber, an average was taken over every five measurement positions for three times in order to minimize the effect of noise. Fig. 5.8 (a) shows the SBS probe delay for different crossover positions along the fiber under test when section 2 is maintained at five different temperatures. One can clearly distinguish the delay time at section 2 from those at sections 1 and 3. The spatial resolution of our sensing technique is determined by the overlapping distance of the pump and probe pulses along the fiber where the interaction takes place [31]. The resolution is theoretically calculated to be ~15 m as determined from the product of the group velocity and the average of the pump and probe pulse widths. The number is only a conservative estimation since the calculated distance includes the whole duration of partial and complete overlapping of pulses. Actually the more exact spatial resolution should be obtained from the falling and rising edges in Fig. 5.8 (a). Since the data in Fig. 5.8 (a) are averaged, we retrieve the more exact resolution from the initial experimental measurement of delay distribution along the sensing fiber. The initial delay time for each crossover point is the one measured from the oscilloscope without any post-processing such as averaging over every five measurement positions for three times. And the experimental resolution is found to be around 12 m, which is smaller than the one shown in Fig. 5.8 (a) since the averaging processing broadens the falling and rising edges. Certainly, the spatial resolution can be improved by using shorter pulses. However, on one hand, a shorter probe pulse will imply a broader spectral width, resulting in pulse distortion due to the limited SBS gain bandwidth. The width of the shortest probe pulse that can be delayed is ~20 ns under the intrinsic SBS gain bandwidth. The pulse distortion affects the accuracy and hence limits further improvement of the spatial resolution. The technique employing a phase modulated pump may be applied for the delay of picosecond probe pulses. However, it will lead to a decrease of temperature sensitivity unless higher pump power is used to compensate for the decreased gain coefficient. On the other hand, to further improve the spatial resolution, the pump pulse width can be reduced but the situation is somewhat complex. The decrease of the pump pulse width will give rise to a reduction of the gain coefficient. Hence, it is again necessary to raise the pump power to maintain the same temperature sensitivity. However, a large pump power will degrade the sensing performance due to the occurrence of other nonlinear effects such as self phase modulation. As the pump pulse width is less than 100 ns, the transient regime of SBS should be considered [32]. When the width is shorter than the phonon life time (typical value < 10 ns in SMF), SBS eventually ceases to occur. Thus, without relying on phase modulation of the pump wave, the optimal combination on the widths of the pump/probe pulse pair seems to be ~10/20 ns to achieve ~3 m spatial resolution. As described above, several joint effects need to be carefully considered. The optimal width combination of the pump/probe pulse pair is under investigation. Fig. 5.8 (b) shows the average values (20.68, 16.49, 13.95, 8.28, and 3.99 ns) of the SBS probe delay at section 2 versus the five temperatures. Limited by the SBS gain bandwidth, the temperature sensing range is ~25 ^{o}C from the room temperature, similar to that of the 2 m SMF configuration reported in Ref. [33]. Like most of the approaches [3, 4, 7, 11] used in calculating temperature (strain) resolution, we obtain the temperature resolution from the ratio of the measurement error and the temperature sensitivity. From the result, we achieve a temperature sensitivity of 0.90 ns/^{o}C. The measurement error can be approximated by the root-mean-square (RMS) deviations between the experimental data and the calculated result. The error is found to be ~0.60 ns. Hence a temperature resolution of 0.7 ^{o}C is obtained. The resolution can be enhanced by increasing the temperature sensitivity or reducing the measurement error. To improve the sensitivity, one can increase the pump power to enhance the SBS gain and thus the time delay of the probe pulse. To reduce the measurement error, several factors should be considered. The error can originate from pump power fluctuations, polarization-induced pulse distortion [29], and intensity noise transferred from the instability of the Brillouin fiber laser [28]. These factors can result in fluctuations of the probe pulse delay and hence inaccuracy of the measurement. Therefore, a laser with a steady output power, a polarization scrambler, and a stable Brillouin fiber laser cavity should be employed together with the averaging function of the oscilloscope. In addition, probe pulse distortion due to limited SBS gain bandwidth will cause difficulties in determining the delay time, hence contributing to measurement error. Wider probe pulse will experience less distortion and improve the accuracy; however, the spatial resolution will be sacrificed. A trade-off should thus be adopted according to practical considerations.

It is worth mentioning that the measurable range of temperature can be enlarged by slightly modifying the configuration. A wavelength-tunable pump laser can be used and the Brillouin fiber laser can be replaced by a probe laser at a fixed wavelength. By applying pump pulses at different wavelengths, each defining a unique measurable range of temperature in our setup, the total sensing range can be enhanced. Alternatively, the setup in Fig. 5.5 can also be directly applied to enlarge the measurable range of temperature simply by maintaining the Brillouin fiber laser cavity at different temperatures. Each selected temperature sets the reference for the starting point of a temperature sensing range.

Additional issues should be considered in practical application. To determine the sign of temperature change, the system can work either along the rising slope or falling slope of SBS resonance by detuning the probe wavelength, instead of setting it at the peak gain. Also, to decouple the effects of Brillouin frequency shift and pump power variation on the SBS delay, one may need to measure independently the received pump power at the opposite end of the fiber. Alternatively, a wavelength-tunable probe can be used to obtain a profile of the delay along the fiber at different wavelengths. A variation of pump power causes a proportional change in the SBS delay but the spectral peak position remains unchanged, whereas a temperature variation affects both the SBS delay and the peak position. The maximum sensing distance in our scheme is limited by fiber attenuation as it affects the pump power level and subsequently the probe pulse delay. For short distance real-time monitoring within hundreds of meters, the effect of fiber loss can be neglected. Otherwise, to extend the sensing distance, in-line Raman amplifiers [5] may be used to compensate for the optical loss.

In conclusion, by measuring the SBS slow light delay of a probe pulse at different positions along the fiber, a new distributed temperature sensing scheme is realized. The scheme offers an alternative method of monitoring the temperature in a distributed manner, demonstrating the potential of real-time monitoring of specific positions in a short fiber link. The limitations of this scheme are also discussed and analyzed. The spatial resolution can be enhanced by using shorter pump and probe pulses, and higher temperature resolution is achievable with a stronger SBS pump and better control on the power stability.

5.3 Distributed Fiber-Optic Strain Sensor Using SBS-based Slow Light

Since the Brillouin frequency is also sensitive to the strain, the SBS-based slow light fiber-optic sensor can also be used to monitor the strain along the sensing fiber, realizing distributed strain sensing. In this section, the performance of the fiber-optic sensor using SBS-based slow light for distributed strain sensing is investigated.

5.3.1 Principle and Experimental Setup

Similar to the temperature sensing using SBS based slow light, the fundamental principle here is strain dependence of the Brillouin frequency shift in a fiber, hence the delay time of an input probe pulse as a result of SBS based slow light. The strain dependence of the delay time is governed by the following equations:

$$T_{del} = \Delta T_{\max} \cdot \frac{1-\delta^2}{(1+\delta^2)^2} = (\frac{g_0 P_p L}{\Gamma_B A_{eff}}) \cdot \frac{1-\delta^2}{(1+\delta^2)^2} \tag{5-1}$$

$$\delta = \frac{\Delta\Omega}{\Gamma_B / 2} = \frac{2C_\varepsilon[MHz/\mu\varepsilon]\times(\xi-\xi_0)[\mu\varepsilon]}{(\Gamma_B/2\pi)[MHz]} \tag{5-2}$$

The definitions of the parameters in Equation (5-1) and (5-2) are the same as those in Equation (4-2) and (4-3), except C_ε is the strain coefficient of the Brillouin shift, ξ is the strain on the fiber under test, and ξ_0 is its initial value (generally set to zero microstrain).

Fig. 5.9 shows the working principle of our distributed strain sensing scheme. A CW pump laser is divided into two branches. The upper branch is used for the generation of pump pulses for SBS slow light, while the lower branch is applied as the pump for a Brillouin fiber laser. The fiber laser output is used to produce the probe pulse for SBS slow light. The probe pulse operates at the Stokes frequency of the fiber used in the Brillouin laser, which is of the same type of fiber under test. The arrangement provides automatic spectral alignment for wavelength transparent slow light [28]. In our demonstration, we divide the fiber under test into three sections. The strain of the middle section (section 2) is varied and the other two sections (sections 1 and 3) are kept loose as the reference fibers. The slow light effect is introduced inside the fiber under test. The duration and the length of interaction are determined by the widths of the counter-propagating pump and probe pulses. If the two pulses meet at sections 1 or 3, the probe will experience the maximum delay because its frequency is automatically aligned to that of the Stokes wave in the sections. If the two pulses meet at section 2, the probe will experience a delay that is dependent on the strain in the fiber. The underlying principle is that the Brillouin frequency shift in section 2, hence the SBS gain of the probe, is determined by the strain in the fiber. By controlling the relative delay between the pump and probe pulses, the crossover point

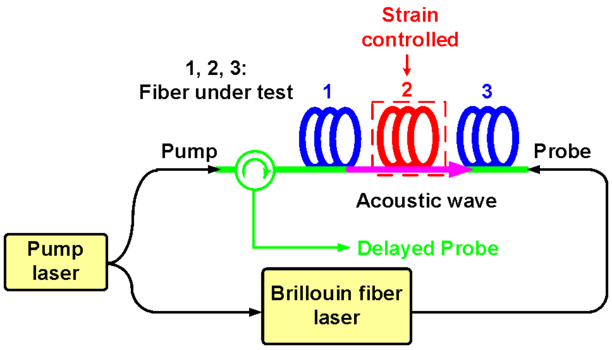

Fig. 5.9. Schematic illustration of the proposed distributed strain sensing scheme using SBS based slow light.

can be set at any arbitrary position. Through measuring the SBS delay for the cases of different crossover points, the strain distribution along the whole sensing fiber can be retrieved.

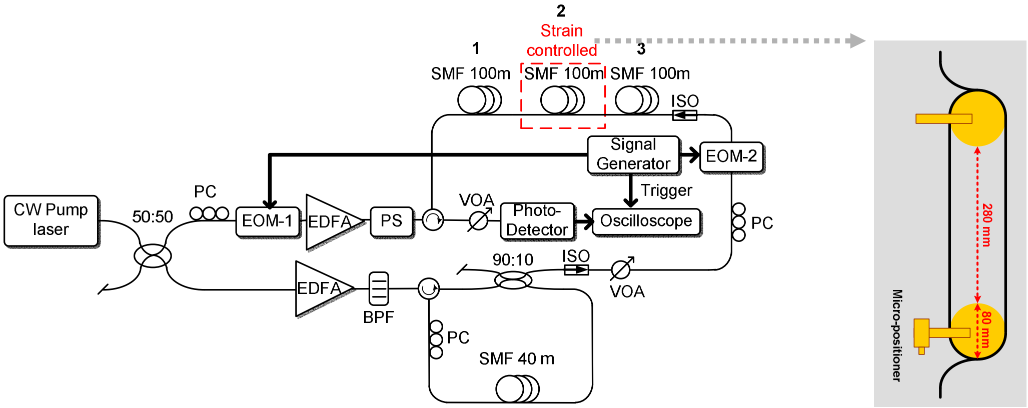

Fig. 5.10. Experimental setup for distributed strain sensing. Inset: schematic illustration of strain control in section 2. EOM: electro-optic intensity modulator; EDFA: erbium-doped fiber amplifier; PC: polarization controller; VOA: variable optical attenuator; BPF: band pass filter; SMF: single mode fiber; ISO: isolator; PS: polarization scrambler.

The experimental setup is shown in Fig. 5.10. A CW pump laser at 1550 nm is split into two branches. The upper branch is modulated by an electro-optic intensity modulator (EOM-1) to provide a 100 ns rectangular pump pulse. After an amplification, the pump pulse passes through a polarization scrambler to minimize the polarization-induced noise [29] which will otherwise result in fluctuations of the SBS probe delay and thus the accuracy of our scheme. The lower branch is amplified to pump a Brillouin fiber laser constructed with 40 m SMF. The laser output is intensity-modulated by EOM-2 to produce a 50 ns probe pulse. The pump and probe pulses are synchronized at 50 kHz repetition frequency and their relative delay can be controlled by the signal generator. The relative delay determines the crossover point of the two counter-propagating pulses in the fiber under test, where SBS slow light is introduced. The probe pulse is then measured by a photodetector and displayed on an oscilloscope for the determination of SBS slow light delay. The compositions of the fiber under test are three sections of 100 m single mode fibers (SMFs). During the experiment, variable strain is applied to the middle 100 m SMF section wound around a couple of plastic drums with a diameter of 80 mm. One of the drums is supported by a micro-positioner of which the movement controls the strain value. The other two sections of 100 m SMF are free from strain, serving as reference fibers.

5.3.2 Results and Discussion

Fig. 5.11 plots the delayed probe pulses when the crossover of the pump and probe occurs at different positions along the fiber: length L=50 m, 150 m and 250 m, corresponding to crossover at section 1, 2, and 3, respectively. The red, green, and blue curves in Fig. 5.11 (a) show that the probe pulses experience almost the same amount of delay. The result is expected as the three sections of the fiber under test are all free from strain. The achievable maximum delay time is ~14.0 ns. Next, we adjust the strain in section 2 to 169, 280, and 364 με respectively and repeat the measurement. The delayed probe pulses are shown in Fig. 5.11 (b)-(d). The SBS delay is almost unchanged (~14.0 ns, shown as the red and blue curves) for the cases when the crossover occurs at section 1 or 3. However, the delay is reduced when the crossover is at section 2 as the strain is increased. The results are displayed as the green curves. In Fig. 5.11, a slight distortion of pulses is observed and is attributed mainly to the limited SBS gain bandwidth. The signal-to-noise ratio (SNR) can be further improved by using the averaging function in the oscilloscope. Note that if there are strains applied on all the three sections at the same time, the red and blue curves in Fig. 5.11 will exhibit delays shorter than 14.0 ns. The amount of delays will depend on the exact strain values.

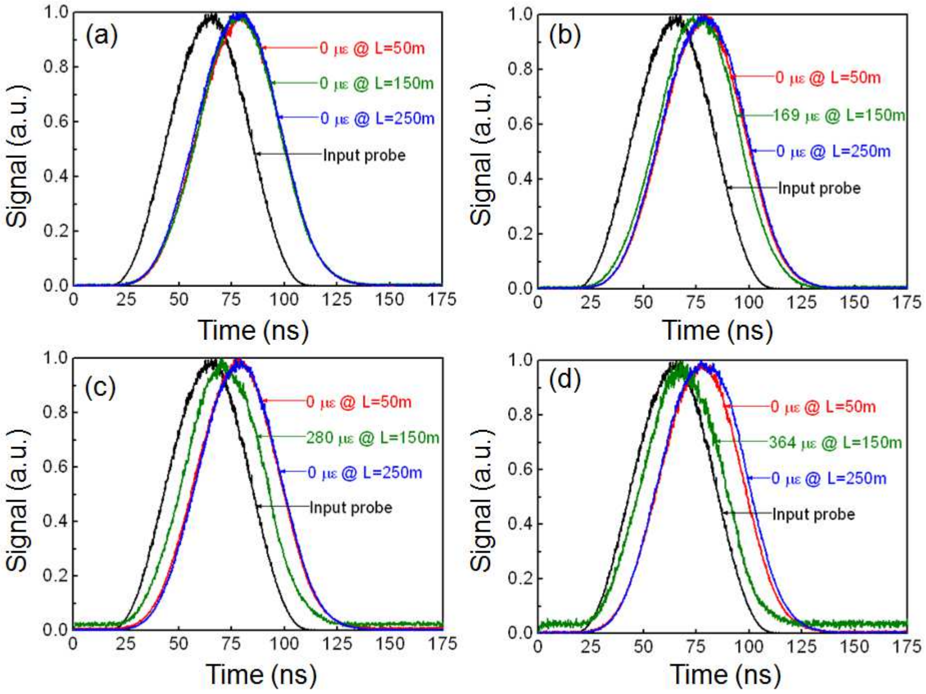

Fig. 5.11. (a)-(d) Measured output probe pulses for three different crossover (sensing) points at section 1 (L=50m), section 2 (L=150m), and section 3 (L=250m) when the strain in section 2 is maintained at (a) 0, (b) 169, (c) 280, and (d) 364 $\mu\varepsilon$.

For distributed strain sensing, we also measure the probe delay time at other crossover positions. For each set of measured data along the sensing fiber, an average was taken over every five measurement positions for three times in order to minimize the effect of noise. Fig. 5.12 (a) shows the delay time of the probe pulse when section

2 is maintained at four different strains. One can clearly distinguish the delay time at section 2 from those at sections 1 and 3. The average values (14.06, 9.66, 5.48, and 3.62 ns) of the delay times at section 2 versus the four strain levels are shown in Fig. 5.12 (b). The spatial resolution of our sensing technique is calculated using the same method as the distributed temperature sensing, that is ~15 m. And the improvement of the spatial resolution has already been discussed in the previous section for distributed temperature sensing. Here we do not repeat the discussion.

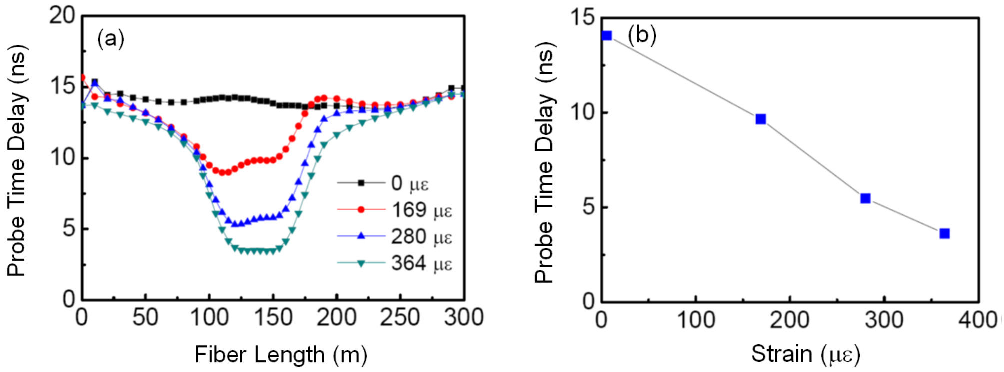

Fig. 5.12. (a) Delay time of the probe pulse when the pump and probe pulses cross at different positions along the sensing fiber. The strains in section 2 are set at 0, 169, 280, and 364 με respectively; (b) average values of the delay times at section 2 as derived from the data in (a).

In a subsequent experiment we investigate the measurement error, the strain sensitivity, and the strain resolution. We apply different strains on section 2 and record the probe delay versus the strain when the crossover point is fixed at L=150 m, the center position of section 2. The experimental data are shown as the dark squares in Fig. 5.13. The strain sensitivity of the delay is ~0.03 ns/με (calculated from the linear part of the experimental data in Fig. 5.13). The blue curve in Fig. 5.13 shows the simulated relationship between the probe delay and the strain at section 2. The simulation is based on Equation (5-1) and (5-2) using strain coefficient C_ε=0.048 MHz/με [34], initial strain ξ_0=0 με, SBS gain bandwidth

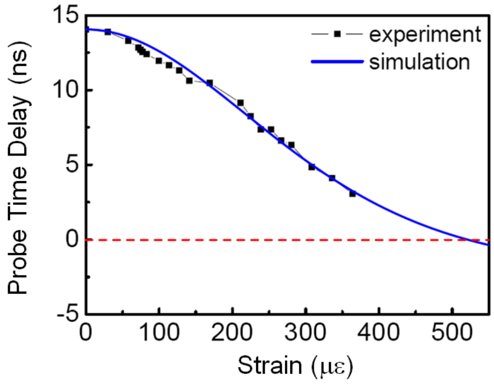

Fig. 5.13. Experimental data (dark squares) and simulated curve on the probe delay time versus the strain at section 2 when the pump and probe crossover is fixed at L=150 m.

$\Gamma_B/2\pi$=50 MHz [33], and maximum delay time ΔT_{max}=14.06 ns (obtained from our experiment). Limited by the SBS gain bandwidth, the maximum strain sensing value is ~520 με as the delay time will become negative owing to fast light beyond this strain value. Similar to Ref. [33], the measurement error can be approximated by the RMS deviations between the experimental data and the simulated result. The error is found to be 0.40 ns. Like the approach in calculating temperature resolution, we take the ratio of the measurement error and the strain sensitivity to obtain the strain resolution. The result is ~13 με. The resolution can be enhanced by increasing the strain sensitivity or reducing the measurement error. The resolution enhancement has already been discussed in the previous section for distributed temperature sensing. Here we do not repeat the discussion again.

Additional issues should be considered in practical application, including the enlargement of the measurable range of strain values, extension of maximum sensing distance, the sign of strain change, and decoupling of the effects of Brillouin frequency shift and pump power variation on the SBS delay. These issues have been studied in detail in the previous section for distributed temperature sensing.

In conclusion, by measuring the delay time of a probe pulse for the cases of different pump-probe crossover positions along the fiber, a distributed strain sensing scheme has been demonstrated using SBS based slow light. Three sections of fibers are used in the setup to demonstrate our scheme. The sensing scheme has been analyzed by a combination of experiment and simulation. We achieve a spatial resolution of 15 m and a strain resolution of 13 με. Our scheme is simple to realize and is practical for accurate monitoring of the strain.

References

[1] K. T. V. Grattan, and B. T. Meggitt, *Optical Fiber Sensor Technology (Advanced Applications–Bragg Gratings and Distributed Sensors),* Kluwer Academic Publishers, 2000.

[2] S. M. Maughan, H. H. Kee, and T. P. Newson, “57-km single-ended spontaneous Brillouin-based distributed fiber temperature sensor using microwave coherent detection,” Opt. Lett., vol. 26, no. 6, pp. 331-333, March 2001.

[3] X. Bao, D. J. Webb, and D. Jackson, “32-km distributed temperature sensor based on Brillouin loss in an optical fiber,” Opt. Lett., vol. 18, no. 18, pp. 1561-1563, September 1993.

[4] H. Liang, W. Li, N. Linze, L. Chen, and X. Bao, “High-resolution DPP-BOTDA over 50 km LEAF using return-to-zero coded pulses,” Opt. Lett., vol. 35, no. 10, pp. 1503-1505, May 2010.

[5] F. R. Barrios, S. M. López, A. C. Sanz, P. Corredera, J. D. A. Castañón, L. Thévenaz, and M. G. Herráez, “Distributed Brillouin Fiber Sensor Assisted by First-Order Raman Amplification,” J. Lightw. Technol., vol. 28, no. 15, pp. 2162 -2172, August 2010.

[6] S. M. Lopez, M. A. Camas, F. Rodriguez, P. Corredera, J. D. A. Castañón, L. Thévenaz. and M. G. Herráez, “Brillouin optical time-domain analysis assisted by second-order Raman amplification,” Opt. Express, vol. 18, no. 18, pp. 18769-18778, August 2010.

[7] Y. Dong, L. Chen, and X. Bao, “Time-division multiplexing-based BOTDA over 100 km sensing length,” Opt. Lett., vol. 36, no. 2, pp. 277-279, January 2011.

[8] R. Bernini, A. Minardo, and L. Zeni, “Stimulated Brillouin scattering frequency-domain analysis in a single-mode optical fiber for distributed sensing,” Opt. Lett., vol. 29, no. 17, pp. 331-333, September 2004.

[9] A. Minardo, R. Bernini, and L. Zeni, “Brillouin Optical Frequency-Domain Single-Ended Distributed Fiber Sensor,” IEEE Sens. J., vol. 9, no. 3, pp. 221-222, March 2009.

[10] K. Hotate and M. Tanaka, “Distributed fiber Brillouin strain sensing with 1-cm spatial resolution by correlation-based continuous-wave technique” IEEE Photon. Technol. Lett., vol. 14, no. 2, pp. 179-181, February 2002.

[11] M. Belal, and T. P. Newson, “Enhanced Performance of a Temperature-Compensated Submeter Spatial Resolution Distributed Strain Sensor,” IEEE Photon. Technol. Lett., vol. 22, no. 23, pp. 1705-1707, December 2010.

[12] Z. Fang, K. K. Chin, R. Qu, and H. Cai, *Fundamentals of Optical Fiber Sensors*, WILEY, 2012.

[13] K. Kishida, C. H. Li, and K. Nishiguchi, “Pre-pump method for cm-order spatial resolution of BOTDA,” Proceeding of SPIE 2005; 5855: 559-562.

[14] S. B. Cho, and J. J. Lee, “Strain event detection using a double-pulse technique of a Brillouin scattering-based distributed optical fiber sensor,” Opt. Express, vol. 12, pp. 4339-4346, 2004.

[15] A. W. Brown, B. G. Clopitts, and K. Brown, “Dark-pulse Brillouin optical time-domain sensor with 20-mm spatial resolution,” J. Lightw. Technol., vol. 25, pp. 381 -386, 2007.

[16] M. A. Soto, G. Bolognini, and F. D. Pasquale, “Analysis of pulse modulation format in coded BOTDA sensors,” Opt. Express, vol. 18, pp. 14878-14892, 2010.

[17] Q. Yu, X. Bao, F. Ravet, and L. Chen, “Simple method to identify the spatial location better than the pulse length with high strain accuracy,” Opt. Lett., vol. 30, pp. 2215-2217, 2005.

[18] W. Li, X. Bao, Y. Li, and L. Chen, “Differential pulse-width pair BOTDA for high spatial resolution sensing,” Opt. Express, vol. 16, pp. 21616-21625, 2008.

[19] Y. Dong, X. Bao, and W. Li, “Differential Brillouin gain for improving the temperature accuracy and spatial resolution in a long-distance distributed fiber sensor,” Appl. Opt., vol. 48, pp. 4279-4301, 2009.

[20] Y. Li, X. Bao, Y. Dong, and L. Chen, “A novel distributed Brillouin sensor based on optical differenential parametric amplification,” J. Lightw. Technol., vol. 28, pp. 2621-2626, 2010.

[21] X. Bao, and L. Chen, “Recent progress in optical fiber sensors based on Brillouin scattering at University of Ottawa,” Photonic Sensors, vol. 1, pp. 102-117, 2011.

[22] M. N. Alahbabi, Y. T. Cho, and T. P. Newson, “Long-range distributed temperature and strain optical fiber sensor based on the coherent detection of spontaneous Brillouin scattering with in-line Raman amplification,” Measuremetn Science and Technology, vol. 17, pp. 1082-1090, 2006.

[23] M. G. Herraez, L. Thevenaz, and P. Robert, “Distributed measurement of chromatic dispersion by four-wave mixing and Brillouin optical-time-domain analysis,” Opt. Lett., vol. 28, pp. 2210-2212, 2003.

[24] M. O. Vandeventer, and A. J. Boot, “Polarization properties of stimulated Brillouin scattering in single-mode fibers,” J. Lightw. Technol., vol. 12, pp. 585-590, 1994.

[25] L. Thevenaz, “Brillouin distributed time-domain sensing in optical fibers: state of the art and perspectives,” Front. Optoelectron. China, vol. 3(1), pp. 13-21, 2010.

[26] L. Thévenaz, K. Y. Song, M. G. Herráez, “Time biasing due to the slow-light effect in distributed fiber-optic Brillouin sensors,” Opt. Lett. , vol. 31, no. 6, pp. 715-717, March 2006.

[27] R. Bernini, A. Minardo, and L. Zeni, “Dynamic strain measurement in optical fibers by stimulated Brillouin scattering,” Opt. Lett., vol. 34, no.17, pp. 2613-2615, September 2009.

[28] A. Cheng, M. P. Fok, and C. Shu, “Wavelength-transparent, stimulated-Brillouin-scattering slow light using cross-gain-modulation-based wavelength converter and Brillouin fiber laser,” Opt. Lett., vol. 33, no. 22, pp. 2596-2598, November 2008.

[29] A. Zadok, S. Chin, L. Thévenaz, E. Zilka, A. Eyal, and M. Tur, “Polarization-induced distortion in stimulated Brillouin scattering slow-light systems,” Opt. Lett., vol. 34, no. 16, pp. 2530-2532, August 2009.

[30] L. Wang and C. Shu, “Demonstration of distributed strain sensing with the use of stimulated Brillouin scattering-based slow light,” IEEE Photon. J., vol. 3, no. 6, pp. 1164-1170, December 2011.

[31] M. Nikles, L. Thévenaz, and P. A. Robert, “Simple distributed fiber sensor based on Brillouin gain spectrum analysis,” Opt. Lett., vol. 21, no. 10, pp. 758-760, August 1996.

[32] G. P. Agrawal, *Nonlinear Fiber Optics*, fourth ed., Elsevier Pte Ltd., Singapore, 2009.

[33] L. Wang, B. Zhou, C. Shu, and S. He, “Stimulated Brillouin scattering slow-light-based fiber-optic temperature sensor, ” Opt. Lett., vol. 36, no. 3, pp. 427-429, February 2011.

[34] M. Alahbabi, Y. T. Cho, and T. P. Newson, “Comparison of the methods for discriminating temperature and strain in spontaneous Brillouin-based distributed sensors, ” Opt. Lett., vol. 29, no. 1, pp. 26-28, January 2004.

6 DYNAMIC CONTROL OF PHASE MATCHING IN FWM WAVELENGTH CONVERSION BY GAIN-TRANSPARENT SBS

All-optical wavelength conversion (AOWC) is considered as a key functionality in future wavelength division multiplexing (WDM) networks and switching architectures [1]. It offers a way of simultaneously converting a single data channel into different channels without the necessity of multiple optical-electronic-optical (O-E-O) conversions [2]. Several approaches for AOWC have been proposed, including self-phase modulation (SPM) [3], cross-phase modulation (XPM) [4], and cross-gain modulation (XGM) [5]. However, these techniques are only applicable to amplitude-modulated signals, not suitable for wavelength conversion of phase-modulated signals. On the other hand, four-wave mixing (FWM) based wavelength converter offers unique advantages in being transparent to modulation formats, bit-rates, and communication protocols [6-8]. Therefore, it is considered as one of the most promising wavelength converters. FWM can be performed in the semiconductor optical amplifier (SOA) or optical fiber. Generally, the AOWC achieved by FWM in optical fibers can have higher speed operation, while the speed of the AOWC in the SOA is very limited because of a long response time of the carriers [9]. Wavelength conversion based on FWM can be accomplished by using either a single-pump configuration [10] or a dual-pump configuration [11].

Although the FWM based wavelength converter has many advantages, it usually suffers from two major obstacles: stringent requirements on the polarization states of the interacting fields and phase matching among the optical components. The two obstacles result in the polarization-dependent performance and limited conversion bandwidth, respectively. In this chapter, we are addressing the two obstacles, especially the latter one. The phase-matching condition of FWM is introduced in Section 6.1. In Section 6.2 an approach of using gain-transparent SBS to control the phase matching of degenerate FWM is proposed and it is applied to degenerate FWM for the enlargement of its conversion bandwidth. The real data wavelength conversion using degenerate FWM under gain-transparent SBS processing is demonstrated in Section 6.3. To further demonstrate the application of the phase matching control scheme, the gain-transparent SBS is applied to non-degenerate FWM for all-optical manipulation of its bandwidth, which is described in Section 6.4. In Section 6.5, a dual orthogonal-pump wavelength converter assisted by gain-transparent SBS is employed to demonstrate simultaneously polarization-insensitive and wideband wavelength conversion. The last section focuses on one specific application of FWM bandwidth enlargement – the extension of the maximum optical delay based on FWM wavelength conversion and group velocity dispersion.

6.1 Phase-matching Condition in FWM

Unlike the SBS process discussed in Chapter 2, where optical fibers play an active role through molecular vibrations or density variations of silica [12], parametric processes involve modulation of a medium parameter, e.g. refractive index, in which optical fibers play a passive role except for mediating the interaction among several optical beams [12]. Four-wave mixing (FWM) is one of the third-order parametric processes in optical fibers. It originates from the nonlinear response of bound electrons of a material to an external electromagnetic field. It requires phase matching among the interacting fields before the process can build up along the fiber. Thus, significant FWM happens only if the phase mismatch nearly vanishes. In a quantum-mechanical view, for a FWM process where two pumps and one signal are involved, as shown in Fig. 6.1, two photons at the pump frequencies (ω_1 and ω_2) are annihilated, while two photons at the signal frequency (ω_s) and idler frequency (ω_i) are created simultaneously. During this parametric interaction, the conservation of both the net energy and momentum is required. The former requirement is referred to as the matching of the frequencies determining the frequency relationships among those fields, and the latter one is the related to phase matching, that is, the matching

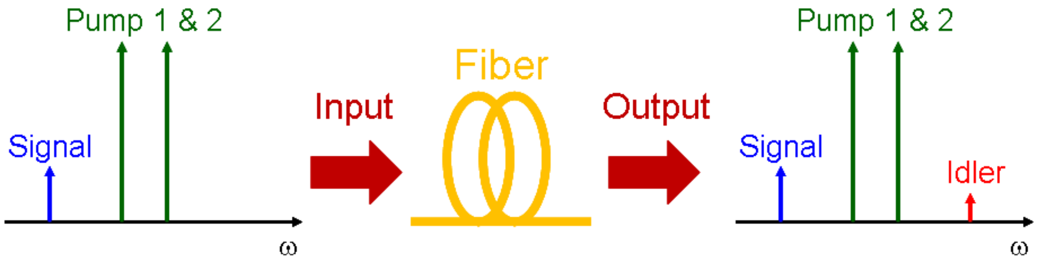

Fig. 6.1 Concept of a general four-wave mixing process.

of the wave vectors. The frequency and phase matching can be mathematically expressed using the following equations:

$$\omega_1 + \omega_2 = \omega_s + \omega_i \tag{6-1}$$

$$\beta_1 + \beta_2 = \beta_s + \beta_i \tag{6-2}$$

where β is the phase constant. A phase mismatch term is usually defined to describe the phase-matching condition:

$$\begin{aligned}\Delta\beta &= \beta_1 + \beta_2 - \beta_s - \beta_i \\ &= (\bar{n}_1\omega_1 + \bar{n}_2\omega_2 - \bar{n}_s\omega_s - \bar{n}_i\omega_i)/c\end{aligned} \tag{6-3}$$

where $\bar{n}$ is the effective mode index. For perfect phase matching, $\Delta\beta$ needs to be zero. Equation (6-3) is only meaningful when other nonlinear effects such as self-phase modulation (SPM) and cross-phase modulation (XPM) are not considered. In practice, those nonlinear effects should be included and hence the effective phase mismatch is given by [12]

$$\kappa = \Delta\beta + \gamma(P_1 + P_2) \tag{6-4}$$

in which γ is the nonlinear coefficient and P_1, P_2 are the powers of the two pumps. The first term denotes the linear phase mismatch, as expressed in Equation (6-3); the second term originates from the effect of SPM of the two pumps. As the powers of the signal and idler are low compared to that of the pump, the SPM and XPM due to the signal and idler are often neglected. The phase mismatch in Equation (6-4) should be zero or close to zero to for FWM to take place efficiently. Since the optical fiber plays a passive role during the FWM process, the phase-matching condition can not be satisfied automatically but requires a specific choice of input wavelengths, powers, and fiber parameters before significant FWM can occur.

In general, the two pumps in Fig. 6.1 have different frequencies ($\omega_1 \neq \omega_2$), which is referred to as non-degenerate FWM. In a special case, where $\omega_1 = \omega_2$, FWM is initiated by a single pump beam. This case is called degenerate FWM, which is also very common in nonlinear fiber optics.

6.2 Conversion Bandwidth Enlargement in Degenerate FWM Using Phase-Matching Control by Gain-Transparent SBS

Although FWM offers advantages in being transparent to the modulation formats, bit-rates, and communication protocols, significant FWM can occur only if the phase velocities of the interplaying waves are matched. The matching condition can hardly be satisfied over a wide spectral range and hence the conversion bandwidth is often limited. To satisfy the phase-matching condition, a specific choice of the input wavelengths and/or special design of fiber parameters are required. Specifically, FWM can be enhanced in the zero-dispersion wavelength region [13] and in a dispersion-flattened fiber [14]. Nonetheless, once the initial parameters (e.g. input wavelengths and powers of the FWM pump and signal, and the nonlinear fiber medium) are chosen, it is difficult to adjust the FWM bandwidth. In this section, we experimentally demonstrate the use of gain-transparent SBS to control purely the phase difference among the fields and thus enlarge the conversion bandwidth dynamically without affecting the input FWM pump or signal powers.

It is worth mentioning that Mateo et al. has previously applied SBS to a FWM pump to control the FWM phase-matching condition [15]. However, in the experiment, both the real and imaginary parts of the SBS gain coefficient were inevitably modified. While the imaginary part influences the phase-matching condition simply through SBS induced refractive index change, the real part complicates the situation by introducing a nonlinear phase term and by increasing the idler power through amplification of the FWM pump. To measure the exact FWM conversion bandwidth, the conversion efficiency (CE) at different signal-pump spectral spacings should be determined under the same initial conditions without affecting the signal and FWM pump powers. Thus, it is crucial that one can have full control of the phase-matching condition and hence the CE without disturbing the initial parameters of the FWM process. The effect was merely examined by simulation in Ref [15] where the real part of the SBS gain has been intentionally removed. Even so, only a negligible improvement of less than 1 dB was predicted in the conversion efficiency. The SBS effect appeared to be insignificant because the simulation study was confined to an operating range within the original 3-dB conversion bandwidth, where the phase velocities of the optical components are already nearly matched.

6.2.1 Principle and Experimental Setup

The SBS process can be described as a nonlinear interaction between the pump and Stokes fields through an acoustic wave [12]. If the frequency of the Stokes wave is within the Brillouin gain bandwidth, it will experience a complex gain given by [16]

$$g_b(\delta) = \frac{g_0}{1 - i\delta} = \frac{g_0}{1 - i\,\dfrac{(\omega_{SBS} - \omega_{stokes} - \Omega_B)}{\Gamma_B / 2}} \tag{6-5}$$

in which g_0 is the peak gain, ω_{SBS} and ω_{stokes} are the frequencies of the SBS pump and Stokes wave, $\Omega_B=2\pi\nu_B$ is the Brillouin frequency shift, Γ_B is the gain bandwidth and $\delta=(\omega_{SBS}-\omega_{stokes}-\Omega_B)/(\Gamma_B/2)$ is the normalized frequency detuning from the Brillouin resonance. The real part of $g_b(\delta)$, $\mathrm{Re}[g_b(\delta)]$, represents a narrowband amplification while the imaginary part $\mathrm{Im}[g_b(\delta)]$ will lead to a sharp change of refractive index and can result in slow or fast light in fibers. The refractive index change is [12]

$$\Delta n = \frac{P_{SBS} \cdot c}{2 A_{eff} \omega_{stokes}} \cdot \mathrm{Im}[g_b(\delta)] \qquad \text{(6-6)}$$

where c is speed of light in vacuum, P_{SBS} is the power of the SBS pump and A_{eff} is the effective area of the fiber. Equation (6-6) determines how SBS can be used to control the phase velocity of an optical carrier.

A general SBS-FWM interaction process where a SBS pump is applied to amplify a FWM pump can be described by the following expression [15, 17]:

$$\frac{dP_{FWM}}{dz} = -\alpha P_{FWM} - 4\gamma (P_s P_i)^{\frac{1}{2}} P_{FWM} \sin\theta + \frac{\mathrm{Re}[g_b(\delta)]}{A_{eff}} P_{SBS} P_{FWM} \qquad \text{(6-7)}$$

$$\frac{dP_{s,i}}{dz} = -\alpha P_{s,i} + 2\gamma (P_s P_i)^{\frac{1}{2}} P_{FWM} \sin\theta \qquad \text{(6-8)}$$

$$\frac{dP_{SBS}}{dz} = \alpha P_{SBS} + \frac{\mathrm{Re}[g_b(\delta)]}{A_{eff}} P_{FWM} P_{SBS} \qquad \text{(6-9)}$$

$$\begin{aligned} \frac{d\theta}{dz} &= \Delta\beta + \gamma(2P_{FWM} - P_s - P_i) + \gamma (P_s P_i)^{\frac{1}{2}} \\ &\quad \times (P_{FWM} / P_s + P_{FWM} / P_i - 4) \cos\theta + \frac{\mathrm{Im}[g_b(\delta)]}{A_{eff}} P_{SBS} \end{aligned} \qquad \text{(6-10)}$$

where P_{FWM} and $P_{s,i}$ are the powers of the FWM pump, signal and idler, α and γ are the loss and nonlinear coefficients, $\Delta\beta \approx \beta_2(\omega_{FWM} - \omega_s)^2$ is the linear phase mismatch with β_2 being the dispersion parameter. $\theta(z) = \Delta\beta z + \phi_s + \phi_i - 2\phi_{FWM}$ is the phase difference in the FWM process and ϕ_{FWM}, ϕ_s, and $\phi_i(z)$ are the nonlinear phase terms. Equation (6-10) describes the evolution of the phase-matching condition. Its last term shows the effect of the SBS induced refractive index change. It should be noted that the real part of the Brillouin gain amplifies the FWM pump and will result in a nonlinear phase term that disturbs the phase-matching condition. As mentioned before, it is preferable that one can dynamically control the phase-matching condition and hence the CE without disturbing the initial parameters of the FWM process.

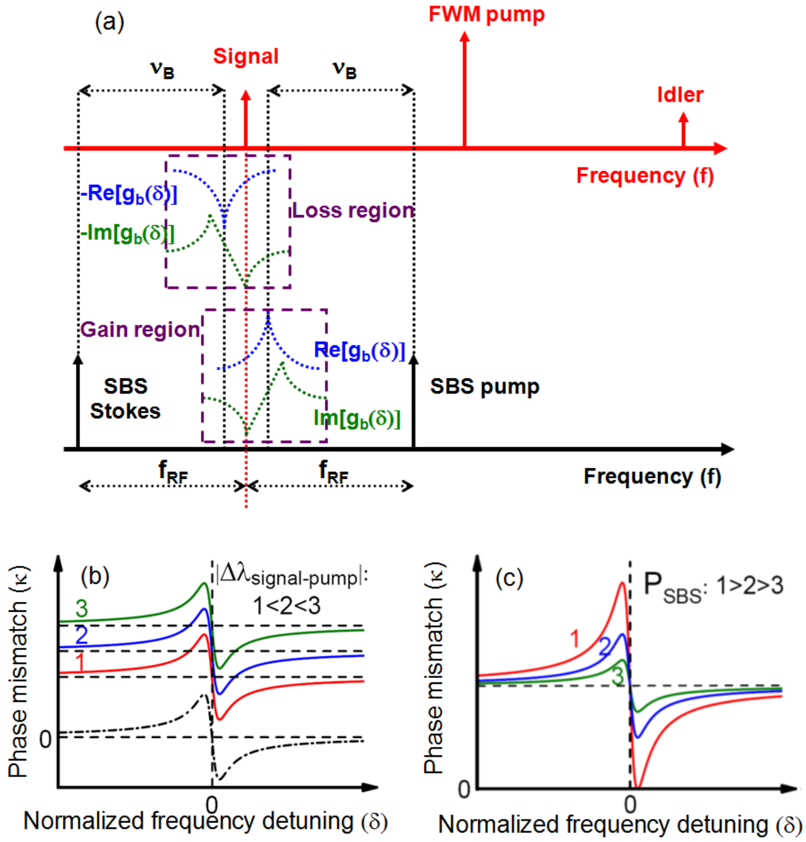

Fig. 6.2 (a) Principle of degenerate FWM bandwidth enlargement using gain-transparent SBS. ν_B : Brillouin frequency shift; f_{RF}: frequency spacing between SBS pump and signal, and between signal and SBS Stokes wave; $g_b(\delta)$: complex Brillouin gain coefficient with δ being the normalized frequency detuning. (b) simulated phase mismatch profiles as a function of δ in the normal dispersion region for different FWM signal-pump spectral spacings and (c) for different power levels of SBS pump and Stokes waves.

The principle of our scheme is illustrated in Fig. 6.2 (a). Here, f_{RF} is the frequency spacing between the SBS pump and the signal, and between the signal and the SBS

Stokes wave. The signal and the FWM pump copropagate in an optical fiber and generate an idler wavelength. At the same time, the SBS pump and Stokes waves are injected into the same fiber from the opposite end. Consequently, optical gain and loss are introduced on the signal by the counter-propagating SBS pump and Stokes waves, respectively. The overall effect is that the amplitude of the signal will remain unaffected. The real parts of SBS gain and loss cancel each other, while the imaginary parts add up to strengthen SBS induced index change. Hence, the last term in Eq. (6-7) disappears while that in Eq. (6-10) is doubled. The total phase mismatch in FWM under gain-transparent SBS can be expressed by the following equation:

$$\kappa = \Delta\beta + 2\gamma\overline{P}_{FWM} - \frac{\mathrm{Im}[g_b(\delta)]}{A_{eff}}\overline{P}_{SBS} \tag{6-11}$$

where $\overline{P}_{FWM}$ and $\overline{P}_{SBS}$ are the average powers of the FWM and SBS pumps, respectively. The first two terms in Equation (6-11) are unchanged once the initial parameters of the FWM process are chosen. The last term represents the SBS induced phase mismatch and can be adjusted by tuning the frequency spacing f_{RF}. To maximize the CE, one can minimize the phase mismatch by optimizing f_{RF} for each signal-pump spectral spacing and hence enlarge the conversion bandwidth without affecting the initial parameters of the FWM process. Fig. 6.2 (b) and (c) show the simulated mismatch curves as a function of δ derived from Eq. (6-11) in the normal dispersion region. In Fig. 6.2 (b), the powers of the SBS pump and Stokes waves are constant. The black dash-dot curve shows the SBS induced phase mismatch. As the FWM signal-pump spectral spacing increases, the mismatch shifts upwards to larger values and thus the CE is reduced. In Fig. 6.2 (c), the signal-pump spectral spacing is fixed. When the powers of the SBS pump and Stokes waves increase, the maximum phase mismatch becomes larger while the minimum phase mismatch becomes smaller, implying that the achievable minimum/maximum CE can be reduced/enhanced.

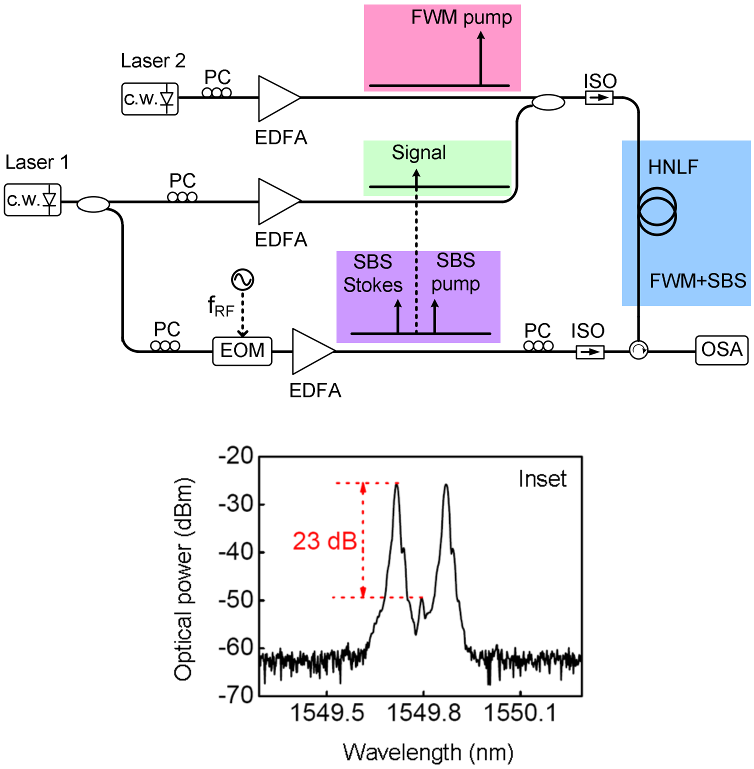

Fig. 6.3 Experimental setup. c.w., continuous wave; EOM, electro-optic intensity modulator; EDFA, erbium-doped fiber amplifier; PC, polarization controller; HNLF, highly nonlinear fiber; ISO, isolator; OSA, optical spectrum analyzer. Inset: spectrum of carrier suppression modulation.

Our experimental setup is shown in Fig. 6.3. The output of laser 1 at 1549.84 nm is split into two branches. The upper branch is amplified by an erbium-doped fiber amplifier (EDFA) to – 6.48 dBm and serves as the signal. The lower branch is modulated by an electro-optic intensity modulator (EOM) biased to suppress the optical carrier and driven at a frequency f_{RF}. The carrier suppression ratio is about 23 dB, as shown in the inset of Fig. 6.3. The two sidebands act as the SBS pump and

Stokes waves after amplification by an EDFA. A FWM pump is provided from another laser 2 and is amplified to 16.48 dBm. The signal together with the FWM pump are directed to a 1 km dispersion-flattened highly nonlinear fiber (HNLF) where FWM takes place in the presence of the counter-propagating SBS pump and Stokes waves. The HNLF has a nonlinear coefficient of 11/(W·km), a dispersion coefficient of –0.4 ps/(nm·km) and a dispersion slope of 5.7×10^{-3} ps/(nm^2·km) at ~1550 nm. It has no zero-dispersion wavelength over the range of 1510 to 1620 nm. The Brillouin frequency shift and gain bandwidth of the HNLF are measured to be 9.698 GHz and 50 MHz, respectively. During the experiment, all the operation wavelengths are in the normal dispersion region.

6.2.2 Results and discussion

The FWM pump wavelength is first fixed at 1546.94 nm corresponding to a signal-pump spectral spacing of ~3 nm. Fig. 6.4 (a)(i) shows the FWM spectrum when the SBS pump and Stokes waves are turned off. By optimizing the polarization state of the FWM pump, a CE of –17.68 dB is obtained. Next, the SBS pump and Stokes waves are turned on with 16 dBm power. A maximum CE of –15.35 dB is achieved at a driving frequency f_{RF} =9.717 GHz while a minimum CE of –30.24 dB is obtained at f_{RF} =9.667 GHz. The two corresponding FWM spectra are depicted in Fig. 6.4 (a)(ii) and (iii), respectively. Comparing Fig. 6.4 (a)(ii) with 6.4 (a)(i), the limited enhancement of 2.33 dB in the CE is explained by the fact that the idler wavelength is within the original 3-dB FWM conversion bandwidth. Thus, the initial FWM process is already nearly phase-matched. It is also shown in Fig. 6.4 (a)(iii) that the matching condition can be totally destroyed by SBS induced phase mismatch. The frequency response of the CE is depicted in Fig. 6.4 (b). Each RF driving frequency results in a different SBS induced phase term, thus allowing precise control of the CE. As the driving frequency is varied, the signal power is monitored with an optical

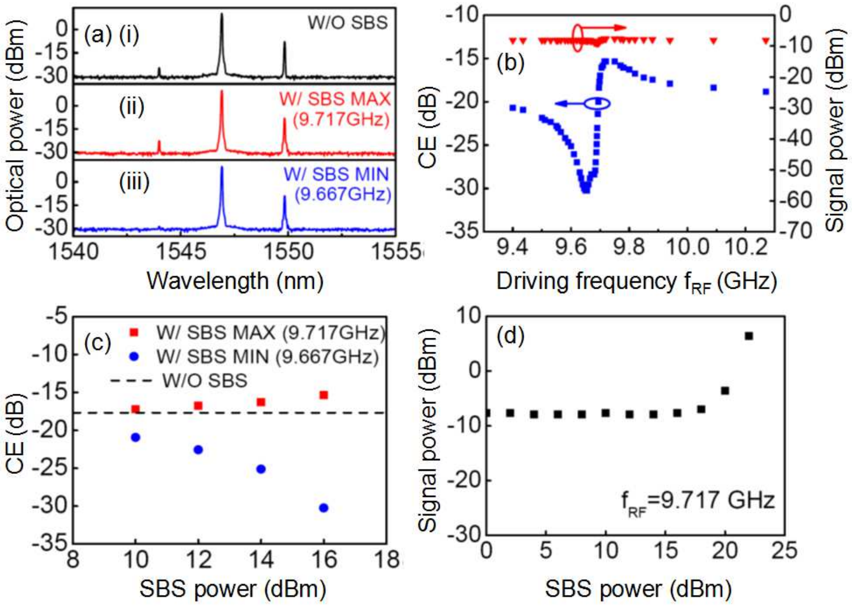

Fig. 6.4 Experimental results of dynamically controlling CE by gain-transparent SBS at a FWM pump wavelength of 1546.94 nm. (a)(i)–(iii) Measured FWM up-conversion spectra without SBS (W/O SBS), with gain-transparent SBS for maximum conversion efficiency (W/ SBS MAX) and with gain-transparent SBS for minimum conversion efficiency (W/ SBS MIN); (b) conversion efficiency and signal power as a function of the RF driving frequency f_{RF}; (c) maximum and minimum conversion efficiency versus the powers of SBS pump and Stokes waves; (d) the signal power versus the powers of SBS pump and Stokes waves.

spectrum analyzer (OSA). The result is also plotted in Fig. 6.4 (b). The power variation is within 1.4 dB, confirming nearly gain-transparent operation. The slight variation may originate from non-perfect Lorentzian lineshape of the Brillouin gain, resulting in non-ideal compensation of SBS gain and loss [18]. To further study the effect of the power of SBS pump and Stokes waves, we measure the CE at different power levels and depict the results in Fig. 6.4 (c). The black dashed line indicates the CE (–17.68 dB) without SBS corresponding to the case in Fig. 6.4 (a)(i). For all the SBS input power levels, the maximum and minimum CE are achieved at f_{RF} =9.717 GHz and f_{RF} =9.667 GHz, respectively. As the SBS power increases, the maximum CE increases from –17.21 to –15.35 dB; while the minimum CE decreases from –20.93 to –30.24 dB. The result is consistent with the prediction illustrated in Fig. 6.2 (c), i.e., at higher power, the minimum phase mismatch becomes smaller while the maximum phase mismatch becomes larger. Due to the aforementioned nearly phase-matched condition at the particular idler wavelength, the enhancement in CE is much weaker than the degradation in CE. We also measure the variation of the signal power versus the power of SBS pump and Stokes waves, as shown in the Fig. 6.4 (d). During the measurement, the driving frequency is fixed at 9.717 GHz. For SBS power ranging from 0 to 16 dBm, the signal power remains nearly constant with a maximum fluctuation of around 0.24 dB. Above 16 dBm, the signal power starts to increase rapidly. The observation can possibly be explained by the saturation of energy transfer from the signal to the SBS Stokes wave. Consequently, SBS loss of the signal is not sufficient to cancel the increasing SBS gain. In order to maintain a constant signal power, we limit the power of the SBS pump and Stokes waves to be 16 dBm in our following experiments.

The FWM pump wavelength is then tuned to 1552.94 nm located at the long wavelength side of the signal. Fig. 6.5 (a)(i) – (iii) show the FWM spectra without SBS, with gain-transparent SBS for maximum CE and minimum CE, respectively. The corresponding CE are –17.68, –14.92 and –29.45 dB. Similar to the case of pump wavelength at 1546.94 nm, limited enhancement of the CE is observed and is explained by initial nearly phase-matched condition of the operating wavelengths. To obtain a large CE enhancement, the FWM pump wavelength is tuned to 1545.94 nm.

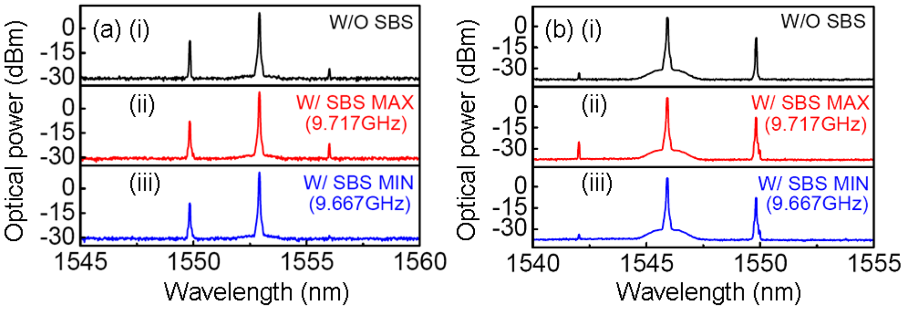

Fig. 6.5 (a) Measured FWM down-conversion spectra when the FWM pump wavelength is 1552.94 nm; (b) measured FWM up-conversion spectra beyond original 3-dB conversion bandwidth when the FWM pump wavelength is 1545.94 nm. (i)–(iii) Spectra without SBS (W/O SBS), with gain-transparent SBS for maximum conversion efficiency (W/ SBS MAX) and with gain-transparent SBS for minimum conversion efficiency (W/ SBS MIN).

The signal-pump spectral spacing is 1 nm larger than that shown in Fig. 6.4. The measured FWM spectra are depicted in Fig. 6.5 (b), where a lower reference level is used in the OSA to clearly show the change in the CE. The measured CE without SBS is –27.12 dB, much lower than that in Fig. 6.4 (a)(i). The reason is the idler wavelength is out of the original 3-dB conversion bandwidth and thus the initial FWM process is far from phase-matched. When the SBS pump and Stokes waves are applied, the CE is enhanced to a maximum value of –17.91 dB at f_{RF} =9.717 GHz. A significant enhancement of 9.3 dB is obtained. Also, the CE can be suppressed to a minimum value of –30.38 dB at f_{RF} =9.667 GHz. The large enhancement of CE implies the feasibility of enlarging the 3-dB FWM conversion bandwidth. Fig. 6.6 shows the result of enlarging the bandwidth. The signal wavelength is fixed at 1549.84 nm while the FWM pump wavelength is tuned. The black squares plot the CE versus the pump wavelength without SBS. The original 3-dB conversion bandwidth is 11.04 nm and is twice that of 5.52 nm in the scale of sweeping the pump wavelength. Next, the SBS pump and Stokes waves are introduced. For each FWM pump wavelength, the driving frequency f_{RF} is tuned to maximize the CE. The result is shown by the red circles in Fig. 6.6. It is clear that the CE enhancement is larger as the operation wavelength is further away from the central region covering the 3-dB conversion bandwidth. Near the central region, the FWM process is phase-matched even without SBS. Away from the region, the matching condition degrades significantly and thus CE enhancement through gain-transparent SBS phase control is of crucial importance. The maximum CE enhancement is 9.3 dB and occurs at a pump wavelength of 1545.94 nm. The 3-dB FWM conversion bandwidth with SBS is increased by 4.58 nm to 15.62 nm, corresponding to 41% enlargement.

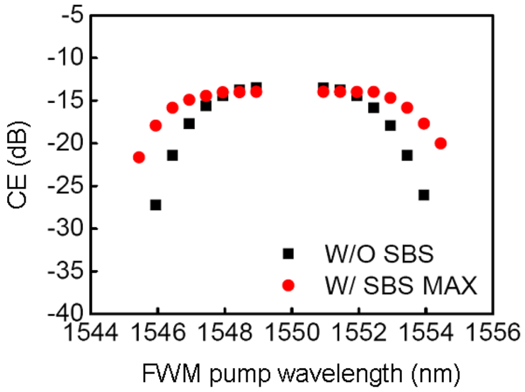

Fig. 6.6 Conversion efficiency versus the FWM pump wavelength without and with gain-transparent SBS in achieving maximum CE.

In applications where the signal may contain high-speed communication data, the SBS gain and loss can be introduced on the FWM pump rather than on the broadband signal. The work is demonstrated in the next section. Note that one may consider to use phase modulator to add phase on the signal rather than to use gain-transparent SBS to control the phase. But there are two disadvantages of using phase modulator. One is that the phase of the signal can only have two values which is not good for continuously tuning the signal phase for phase-matching control. The other one is that phase modulation will broaden the signal spectrum which is not good for wavelength conversion.

6.3 Wavelength Conversion of Communication Signals Using Degenerate FWM with Gain-Transparent SBS for Phase-Matching Control

In Section 6.2, we have experimentally demonstrated the full control of the FWM phase-matching condition entirely through gain-transparent SBS induced refractive index change. The FWM conversion bandwidth was accordingly enlarged by up to 41% from its original value in a dispersion-flattened highly nonlinear fiber (HNLF). The scheme provides an approach to further enlarge the conversion bandwidth after the initial parameters (e.g. input wavelengths and powers of the FWM pump and signal, and the nonlinear fiber medium) of the FWM process are chosen. In this section, we further apply the scheme in dynamic control of degenerate FWM for wavelength conversion of communication signals.

6.3.1 Principle

Fig. 6.7 shows the principle of controlling the optical phase of the degenerate FWM pump using gain-transparent SBS for wavelength conversion of data signals. The principle is similar to that described in Section 6.2 except the optical gain and loss are introduced on the FWM pump rather than on the signal by the counter-propagating SBS pump and Stokes waves. The modification is needed because the frequency bandwidth of high-speed data signal exceeds that of the SBS gain and loss spectra. To understand the dynamic control scheme, it is noted that the total phase mismatch in FWM under gain-transparent SBS can be expressed by the following equation:

$$\kappa = \Delta\beta + 2\gamma\overline{P}_{FWM} \pm 2\left|\frac{\mathrm{Im}[g_b(\delta)]}{A_{eff}}\overline{P}_{SBS}\right| \tag{6-12}$$

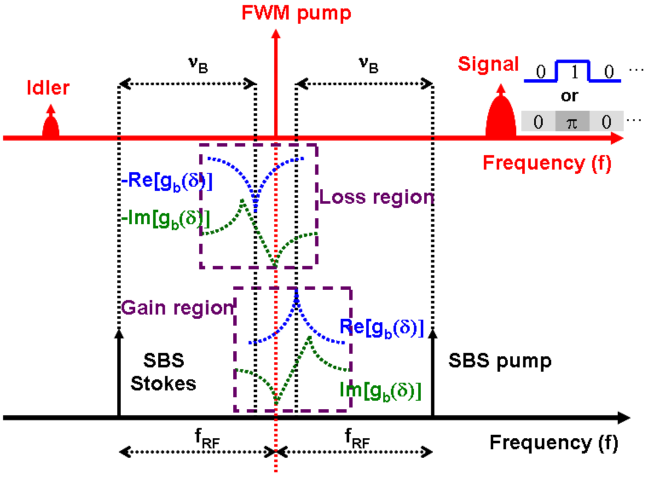

Fig. 6.7. Principle for dynamic control of phase-matching in FWM wavelength conversion of amplitude- and phase- modulated signals using gain-transparent SBS. ν_B: Brillouin frequency shift; f_{RF}: frequency spacing between SBS pump and signal, and between signal and SBS Stokes wave; $g_b(\delta)$: complex Brillouin gain coefficient with δ being the normalized frequency detuning.

where $\overline{P}_{FWM}$ and $\overline{P}_{SBS}$ are the average powers of the FWM and SBS pumps, respectively. Hence, the phase-matching condition can be controlled without affecting the power of the FWM pump. When the scheme is operated at a small signal-pump spectral spacing where the initial FWM process is nearly phase-matched, one can expect a significant reduction in CE by deteriorating the phase-matched condition through gain-transparent SBS. On the other hand, if the signal-pump spacing is large and the initial FWM process is far from phase-matched, a CE enhancement can be obtained by reestablishing the nearly phase-matched condition. The latter case provides a potential application of the dynamic control through gain-

]

transparent SBS: enlargement of the FWM conversion bandwidth without changing the initial FWM parameters.

6.3.2 Wavelength Conversion for Amplitude-Modulated Signals

The experimental setup for dynamic control of FWM wavelength conversion of 10 Gbit/s non-return-to-zero on-off-keying (NRZ–OOK) signal is shown in Fig. 6.8. The output of a tunable laser (TL1) at 1549.8 nm is split into two branches. The upper branch is amplified by an erbium-doped fiber amplifier (EDFA) to 9.9 dBm and serves as the FWM pump. A relatively weak FWM pump is adopted not only to avoid SBS impact by itself, but also to reduce the power requirement of SBS pump and Stokes waves in achieving the gain-transparent operation. The amplified spontaneous emission (ASE) noise from the EDFA is filtered out by a bandpass filter (BPF). The lower branch is modulated by an electro-optic intensity modulator (EOM) biased to suppress the optical carrier and driven at a frequency f_{RF}. The carrier suppression ratio is about 23 dB. The two sidebands act as the SBS pump and Stokes waves after amplification by an EDFA to 15.5 dBm. A 10 Gbit/s NRZ–OOK signal is generated by intensity modulation of another tunable laser 2. The signal is amplified to 5.3 dBm through another EDFA. It is then combined with the FWM pump using a 3 dB coupler. The signal together with the FWM pump are directed to a 1 km HNLF where FWM takes place in the presence of the counter-propagating SBS pump and Stokes waves. The HNLF is the same as that used in Section 6.2. A BPF is used at the port 3 of the circulator to extract the converted idler for detection and measurement.

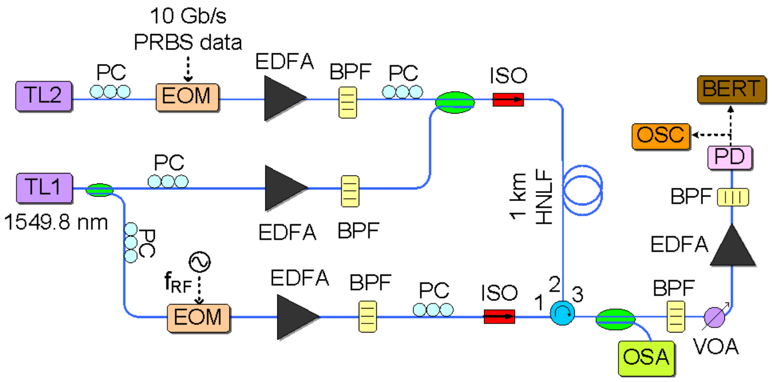

Fig. 6.8. Experimental setup on phase matching control by gain-transparent SBS in FWM wavelength conversion of 10 Gbit/s NRZ–OOK signal. TL: tunable laser; EOM: electro-optic intensity modulator; EDFA: erbium-doped fiber amplifier; PC: polarization controller; BPF: band pass filter; HNLF: highly nonlinear fiber; ISO: isolator; OSA: optical spectrum analyzer; VOA: variable optical attenuator; PD: photodetector; OSC: oscilloscope; BERT: bit error rate tester.

First, the signal wavelength is fixed at 1547.9 nm which corresponds to a signal-pump spectral spacing of 1.9 nm. Fig. 6.9 (a)(i) and (b)(i) show the eye diagram of the converted signal and the corresponding FWM spectrum when the SBS pump and Stokes waves are turned off. With the polarization states optimized, we obtain a CE of –22.1 dB. The noise at the output signal is mainly caused by ASE noise in the EDFA and the noise transferred from four-wave mixing. Owing to degradation in the signal-to-noise ratio, the bit-error rate (BER) performance in Fig. 6.9 (c) shows a power penalty of ~0.8 dB compared to the input signal at the error free detection level ($BER=10^{-9}$). Next, the SBS pump and Stokes waves are turned on. By tuning the driving frequency f_{RF}, we have obtained a maximum CE of –21.9 dB and a minimum CE of –32.8 dB. During the experiment, the FWM pump power variation is smaller than 1.5 dB, confirming nearly gain-transparent operation at different driving frequencies. After the SBS processing, the optical signal-to-noise ratio of the

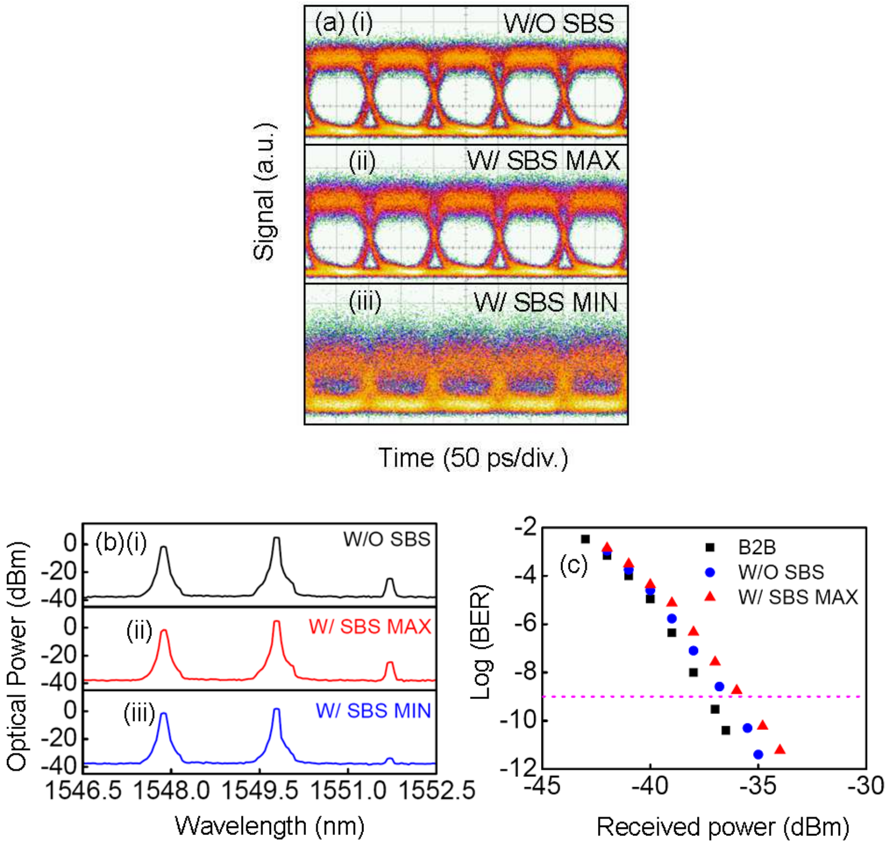

Fig. 6.9. Experimental results on phase matching control by gain-transparent SBS in wavelength up-conversion of 10 Gbit/s NRZ–OOK signal. The signal-pump spectral spacing is 1.9 nm. (a)(i)–(iii) eye diagrams of the converted signal without SBS (W/O SBS), with gain-transparent SBS for maximum CE (W/ SBS MAX) and with gain-transparent SBS for minimum CE (W/ SBS MIN); (b)(i)–(iii) the corresponding FWM spectra; (c) BER measurement for input signal (B2B), converted signals without SBS (W/O SBS) and with gain-transparent SBS for maximum CE (W/ SBS MAX).

FWM pump has a variation within 1.5 dB from its original value of 42 dB. The two corresponding eye diagrams of the converted signals and the FWM spectra are depicted in Fig. 6.9 (a)(ii), (iii) and (b)(ii), (iii), respectively. Comparing Fig. 6.9 (b)(ii) with (b)(i), the limited enhancement of 0.2 dB in the CE is explained by the fact that the idler wavelength is within the original 3-dB FWM conversion bandwidth due to the small signal-pump spectral spacing. Thus, the initial FWM process is already nearly phase-matched. In Fig. 6.9 (b)(iii), it is also verified that the matching condition can be seriously deteriorated by SBS induced phase mismatch, leading to reduction of the CE by up to 10.7 dB when compared to Fig. 6.9 (b)(i). The quality of the converted signal is degraded as shown in Fig. 6.9 (a)(iii). From the BER results in Fig. 6.9 (c), the converted signal with maximum CE reaches error free detection level with a power penalty of ~1.6 dB. The penalty is believed to be caused by SBS processing that introduces additional noise on the converted signal through Rayleigh and Brillouin scattering. It is worth mentioning that the converted idler with minimum CE can only reach lowest BER of ~10^{-2}.

We next tune the signal wavelength to 1546.9 nm corresponding to a signal-pump spectral spacing of 2.9 nm. The results are similar to the case with 1.9 nm signal-pump spectral spacing except that the improvement in the conversion efficiency by SBS phase control is slightly enhanced. The results are summarized in Section 6.3.4.

To obtain a large CE enhancement, the signal wavelength is tuned to 1545.9 nm which gives a signal-pump spectral spacing of 3.9 nm. The measured results are depicted in Fig. 6.10. The CE without SBS is –32.3 dB and is 10.2 dB worse than the case with 1.9 nm signal-pump spacing in Fig. 6.9 (a)(i) and (b)(i). Consequently, a small eye opening is observed for the converted signal as shown in Fig. 6.10 (a)(i). The observation is explained by the fact that for widely separated signal and pump, the FWM process is far from phase-matched. Due to the low CE, the converted signal cannot reach error free detection level and the lowest measured BER is ~10^{-3}.

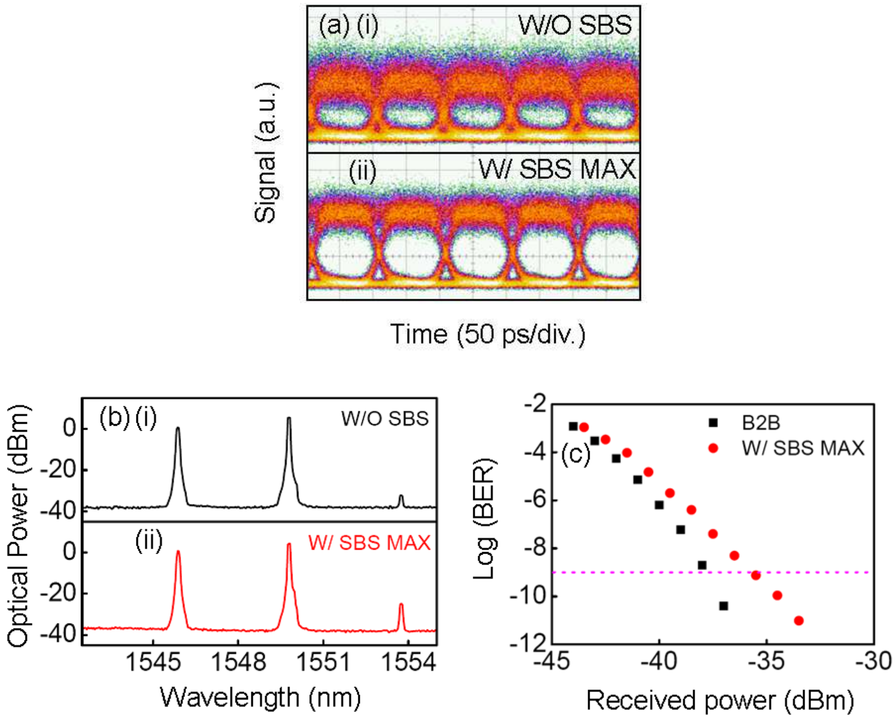

Fig. 6.10. Experimental results on phase matching control by gain-transparent SBS in wavelength up-conversion of 10 Gbit/s NRZ–OOK signal at a signal-pump spectral spacing of 3.9 nm. (a)(i)–(ii) eye diagrams of the converted signal without SBS (W/O SBS) and with gain-transparent SBS for maximum CE (W/ SBS MAX); (b)(i)–(ii) the corresponding FWM spectra; (c) BER measurement for input signal (B2B) and converted signal with gain-transparent SBS for maximum CE (W/ SBS MAX).

When the SBS pump and Stokes waves are applied to the FWM pump, we have achieved a maximum CE of –24.6 dB. A significant CE enhancement of 7.7 dB is obtained due to re-establishment of the nearly phase-matched condition through gain-transparent SBS. The increase in CE gives rise to a widely opened eye of the converted signal (Fig. 6.10 (a)(ii)) and error free detection with a power penalty of ~2.1 dB (Fig. 6.10 (c)). The strong enhancement of the CE is consistent with the enlargement of the 3-dB FWM conversion bandwidth. Here, we do not record the results for the converted signal with gain-transparent SBS for minimum CE, as the quality of the converted signal without SBS is already very poor. Finally we tune the signal wavelength to 1553.9 nm located at the long wavelength side of the FWM pump, with a signal-pump spectral spacing of 4.1 nm. The results are plotted in Fig. 6.11 which are comparable to those in Fig. 6.10. The CE without SBS and with gain-transparent SBS for maximum CE are –33 dB and –24.2 dB, respectively. The enhancement in the CE is 8.8 dB, resulting in large eye opening of the converted signal (Fig. 6.11 (a)(ii)) when compared to that without SBS (Fig. 6.11 (a)(i)). We also observe that the converted signal shown in Fig. 6.11 (a)(ii) can reach error free detection level with BER performance similar to that in Fig. 6.10 (c).

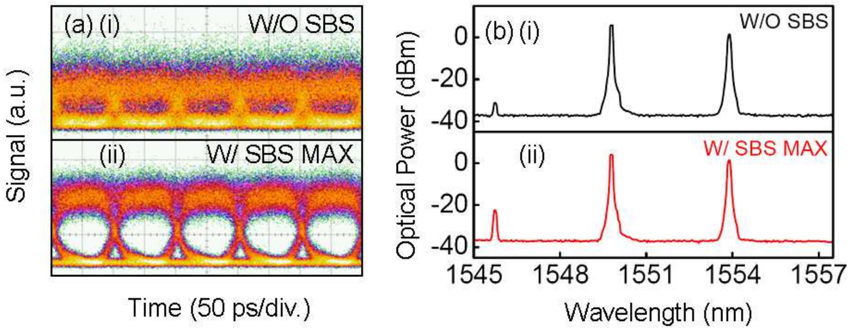

Fig. 6.11. Experimental results on phase matching control by gain-transparent SBS in wavelength down-conversion of 10 Gbit/s NRZ–OOK signal at a signal-pump spectral spacing of 4.1 nm. (a)(i)–(ii) eye diagrams of the converted signal without SBS (W/O SBS) and with gain-transparent SBS for maximum CE (W/ SBS MAX); (b)(i)–(ii) the corresponding FWM spectra.

6.3.3 Wavelength Conversion for Phase-Modulated Signals

In this section, we use 10 Gbit/s NRZ- differential-phase-shift-keying (DPSK) PRBS data as the input signal and perform the wavelength conversion for phase-modulated signals. The setup is shown in Fig. 6.12. It is almost the same as that in Fig. 6.8 except that one of the EOMs is replaced by a phase modulator (PM) for the generation of 10 Gbit/s NRZ–DPSK input signal, and a 100-ps Mach-Zehnder delay interferometer (MZDI) is added before the photodetector to demodulate the converted signal. The powers of the FWM pump, signal and SBS waves are 9.8, 5.7

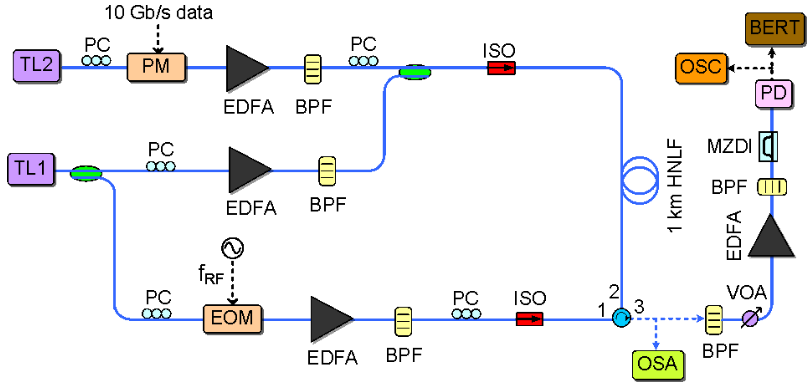

Fig. 6.12. Experimental setup on phase matching control by gain-transparent SBS in FWM wavelength conversion of 10 Gbit/s NRZ–DPSK signal. TL: tunable laser; EOM: electro-optic intensity modulator; PM: phase modulator; EDFA: erbium-doped fiber amplifier; PC: polarization controller; BPF: band pass filter; HNLF: highly nonlinear fiber; ISO: isolator; OSA: optical spectrum analyzer; VOA: variable optical attenuator; MZDI: Mach-Zehnder delay interferometer; PD: photodetector; OSC: oscilloscope; BERT: bit error rate tester.

and 14.4 dBm, respectively. The eye diagrams and optical spectra of the demodulated input NRZ-DPSK signal are shown in Fig. 6.13. Note that during the experiment the wavelength of the input signal is slightly tuned to obtain the largest eye opening for the demodulated signal.

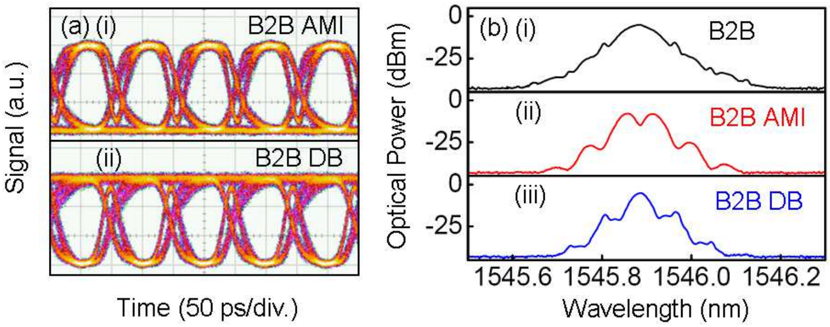

Fig. 6.13. (a) Eye diagrams of the demodulated input NRZ-DPSK signal in (i) alternate mark inversion (AMI) and (ii) duobinary (DB) formats; (b)(i)–(iii) optical spectra of the input NRZ–DPSK, demodulated AMI, and demodulated DB signals. B2B: back to back.

For NRZ–DPSK signal wavelength conversion, we follow the experimental procedure described in Section 6.3.2 and gradually increase the signal-pump spectral spacing. First, the signal wavelength is fixed at 1547.86 nm with a signal-pump spectral spacing of 1.94 nm. Fig. 6.14 (a)(i) and (b)(i) shows the eye diagrams of the converted signal in alternate-mark-inversion (AMI) and duobinary (DB) formats after demodulation, and (c)(i) shows the corresponding FWM spectrum when the SBS pump and Stokes waves are turned off. The measured CE is –21.63 dB after the polarization states are optimized. In the BER measurement, we only measure the demodulated AMI signal for convenience. The BER performance in Fig. 6.14 (d) indicates a power penalty of ~0.5 dB compared to the input signal at the error free detection level. Next, the SBS pump and Stokes waves are turned on. By tuning the

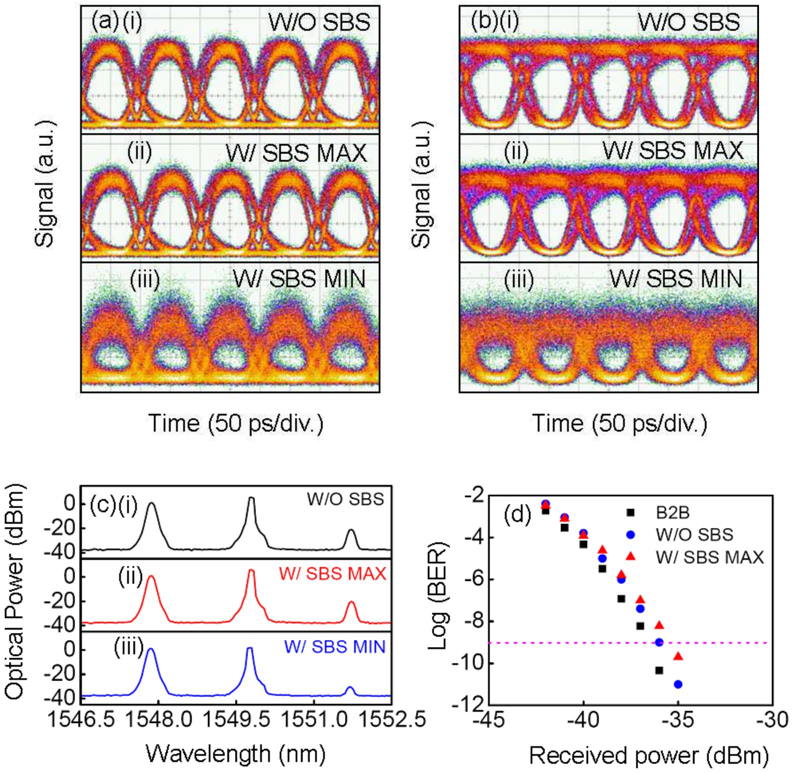

Fig. 6.14. Experimental results on phase matching control by gain-transparent SBS in wavelength up-conversion of 10 Gbit/s NRZ–DPSK signal at a signal-pump spectral spacing of 1.94 nm. (a) and (b): eye diagrams of the converted AMI and DB signals (i) without SBS (W/O SBS), (ii) with gain-transparent SBS for maximum CE (W/ SBS MAX) and (iii) with gain-transparent SBS for minimum CE (W/ SBS MIN); (c)(i)–(iii) the corresponding FWM spectra; (d) BER measurement results for input AMI signal (B2B), converted AMI signals without SBS (W/O SBS) and with gain-transparent SBS for maximum CE (W/ SBS MAX).

driving frequency f_{RF}, we have obtained a maximum CE of –20.7 dB and a minimum CE of –33 dB. During the experiment, the FWM pump power variation is smaller than 1.5 dB. Both limited enhancement (0.93 dB) and large reduction (11.37 dB) of the CE are observed due to the initial nearly phase-matched condition at small signal-pump spectral spacing. The corresponding eye diagrams of the converted AMI and DB signals are depicted in Fig. 6.14 (a)(ii), (iii) and (b) (ii), (iii), and the FWM spectra are shown in Fig. 6.14 (c)(ii), (iii), respectively. Fig. 6.14 (a)(ii), (iii) and (b) (ii), (iii) show that the dynamic control of phase-matching by gain-transparent SBS can be applied to phase-transparent wavelength conversion. From the BER results in Fig. 6.14 (d), the converted AMI signal with maximum CE reaches error free detection level with a power penalty of ~1.2 dB. Instead, the converted idler with minimum CE can only reach lowest BER of $\sim 10^{-6}$.

We next reduce the signal-pump spectral spacing to 2.94 nm with the signal wavelength fixed at 1546.86 nm. Similar results are obtained except that the improvement in conversion efficiency by SBS phase control is again slightly enhanced. The results are summarized in Section 6.3.4. Subsequently, the signal wavelength is tuned to 1545.89 nm corresponding to a signal-pump spectral spacing of 3.91 nm, which is large enough to observe a significant CE enhancement. The measured results are depicted in Fig. 6.15. At this large signal-pump spectral spacing, the FWM process is far from phase-matched. The CE without SBS is –32 dB which is 10.37 dB worse than the case in Fig. 6.14. Therefore, a small eye opening is observed for both the converted AMI and DB signals as shown in Fig. 6.15 (a)(i) and (b)(i). The lowest BER obtained for the converted AMI signal is $\sim 10^{-8}$. When the SBS pump and Stokes waves are applied to the FWM pump, the achieved maximum CE and minimum CE are –24.88 dB and –34.12 dB, respectively. A significant CE enhancement of 7.12 dB is obtained. The increase in CE gives rise to a widely opened eye of the converted AMI and DB signals (Fig. 6.15 (a)(ii) and (b)(ii)) and error free detection of the converted AMI signal with a power penalty of ~2.9 dB

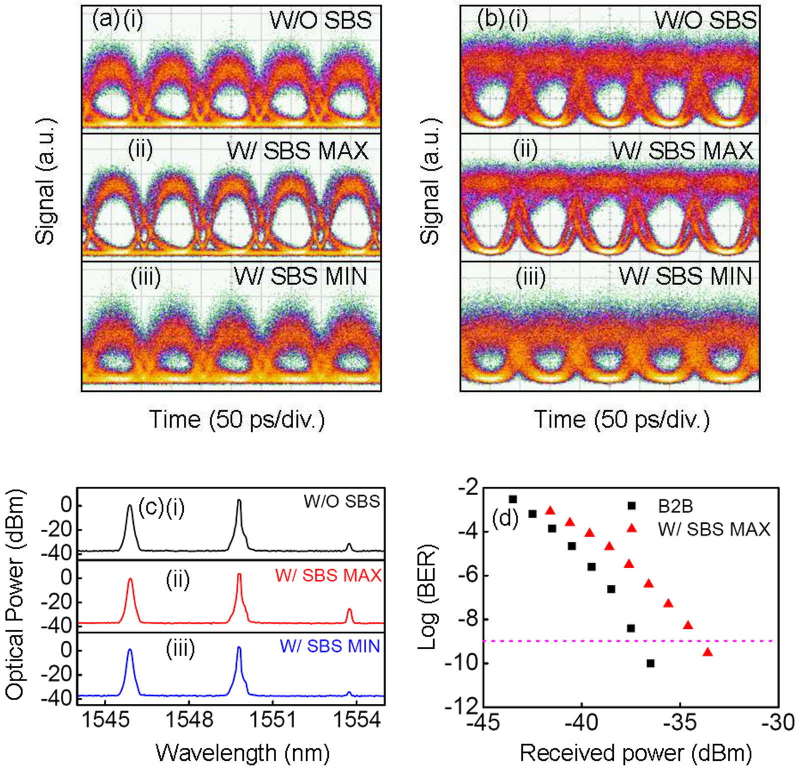

Fig. 6.15. Experimental results on phase matching control by gain-transparent SBS in wavelength up-conversion of 10 Gbit/s NRZ–DPSK signal at a signal-pump spectral spacing of 3.91 nm. (a) and (b): eye diagrams of the converted AMI and DB signals (i) without SBS (W/O SBS), (ii) with gain-transparent SBS for maximum CE (W/ SBS MAX) and (iii) with gain-transparent SBS for minimum CE (W/ SBS MIN); (c)(i)–(iii) the corresponding FWM spectra; (d) BER measurement results for input AMI signal (B2B) and converted AMI signal with gain-transparent SBS for maximum CE (W/ SBS MAX).

(Fig. 6.15 (d)). On the other hand, the narrow eye opening of the converted AMI signal with gain-transparent SBS for minimum CE in Fig. 6.15 (a)(iii) results in lowest measured BER of ~10^{-5}. Finally we also perform the experiment for wavelength down-conversion. The signal wavelength is tuned to 1553.87 nm located

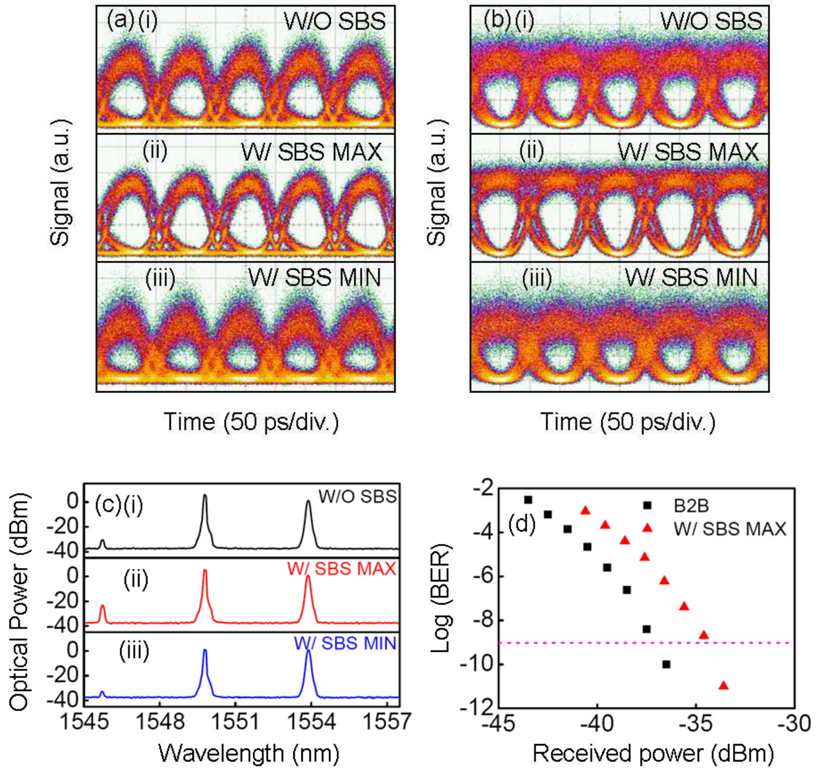

Fig. 6.16. Experimental results on phase matching control by gain-transparent SBS in wavelength down-conversion of 10 Gbit/s NRZ–DPSK signal at a signal-pump spectral spacing of 4.07 nm. (a) and (b): eye diagrams of the converted AMI and DB signals (i) without SBS (W/O SBS), (ii) with gain-transparent SBS for maximum CE (W/ SBS MAX) and (iii) with gain-transparent SBS for minimum CE (W/ SBS MIN); (c)(i)–(iii) the corresponding FWM spectra; (d) BER measurement results for input AMI signal (B2B) and converted AMI signal with gain-transparent SBS for maximum CE (W/ SBS MAX).

at the long wavelength side of the FWM pump. The signal-pump spectral spacing is 4.07 nm. The results are plotted in Fig. 6.16. The CE without SBS is –31.63 dB, while the maximum and minimum CE under gain-transparent SBS are –24.19 dB and –33.72 dB, respectively. Due to re-establishment of the nearly phase-matched condition by gain-transparent SBS, the CE is enhanced by 7.44 dB. Hence, widely opened eyes are obtained for the converted AMI and DB signals (Fig. 6.16 (a)(ii) and (b)(ii)) compared to those without SBS (Fig. 6.16 (a)(i) and (b)(i)). The BER measurement of the converted AMI signal with gain-transparent SBS for maximum CE shows a power penalty of ~2.6 dB at error free detection level, as depicted in Fig. 6.16 (d). In comparison, the lowest BERs for the converted AMI signal without SBS is $\sim 8\times10^{-9}$ and with gain-transparent SBS for minimum CE is $\sim 10^{-6}$.

6.3.4 Discussion

Once the initial parameters (e.g. input wavelengths and powers of the FWM pump and signal, and the nonlinear fiber medium) of the FWM process are chosen, the CE is usually fixed. Our scheme offers a solution for dynamic control of phase-matching by gain-transparent SBS. The CE can be significantly enhanced without disturbing the initial parameters, thus providing an approach to enlarge the conversion bandwidth. For convenience of discussion, Table 6.1 and 6.2 summarize the results of FWM wavelength conversion of NRZ-OOK and NRZ-DPSK signals at four signal-pump spectral spacings. From the results in the Tables, it is clear that the CE enhancement is more pronounced as the signal-pump spectral spacing increases. Within the original 3-dB conversion bandwidth, the FWM process is nearly phase-matched even without SBS. While away from this region, the phase matching condition degrades significantly and thus CE enhancement through gain-transparent SBS phase control is of crucial importance to enlarge the conversion bandwidth. However, the bandwidth cannot be enlarged indefinitely. The enlargement is limited by the maximum SBS induced phase mismatch that one can achieve in the experiment. The SBS induced phase mismatch described in Equation (6-12) is Im[$g_b(\delta)$] $\overline{P}_{SBS} / A_{eff} = g_0 P_{SBS}\delta / [A_{eff}(1+\delta^2)]$, which takes a value over the range of $-0.5g_0\ \overline{P}_{SBS} / A_{eff}$ to $0.5g_0\ \overline{P}_{SBS} / A_{eff}$ governed by the RF frequency f_{RF}. The maximum value $0.5g_0\ \overline{P}_{SBS} / A_{eff}$ of the SBS induced phase mismatch should be sufficiently large to compensate the linear and nonlinear phase mismatch ($\Delta\beta$ and $2\gamma\,\overline{P}_{FWM}$ in Equation (6-12)) over a wide operation band. To achieve this purpose, one approach is to enhance the Brillouin gain coefficient by adopting special nonlinear fiber [19] but it relies on complicated fiber design and manufacture. The other approach is to simply increase the power $\overline{P}_{SBS}$. If there is no restriction on the power limit, one can obtain very large SBS induced phase mismatch to compensate

Table 6.1: Experimental results for FWM wavelength conversion of NRZ-OOK signal

$\lambda_p - \lambda_s$ (nm)	CE (dB), Power Penalty (dB) or Lowest BER		
	W/O SBS	W/ SBS MAX	W/ SBS MIN
1.9	–22.1, 0.8	–21.9, 1.6	–32.8, 10^{-2} (BER)
2.9	–26.3, 1.3	–24.2, 2.7	–34.9, 10^{-2} (BER)
3.9	–32.3, 10^{-3} (BER)	–24.6, 2.1	
–4.1	–33	–24.2	

Table 6.2: Experimental results for FWM wavelength conversion of NRZ-DPSK signal

$\lambda_p - \lambda_s$ (nm)	CE (dB), Power Penalty (dB) or Lowest BER		
	W/O SBS	W/ SBS MAX	W/ SBS MIN
1.9	–21.6, 0.5	–20.7, 1.2	–33, 10^{-6} (BER)
2.9	–25.4, 1.2	–22.3, 2.4	–33, 10^{-6} (BER)
3.9	–32, 10^{-8} (BER)	–24.9, 2.9	–34.1, 10^{-5} (BER)
–4.1	–31.6, 8×10^{-9} (BER)	–24.2, 2.6	–33.7, 10^{-6} (BER)

the phase mismatch over a very wide bandwidth. However, in practice the SBS loss is not sufficient in cancelling the increasing SBS gain at high pumping power due to saturation of the energy transfer, hence destroying the gain-transparent operation. On the other hand, higher-order SBS processes will also be introduced at high pumping intensity, resulting in undesirable light waves generated at frequencies in the vicinity of the signal. This results in in-band noise on the converted signal. Both these factors limit the increase of the power $\overline{P}_{SBS}$ and hence the enlargement of the conversion bandwidth. Under our experimental conditions, the 3-dB conversion bandwidth can be enlarged by 41% to cover a signal-pump spectral spacing up to ~ 4 nm. In practical applications, the amount of linear and nonlinear phase mismatch and the attainable maximum SBS induced phase mismatch should be carefully and comprehensively taken into account.

At a large signal-pump spectral spacing, the converted signal without SBS has a poor quality. Using gain-transparent SBS to maximize the CE, the converted signal can reach error-free detection level. However, the SBS process also introduces additional noise on the converted signal, resulting in extra power penalty in the BER performances. In NRZ–OOK signal wavelength conversion, Table 6.1 shows the extra power penalties are ~0.8 and ~1.4 dB at signal-pump spectral spacings of 1.9 and 2.9 nm, respectively. While in NRZ–DPSK signal wavelength conversion, Table 6.2 indicates extra power penalties of ~0.7 and ~1.2 dB at signal-pump spectral spacings of 1.94 and 2.94 nm, respectively. The noise on the converted signal originates from different sources including the ASE noise in the EDFA, the noise transferred from the pump in the FWM process, and the noise through Rayleigh and Brillouin scattering. One can employ a bandpass filter to remove most of the noise.

However, to reduce the noise from SBS processing, one may need to decrease the power $\overline{P}_{SBS}$. Unfortunately, excessive reduction of the power may lead to insufficient SBS induced phase mismatch to compensate the linear and nonlinear phase mismatch. Hence, there is a trade-off between the amount of noise and the magnitude of SBS induced phase mismatch. A good strategy is to limit the SBS pump power to a level that is just enough to minimize the total phase mismatch.

It is worth mentioning that the dynamic control of phase-matching in FWM wavelength conversion is demonstrated under single channel operation. For multi-channel conversion, it is difficult to achieve maximum CE simultaneously for all the channels as the required optimal SBS induced phase mismatch are different for different signal-pump spacings. A compromise can be made in optimization by targeting for the maximum number of error-free detection channels. The exact choice of induced phase mismatch may also depend on other system requirements.

Apart from the application in enlarging the FWM conversion bandwidth, the dynamic phase-matching control scheme by gain-transparent SBS can also be applied to other areas, such as fiber-based optical parametric amplifier (FOPA) [20, 21] and phase-sensitive amplification (PSA) [22], where the phase matching condition is not automatically satisfied. We consider the case of a FOPA. Single-pumped FOPA is attractive due to its simple configuration and high gain. A limitation is that single pump cannot provide a flat gain for broadband operation owing to phase mismatch. There are proposals to achieve quasi-phase-matching (QPM) by periodic insertions of standard single mode fibers [17] or fiber Bragg gratings (FBG) [20] to flatten the parametric gain. However, the approaches offer no operational flexibility and the gain profile of the FOPA is fixed. Instead, if the dynamic phase-matching control scheme is applied to the FOPA, one can obtain a flexible parametric gain profile by simply tuning the RF frequency f_{RF}. The optimal gain profile can be obtained according to the practical environment. The demonstration of this flexible gain profile will be discussed in detail in Chapter 7.

6.4 All-Optical Manipulation of Non-Degenerate FWM Conversion Bandwidth by Gain-Transparent SBS

In degenerate FWM-based wavelength conversion where the wavelength is converted symmetrically with respect to the pump wave, the availability of the wavelength for the newly converted idler is restricted by the strict phase-matching condition of FWM, especially at a large signal-pump spectral spacing. As a result, broadband wavelength conversion is not possible unless extra efforts are made, e.g. specific choice of the input wavelength [13] and special design of fiber parameters [14]. On the other hand, dual-pump or non-degenerate FWM process provides a way of achieving broadband wavelength conversion since the phase-matching condition in a non-degenerate FWM process can be maintained over a wide spectral range [23, 24]. Besides the wide wavelength tuning range of the converted idler, polarization-insensitive wavelength conversion has also been demonstrated using non-degenerate FWM [25]. Therefore, non-degenerate FWM possesses unique advantages over degenerate FWM.

Although non-degenerate FWM has wider conversion bandwidth than that of degenerate FWM, its phase-matching condition is still difficult to be satisfied when the operation range is beyond certain values. Thus, it is helpful to develop methods to enhance the phase-matching condition at larger spectral range in further enlarging the conversion bandwidth. In this section, we apply the gain-transparent SBS technique to non-degenerate FWM, and investigate its performance on the manipulation of the conversion bandwidth and effectiveness in the wavelength conversion of data signals.

6.4.1 Principle and Experimental Setup

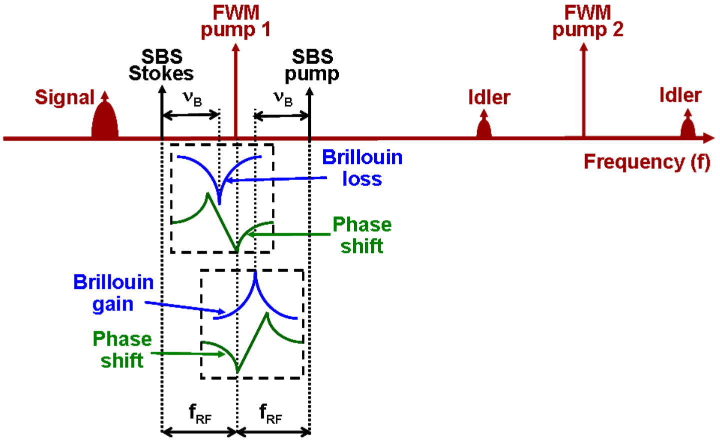

Fig. 6.17. Principle for all-optical manipulation of non-degenerate FWM conversion bandwidth using gain-transparent SBS. ν_B *: Brillouin frequency shift;* f_{RF}*: frequency spacing between SBS pump and signal, and between signal and SBS Stokes wave.*

The principle of all-optical manipulation of non-degenerate FWM conversion bandwidth using gain-transparent SBS is shown in Fig. 6.17. In our non-degenerate FWM, the signal and the FWM pumps co-propagate in an optical fiber, two idlers are generated through scattering of the FWM pump 2 by the index grating originated from the beating of FWM pump 1 and the signal. The phase control principle is the same as that described in Section 6.2. Here, both the optical gain and loss are introduced on the FWM pump 1 by the counter-propagating SBS pump and Stokes waves, respectively.

Our experimental setup is shown in Fig. 6.18. The output of a tunable laser (TL1) at 1549.8 nm is split into two branches. The upper branch is amplified by an EDFA to 9 dBm and serves as the FWM pump 1. The lower branch is modulated by an EOM biased to suppress the optical carrier and driven at a frequency f_{RF}. The carrier suppression ratio is about 23 dB. The two sidebands act as the SBS pump and Stokes

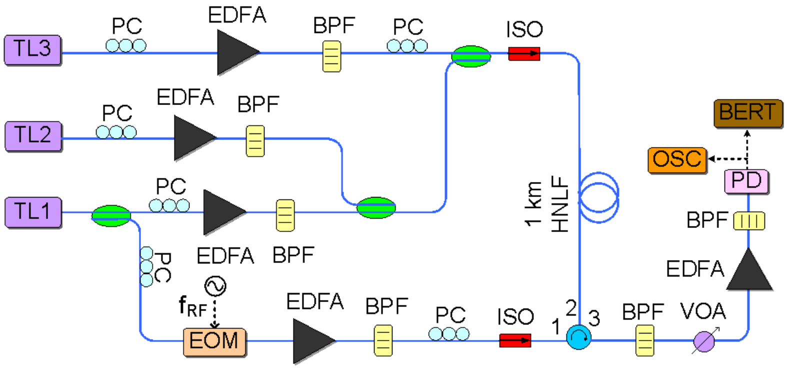

Fig. 6.18. Experimental setup. TL: tunable laser; EOM: electro-optic intensity modulator; EDFA: erbium-doped fiber amplifier; PC: polarization controller; BPF: band pass filter; HNLF: highly nonlinear fiber; ISO: isolator; OSA: optical spectrum analyzer; VOA: variable optical attenuator; PD: photodetector; OSC: oscilloscope; BERT: bit error rate tester.

waves after amplification by an EDFA to 15 dBm. FWM pump 2 is provided by a tunable laser 2 (TL2) and is boosted to a power of 8.9 dBm by an EDFA. Another tunable laser 3 (TL3) at 1550.8 nm generates the signal and it is amplified to 5.6 dBm. The signal together with the FWM pumps are directed to a 1 km dispersion-flattened HNLF where non-degenerate FWM takes place in the presence of the counter-propagating SBS pump and Stokes waves. The HNLF is the same as that used in Section 6.2. A BPF is used at the port 3 of the circulator to extract the converted idler for detection and measurement.

6.4.2 Results and Discussion

First, we tune the FWM pump 2 wavelength to be 1553.9 and 1564.9 nm as two examples showing the impact of the gain-transparent SBS on the phase-matching control of non-degenerate FWM. The corresponding FWM spectra are shown in Fig. 6.19. Here, since the two idlers have the same qualities, we only measure the idler at shorter wavelength side of FWM pump 2. When the SBS pump and Stokes waves are turned off, the signal is co-polarized with FWM pump 1 to make the index grating strongest and the polarization state of the FWM pump 2 is optimized to obtain the

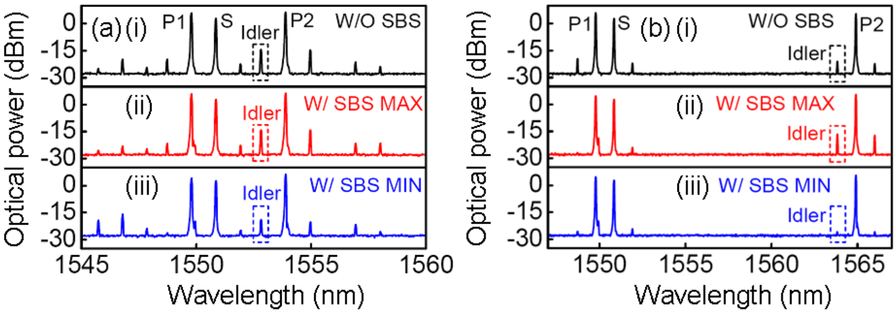

Fig. 6.19 (a) Measured FWM spectra when the FWM pump 2 wavelength is 1553.9 nm; (b) 1564.9 nm. (i)–(iii) Spectra without SBS (W/O SBS), with gain-transparent SBS for maximum CE (W/ SBS MAX) and with gain-transparent SBS for minimum CE (W/ SBS MIN).

Table 6.3: CE with and without SBS phase control for two different wavelength of FWM pump 2

FWM pump 2 wavelength (nm)	CE (dB)		
	W/O SBS	W/ SBS MAX	W/ SBS MIN
1553.9	-17	-16.7	-22.3
1564.9	-24	-19.3	-28.8

highest CE. After the gain-transparent SBS is applied, the CE is maximized or minimized by tuning the driving frequency f_{RF}. During the experiment, the measured power variation of the FWM pump 1 is within 1.3 dB. The CE values without SBS (W/O SBS), with gain-transparent SBS for maximum CE (W/ SBS MAX) and with gain-transparent SBS for minimum CE (W/ SBS MIN) are summarized in Table 6.3. The CE is enhanced through minimizing the phase mismatch while it is reduced by maximizing the phase mismatch.

Next, the wavelength of FWM pump 2 is tuned from 1538 to 1566 nm. The dark squares in Fig. 6.20 plot the CE versus the pump 2 wavelength without SBS. The 3-dB conversion bandwidth is 18 nm. Next, the SBS pump and Stokes waves are introduced. The driving frequency f_{RF} is adjusted correspondingly for each FWM pump 2 wavelength to obtain both the maximum and the minimum CE. The measured CE under gain-transparent SBS are depicted as red dots and blue triangles in Fig. 6.20. The effect of the gain-transparent SBS on dynamic manipulation of the conversion bandwidth is obvious: the 3-dB conversion bandwidth is enlarged to 26 nm (44% increase) in the case of maximum CE while it is reduced to 15 nm in the case of minimum CE. More importantly, the value of the CE for each FWM pump 2 wavelength can be adjusted between the maximum and minimum CE through tuning the driving frequency f_{RF}, that is to say one can synthesize any shape of the CE profile between the maximum and minimum CE without affecting the initial parameters of the non-degenerate FWM, e.g. a very flat CE profile over the FWM pump 2 tuning range which shows larger conversion bandwidth. This is usually important for broadband wavelength conversion that all the converted idlers at a wide wavelength range can have the same performance.

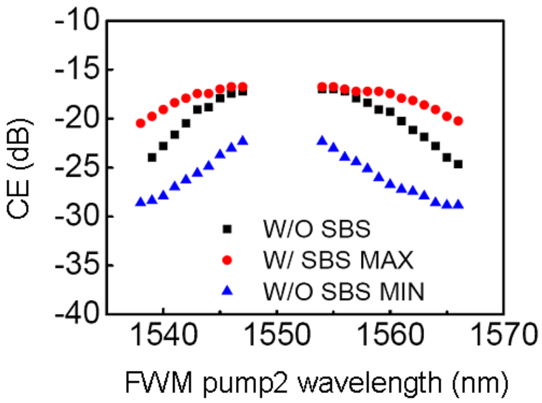

Fig. 6.20 Conversion efficiency versus the FWM pump 2 wavelength without and with gain-transparent SBS in achieving the maximum and minimum CE.

To investigate the performance on the manipulation of FWM bandwidth for wavelength conversion of a data signal, the output of tunable laser 3 in Fig. 6.18 is intensity modulated to generate 10 Gbit/s NRZ-OOK signal. The power of the signal is 6.9 dBm. As an example, the FWM pump 2 wavelength is fixed at 1564.9 nm. Fig. 6.21 (a) shows the measured eye diagrams of the input signal, and converted idlers without SBS, with gain-transparent SBS for maximum and minimum CEs. Optical signal-to-noise ratio (OSNR) is also measured to estimate the signal quality, which are 16.3, 8.3, 10.6 and 4.4 dB from Fig. 6.21 (a)(i) to (iv). Apparently the idler in Fig. 6.21 (a)(iv) has the worst quality due to the low CE. The corresponding FWM spectra are plotted in Fig. 6.21 (b). The CE is successfully controlled by the gain-transparent SBS, meaning that the manipulation of non-degenerate FWM conversion bandwidth is feasible in practical real data wavelength conversion. The CE values in Fig. 6.21 (b) are -24.4, -20 and -28.1 dB, respectively. Last, the bit-error rate (BER) measurement is taken and the result is shown in Fig. 6.21 (c). The converted idlers without SBS and with gain-transparent SBS for maximum CE reach error-free detection level with power penalties of 1.3 and 0.9 dB, respectively. The error measurement for the one with gain-transparent SBS for minimum CE can only reach lowest BER of ~6.7×10^{-9} due to reduced OSNR. The results in Fig. 6.21 imply practical use of this scheme in real data wavelength conversion.

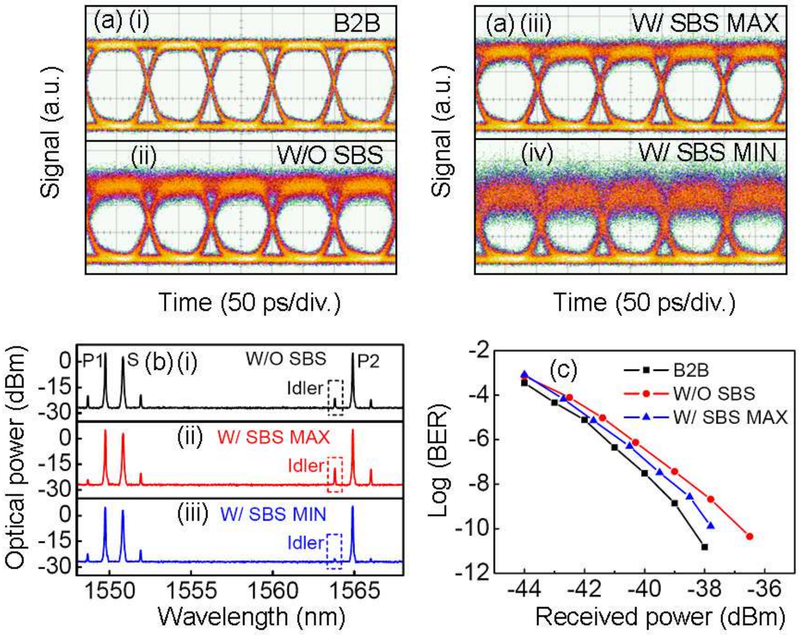

Fig. 6.21. Experimental results on all-optical manipulation of non-degenerate FWM bandwidth by gain-transparent SBS in wavelength conversion of 10 Gbit/s NRZ–OOK signal. The FWM pump 2 wavelength is 1564.9 nm. (a)(i)–(iv) eye diagrams of the input signal (B2B), converted idlers without SBS (W/O SBS), with gain-transparent SBS for maximum CE (W/ SBS MAX) and with gain-transparent SBS for minimum CE (W/ SBS MIN); (b)(i)–(iii) the corresponding FWM spectra; (c) BER measurement for input signal (B2B), converted idlers without SBS (W/O SBS) and with gain-transparent SBS for maximum CE (W/ SBS MAX).

6.5 Enhanced Performance of Polarization-insensitive Wavelength Conversion through Dynamic Control of Optical Phase

As mentioned in the previous sections, FWM processing is often limited by two major factors: stringent requirement on the polarization states of the interacting fields and phase matching among the optical components. The two obstacles result in polarization-dependent performance and limited conversion bandwidth, respectively. To suppress polarization dependence, several schemes have been proposed such as splitting a single pump into two orthogonal branches [28, 29], exploiting residual birefringence in a photonic crystal fiber (PCF) [30, 31], and using configurations with two co-polarized pumps [1, 32] or two orthogonal pumps [33, 34]. Nevertheless, it is difficult to simultaneously realize both polarization-insensitive operation and wideband wavelength conversion in a dual-pump FWM wavelength converter due to opposite requirements on pump wavelength spacing: small spacing for polarization-insensitive operation and large spacing for wideband operation. Although the configuration in Ref. [31] provides a potential solution to this problem, it requires sufficient pump-probe detuning which in turn sets a limit on the conversion bandwidth. Here, we propose and experimentally demonstrate the feasibility in achieving both the properties of polarization-insensitive and wideband operation in a dual orthogonal-pump wavelength converter. The scheme relies on gain-transparent SBS to control the optical phase of one of the pumps.

6.5.1 Principle and Experiment Setup

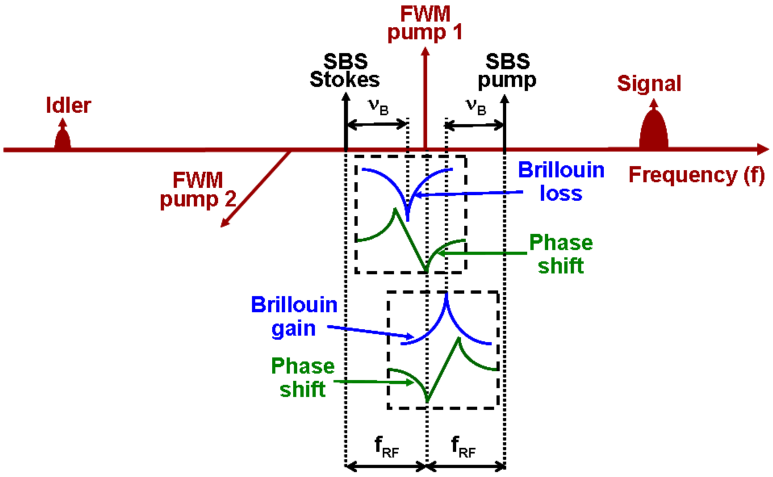

Fig. 6.22 Principle of wideband polarization-insensitive wavelength conversion assisted by gain-transparent SBS. ν_B *: Brillouin frequency shift;* f_{RF}*: frequency spacing between SBS pump and signal, and between signal and SBS Stokes wave.*

The principle of wideband polarization-insensitive wavelength conversion assisted by gain-transparent SBS is shown in Fig. 1. In this dual-pump FWM, the signal and the FWM pumps co-propagate in an optical fiber, with the two pumps orthogonal to each other for polarization-insensitive operation [33]. The phase control principle is the same as that described in Section 6.2. Here, both the optical gain and loss are introduced on the FWM pump 1 by the counter-propagating SBS pump and Stokes waves, respectively. To realize wideband operation, one can re-establish the nearly phase-matched condition at large spectral spacing by adjusting the frequency f_{RF}, and hence enhance the conversion efficiency (CE), without affecting the initial parameters of FWM.

The experimental setup is shown in Fig. 6.23. The output of a tunable laser (TL1) at 1553.8 nm is split into two branches. The upper branch is amplified by an EDFA to

10.3 dBm and serves as the FWM pump 1. The lower branch is modulated by an EOM biased to suppress the optical carrier and driven at a frequency f_{RF}. The carrier suppression ratio is about 23 dB. The two sidebands act as the SBS pump and Stokes waves after amplification by an EDFA to 15 dBm. FWM pump 2 is provided by a tunable laser 2 (TL2) at 1554.8 nm and is boosted to a power of 10.3 dBm by an EDFA. The two pumps are combined through a polarization beam splitter (PBS) to ensure that they are orthogonally polarized. A 10 Gbit/s NRZ–OOK signal is generated by intensity modulation of another tunable laser 3 and then amplified to 7.6 dBm through another EDFA. A polarization scrambler is used to vary the state of polarization (SOP) of the signal. Then the signal together with the FWM pumps are directed to a 1 km dispersion-flattened HNLF where polarization-insensitive FWM

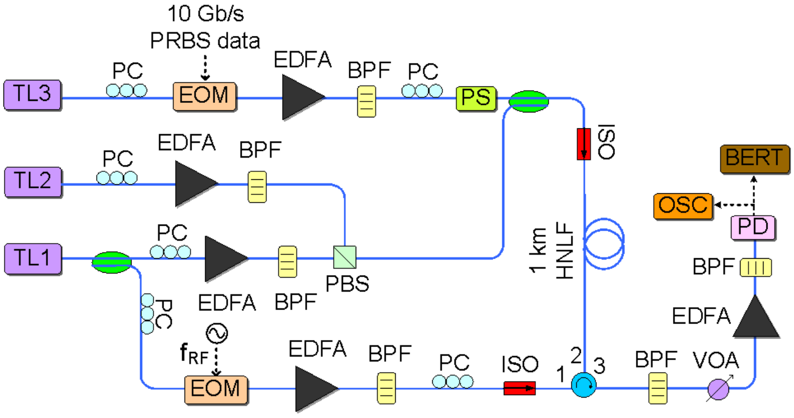

Fig. 6.23. Experimental setup. TL: tunable laser; EOM: electro-optic intensity modulator; EDFA: erbium-doped fiber amplifier; PC: polarization controller; BPF: band pass filter; PBS: polarization beam splitter; PS: polarization scrambler; HNLF: highly nonlinear fiber; ISO: isolator; OSA: optical spectrum analyzer; VOA: variable optical attenuator; PD: photodetector; OSC: oscilloscope; BERT: bit error rate tester.

takes place in the presence of the counter-propagating SBS pump and Stokes waves. The HNLF is the same as that used in Section 6.2. A BPF is used at the port 3 of the circulator to extract the converted idler for detection and measurement.

6.5.2 Results and Discussion

At first we tune the signal wavelength to be 1550.8 nm, in order to investigate the polarization-insensitive performance under the gain-transparent SBS processing. Fig. 6.24 (a)(i) and (b)(i) show the eye diagrams of the converted idler when the SBS pump and Stokes waves are absent. The scrambler is tuned off in Fig. 6.24 (a) while it is turned on in Fig. 6.24 (b). The SOP of the signal in Fig. 6.24 (a) is optimized to enhance the CE. Obviously the largely opened eye in Fig. 6.24 (b)(i) shows the polarization-insensitive operation. The corresponding FWM spectrum for Fig. 6.24 (a)(i) is shown in Fig. 6.24 (c)(i), indicating a CE of –29.8 dB. The measured bit-error rate (BER) performance for Fig. 6.24 (a)(i) is given in Fig. 6.24 (d), showing a power penalty of ~1.3 dB compared to the input signal at the error free detection level. Then the gain-transparent SBS is applied. The CE is maximized through minimizing the phase mismatch by tuning the driving frequency f_{RF}. During the experiment, the measured power variation of the FWM pump 1 is below 1.5 dB. The resulted eye diagrams of the converted idler are plotted in Fig. 6.24 (a)(ii) and (b)(ii), respectively. We can see the polarization-insensitive scheme also works well under gain-transparent SBS processing. The maximum CE under gain-transparent SBS is –26.3 dB, measured from the FWM spectrum in Fig. 6.24 (c)(ii). From the BER results in Fig. 6.24 (d), the converted idler with maximum CE shows a power penalty of ~0.8 dB.

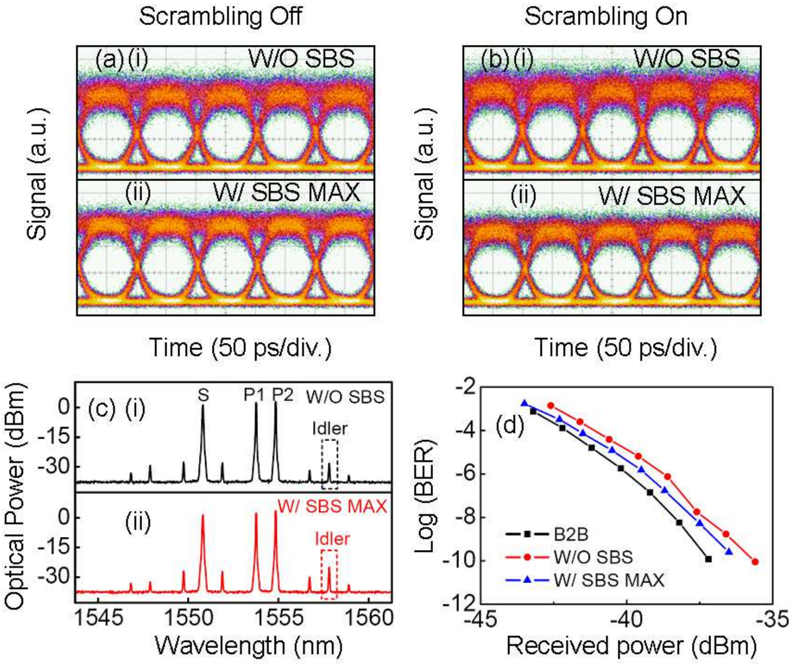

Fig. 6.24. Experimental results on wideband polarization-insensitive wavelength conversion of 10 Gbit/s NRZ-OOK signal assisted by gain-transparent SBS. The signal wavelength is set at 1550.8 nm. (a) and (b) (i)–(ii) eye diagrams of the converted idlers without SBS (W/O SBS) and with gain-transparent SBS for maximum CE (W/ SBS MAX); (c)(i)–(ii) the corresponding FWM spectra; (d) BER measurement for input signal (B2B), converted idlers without SBS (W/O SBS) and with gain-transparent SBS for maximum CE (W/ SBS MAX).

In order to quantify the polarization-insensitive performance under the gain-transparent SBS processing, we also measured the output power of the converted idler against the SOP of the input signal. The result is depicted in Fig. 6.25. As a comparison to the polarization-sensitive idler, the output power of the idler generated by degenerate FWM between the signal and FWM pump 1 is also plotted in Fig. 6.25 (black squares), showing a power variation of 6.3 dB as the SOP of the input signal is changed. Consequently, its eye diagram is very noisy when the scrambler is turned on, as shown in Fig. 6.26 (b). The variations are greatly suppressed to only 0.8 dB

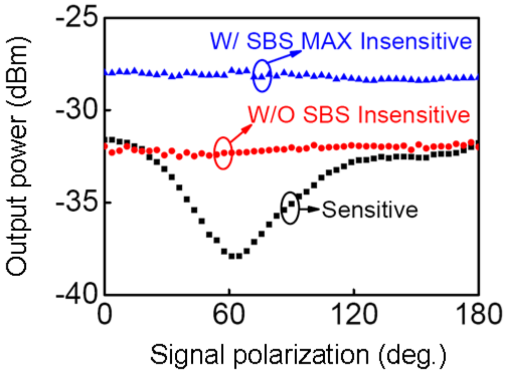

Fig. 6.25 Output power of the converted idler against the state of polarization (SOP) of the input signal. The red dots and blue triangles represent the polarization-insensitive idlers without SBS (W/O SBS Insensitive) and with gain-transparent SBS for maximum CE (W/ SBS MAX Insensitive). The black squares indicate the polarization-sensitive idler (sensitive) generated by degenerate FWM between the signal and FWM pump 1. The signal wavelength is set at 1550.8 nm.

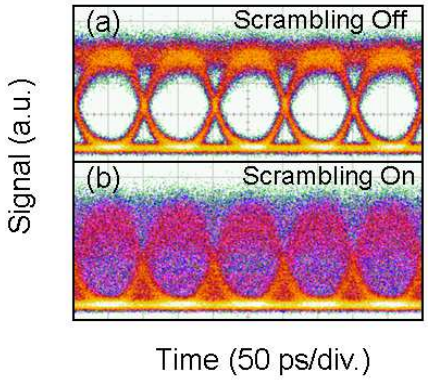

Fig. 6.26 Eye diagrams of the polarization-sensitive idler generated by degenerate FWM between the signal and FWM pump 1 when the scrambler is (a) off; (b) on. The signal wavelength is set at 1550.8 nm.

and 0.5 dB for the polarization-insensitive idler without SBS and with gain-transparent SBS for maximum CE, respectively, as depicted in Fig. 6.25. The output power of the idler with gain-transparent SBS is larger than that of the one without SBS due to the higher CE under gain-transparent SBS. The result in Fig. 6.25 confirms that not only the polarization-insensitive property is well maintained under gain-transparent SBS processing, but also the insensitive performance is further enhanced by the SBS processing.

To demonstrate the potential of this scheme on wideband wavelength conversion, we need to start with a low CE at a larger spectral spacing between the signal and the FWM pumps and then employ the gain-transparent SBS to enhance it by minimizing the phase mismatch. For this purpose the signal wavelength is tuned to 1549.8 nm. The measured results are depicted in Fig. 6.27. The FWM spectrum in Fig. 6.27 (c)(i) shows the CE without SBS is –35.8 dB, which is 6 dB worse than the case in Fig. 6.24 (c)(i). Consequently, a small eye opening is observed for the converted idler, as shown in Fig. 6.27 (a)(i) and (b)(i). Due to the low CE, the converted idler cannot reach error free detection level and the lowest measured BER is ~10^{-5}. When the SBS pump and Stokes waves are applied to the FWM pump 1, we have achieved a maximum CE of –30.7 dB. A CE enhancement of 5.1 dB is obtained due to re-establishment of the nearly phase-matched condition through gain-transparent SBS. The increase in CE gives rise to a widely opened eye of the converted idler (Fig. 6.27 (a)(ii) and (b)(ii)) and error free detection with a power penalty of ~0.9 dB (Fig. 6.27 (d)). Again, the polarization-insensitive property is successfully preserved under gain transparent SBS processing but with strongly enhanced performance compared to that in Fig. 6.27 (b)(i). The large enhancement in CE greatly supports this scheme in achieving wideband wavelength conversion and simultaneously maintaining the polarization-insensitive operation.

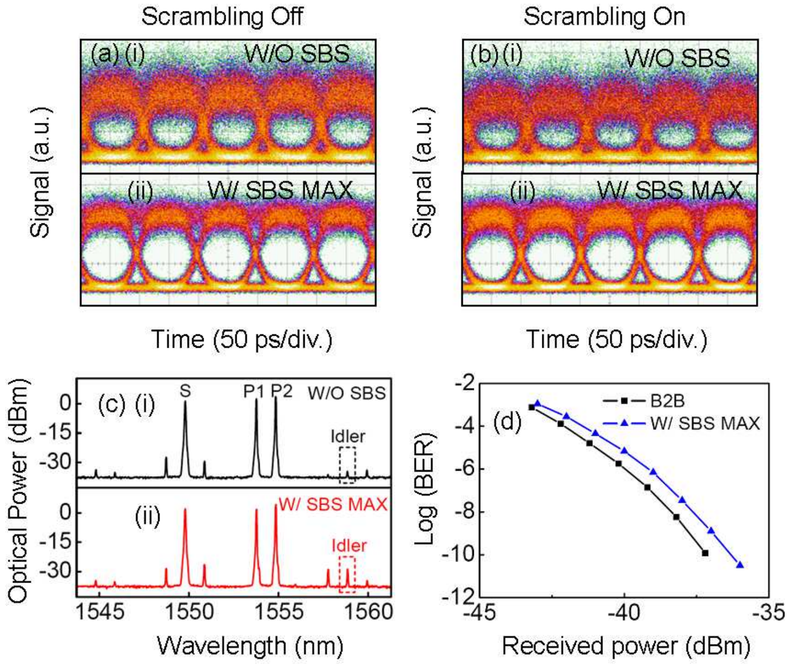

Fig. 6.27 Experimental results on wideband polarization-insensitive wavelength conversion of 10 Gbit/s NRZ-OOK signal assisted by gain-transparent SBS. The signal wavelength is set at 1549.8 nm. (a) and (b) (i)–(ii) eye diagrams of the converted idlers without SBS (W/O SBS) and with gain-transparent SBS for maximum CE (W/ SBS MAX); (c)(i)–(ii) the corresponding FWM spectra; (d) BER measurement for input signal (B2B) and converted idler with gain-transparent SBS for maximum CE (W/ SBS MAX).

6.6 Extension of the Maximum Optical Delay using Gain-Transparent-SBS-Controlled FWM Wavelength Conversion and Group Velocity Dispersion

Tunable optical delay has attracted much research interest because of its wide applications in optical communications, optical signal processing, and microwave photonics. Examples of the applications are all-optical routing [36], optical multiplexing/demultiplexing [37, 38], arbitrary waveform generation [39], optical control of phased array antennas [40] and optical correlation [41]. Different approaches have been proposed to realize tunable optical delay line in the past two decades [42-56]. One of the approaches is to switch optical light between different optical paths [42], although it can not be used to achieve continuously tunable delay. Continuous optical delay can be achieved by employing the slow light technique [43-49], where a rapid change of refractive index happens within a narrow spectral resonance. Electromagnetically induced transparency [43], coherent population oscillation [44], stimulated Brillouin and Raman scattering [16, 45, 46], and optical parametric amplification [47] have all been employed in slowing down optical signals. In particular, the slow light technique based on SBS provides a promising way of delaying ~Gbit/s optical data [48]. Although delay values of several pulse periods have been demonstrated with this approach, a fundamental delay-bandwidth issue limits the maximum achievable delay for a given signal bandwidth [49]. A larger tunable delay range is usually achieved by the wavelength conversion and dispersion scheme [50-56]. The wavelength of the input signal is first converted to an idler wavelength based on a parametric process. The signal is then fed into a dispersive medium with a large group-velocity dispersion (GVD), which generates a wavelength-dependent delay with respect to the initial optical signal. The total delay is the product of the GVD parameter, the length of the dispersive medium, and the wavelength shift. As a result, the delay can be tuned by changing the wavelength of the converted idler and the tuning range can be extended by lengthening the dispersive medium or broadening the wavelength conversion bandwidth.

In this section, we experimentally demonstrate for the first time the extension of the maximum achievable delay by enlarging the FWM conversion bandwidth with the use of gain-transparent SBS to control purely the phase difference among the fields. We make use of the enlarged bandwidth and apply it in a tunable delay line in order to extend the maximum achievable delay.

6.6.1 Principle and Experimental Setup

Our tunable delay line consists of two parts. The first part is a wavelength converter based on degenerate FWM in a 1 km dispersion-flattened highly nonlinear fiber (HNLF). The second part induces the wavelength dependent group delay by passing the converted signal through a dispersive medium. Here we use a chirped fiber Bragg grating (CFBG) as the dispersive element. The total group delay is expressed as

$$\Delta t = D \cdot \Delta \lambda_i = D \cdot (2\Delta \lambda_p) \qquad (6\text{-}13)$$

where D is the dispersion coefficient of the CFBG, $\Delta\lambda_i$ and $\Delta\lambda_p$ are the wavelength shift for the idler and pump, respectively. As can be seen from Equation (6-13), a larger wavelength shift is desirable to maximize the achievable delay and hence reduce the required dispersion to achieve a given time delay. In order to enlarge the wavelength shift and hence maximize the delay, we apply our dynamic control of phase-matching technique through gain-transparent SBS to the wavelength converter of a tunable delay line, and realize the extension of the achievable delay.

The principle of using gain-transparent SBS to control the optical phase of the FWM pump for wavelength conversion of data signals is explained in detail in Section 6.3. Fig. 6.28 shows the principle again. Here, we do not repeat the explanation which can be found in Section 6.3.

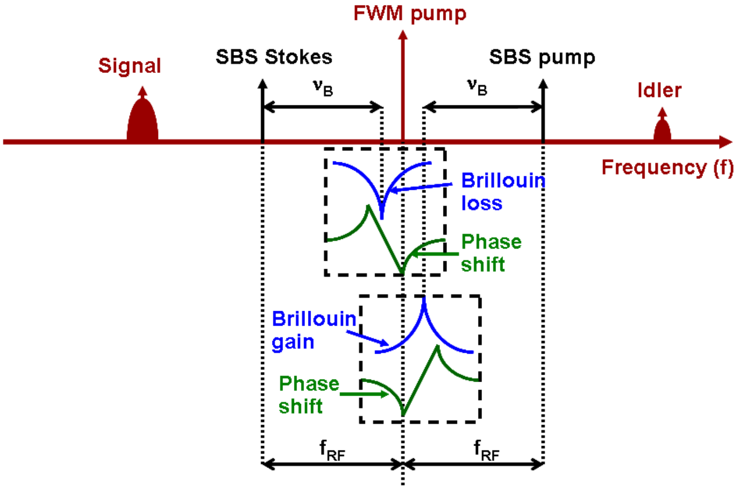

Fig. 6.28. Principle for dynamic control of phase-matching in FWM wavelength conversion of data signals using gain-transparent SBS. ν_B *: Brillouin frequency shift;* f_{RF}*: frequency spacing between SBS pump and signal, and between signal and SBS Stokes wave.*

The experimental setup for extension of tunable delay with the use of gain-transparent SBS for bandwidth enlargement is shown in Fig. 6.29. The output of a tunable laser (TL1) is split into two branches. The upper branch is amplified by an

EDFA to 9.9 dBm and serves as the FWM pump. The lower branch is modulated by an EOM biased to suppress the optical carrier and driven at a frequency f_{RF}. The carrier suppression ratio is about 23 dB. The two sidebands act as the SBS pump and Stokes waves after amplification by an EDFA to 14.2 dBm. A 10 Gbit/s NRZ–OOK signal is generated by intensity modulation of another tunable laser 2 at 1549.8 nm. The signal is amplified to 5.9 dBm through another EDFA. It is then combined with the FWM pump using a 3 dB coupler. The signal together with the FWM pump are directed to a 1 km HNLF where FWM takes place in the presence of the counter-propagating SBS pump and Stokes waves. The HNLF is the same as that used in Section 6.2. The converted idler is extracted by a BPF at the port 3 of the first circulator and is then reflected by a CFBG where the tunable delay is introduced. The CFBG has a 30 nm reflection bandwidth starting from 1535 nm, and a dispersion

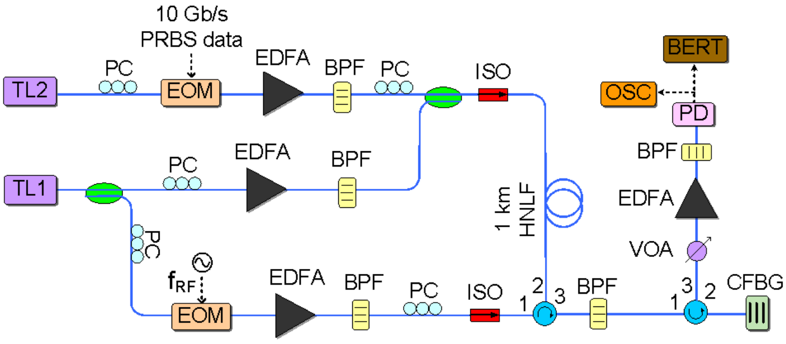

Fig. 6.29. Experimental setup for extension of tunable delay with the use of gain-transparent SBS for bandwidth enlargement. TL: tunable laser; EOM: electro-optic intensity modulator; EDFA: erbium-doped fiber amplifier; PC: polarization controller; BPF: band pass filter; HNLF: highly nonlinear fiber; ISO: isolator; OSA: optical spectrum analyzer; VOA: variable optical attenuator; PD: photodetector; OSC: oscilloscope; BERT: bit error rate tester, CFBG: chirped fiber Bragg grating.

coefficient of 21 ps/nm. Finally the reflected idler is detected by a photodetector and displayed on an oscilloscope for the measurement of the time delay.

6.6.2 Results and Discussion

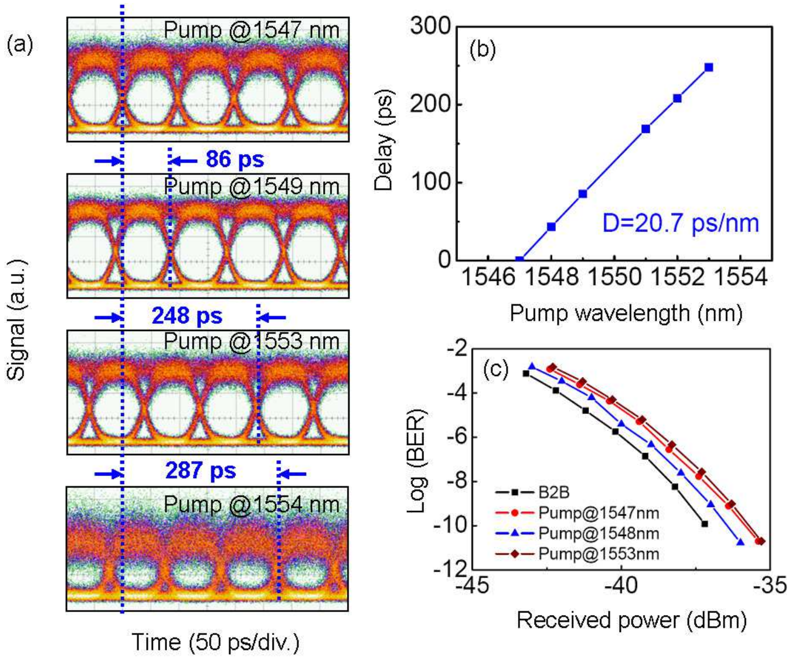

Fig. 6.30. (a) Eye diagrams of the delayed idlers at different wavelength; (b) the delay time against the pump wavelength; (c) BER performance of the input signal (B2B) and delayed idlers. Gain-transparent SBS is not applied.

As a comparison to the case where the gain-transparent SBS is used to extend the maximum delay, we first measure the tunable delay when the SBS pump and Stokes waves are turned off. The results are depicted in Fig. 6.30. The pump wavelength is tuned from 1546 to 1554 nm with a step of 1 nm. When the pump is at 1546 and 1554 nm, we find that the delayed idlers can not reach error-free detection level because the FWM CE decreases greatly at a large signal-pump spectral spacing. Therefore, the pump tuning range should be confined from 1547 to 1553 nm where error-free detection is possible for all the delayed idlers. Fig. 6.30 (a) shows the eye diagrams of the delayed idlers at different pump wavelengths. The one obtained with a weak FWM CE at a pump wavelength of 1554 nm is also shown although the delay is not considered as within the tunable delay range. Fig. 6.30 (b) plots the time delay versus the pump wavelength, showing a maximum delay of 248 ps achieved at a pump wavelength of 1553 nm. The measured dispersion coefficient of 20.7 ps/nm agrees well with that of the CFBG. Fig. 6.30 (c) shows the measured bit-error rate (BER) performance for the idlers at different delays. Compared to the input signal at the error free detection level, the power penalties are 1.3, 0.8 and 1.5 dB for the pump wavelength of 1547, 1548 and 1553 nm, respectively.

Next, the SBS pump and Stokes waves are turned on. By adjusting the driving frequency f_{RF}, the CE can be enhanced significantly for large signal-pump spectral spacing through minimizing the phase mismatch. To examine the performance of the SBS processing on the tunable delay, the pump wavelength is first tuned to 1554 nm to study the signal quality of the delayed idler. The measured results are depicted in Fig. 6.31. The case without SBS is obtained from the bottom plot of Fig. 6.30(a) and is reproduced in Fig. 6.31 (a)(i). The corresponding CE is as low as –32.1 dB. Consequently, a small eye opening is observed for the delayed idler. However, when the SBS pump and Stokes waves are applied to the FWM pump, we have achieved a maximum CE of –25.1 dB. A significant CE enhancement of 7 dB is obtained due to re-establishment of the nearly phase-matched condition through gain-transparent SBS. The increase in CE gives rise to a widely opened eye of the delayed idler (Fig. 6.31 (a)(ii)) and error free detection. The performances at other pump wavelengths are also examined, as shown in Fig. 6.32. The eye diagrams of the delayed idlers

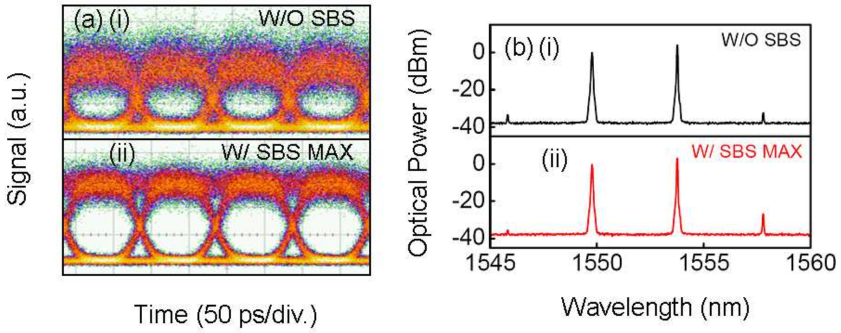

Fig. 6.31. (a)(i)–(ii) eye diagrams of the delayed idler without SBS (W/O SBS) and with gain-transparent SBS for maximum CE (W/ SBS MAX); (b)(i)–(ii) the corresponding FWM spectra. The pump wavelength is 1554 nm.

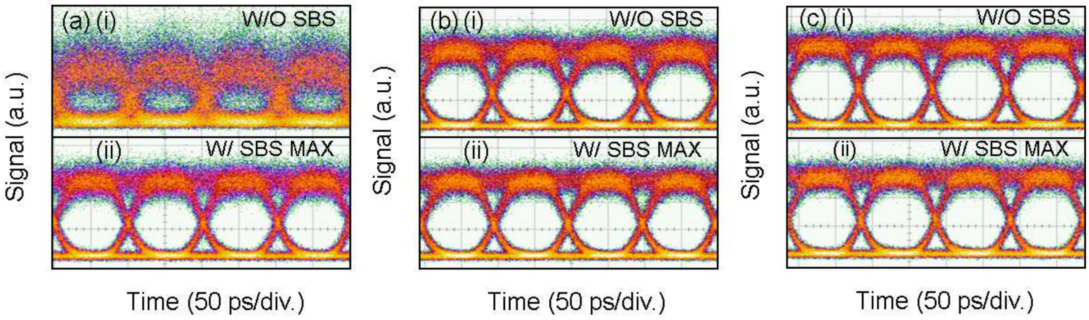

Fig. 6.32. Eye diagrams of the delayed idler without SBS (W/O SBS) and with gain-transparent SBS for maximum CE (W/ SBS MAX) when the pump is tuned at (a) 1546 nm, (b) 1547 nm, and (c) 1548 nm.

without SBS are obtained from the same experiment with results shown in Fig. 6.30 but additional wavelengths have been used. The corresponding CE for pump wavelengths at 1546, 1547, and 1548 nm are –34.4 dB, –26.1 and –24.7 dB, respectively. After the SBS processing, the CE is maximized to be –24.9 dB, –24.2 and –23.7 dB, respectively. The most noticeable enhancement (9.5 dB) in the CE occurs at a pump wavelength of 1546 nm, resulting in large eye opening of the delayed idler (Fig. 6.32 (a)(ii)) in comparison to that without SBS (Fig. 6.32 (a)(i)).

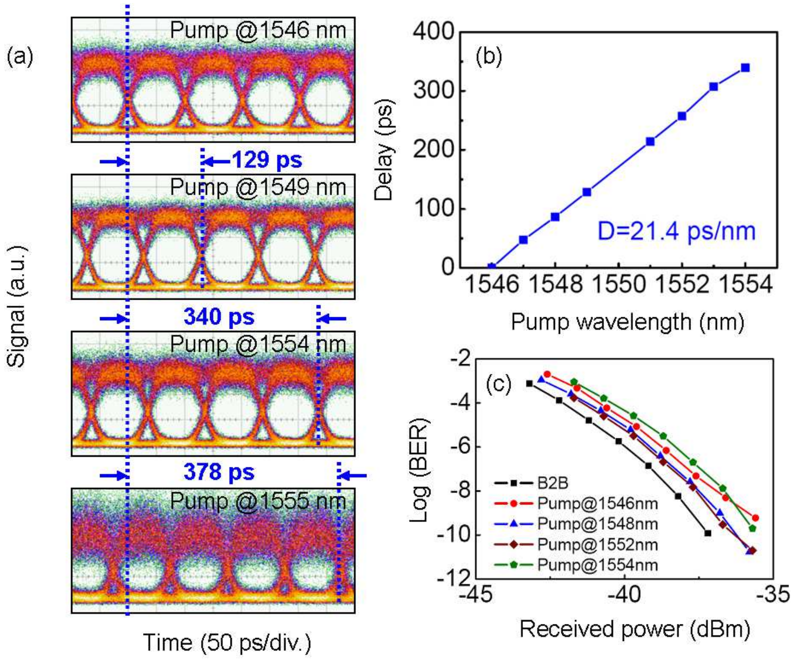

Fig. 6.33. (a) Eye diagrams of the delayed idlers at different wavelengths; (b) the delay time against the pump wavelength; (c) BER performance of the input signal (B2B) and delayed idlers. Gain-transparent SBS is applied to extend the maximum delay.

Hence, error-free operation can be obtained. In Fig. 6.31 and Fig. 6.32, as the pump wavelength is tuned to produce a larger wavelength shift in Equation (6-13), the time delay becomes larger. The result of the tunable delay under gain-transparent SBS processing are given in Fig. 6.33. The CE for each pump wavelength is maximized by tuning the driving frequency f_{RF}. The resulted pump tuning range spans from 1546 to 1554 nm in order to obtain error-free detection of the delayed idler. The delayed idlers at error-free detection level and the one with low FWM CE at a pump wavelength of 1555 nm are both shown in Fig. 6.33 (a). The delay values at other pump wavelengths are given in Fig. 6.33 (b) where a maximum delay of 340 ps is achieved at a pump wavelength of 1554 nm. A delay slope of 21.4 ps/nm is observed. The maximum delay under gain-transparent SBS is increased by 92 ps, that is 37% increase when compared to that without SBS processing. In theory, the percentage of the delay increase should be the same as that of the bandwidth increase in Ref. [27]. Here, since we tune the pump wavelength in steps of 1 nm, the calculation of the bandwidth increase or delay increase should have a little deviation from that in Ref. [27] which provides more exact values. The BER performance for the idlers at different delays under gain-transparent SBS is measured and depicted in Fig. 6.33 (c). The power penalties are 2.0, 1.0, 0.9 and 1.7 dB for the pump wavelengths of 1546, 1548, 1552 and 1554 nm, respectively.

References

[1] J. Ma, J. Yu, C. Yu, Z. Jia, X. Sang, Z. Zhou, T. Wang, and G. K. Chang, “Wavelength Conversion Based on Four-Wave Mixing in High-Nonlinear Dispersion Shifted Fiber Using a Dual-Pump Configuration,” IEEE J. Lightw. Technol., Vol. 24, no. 7, pp. 2851–2858 (2006).

[2] M. F. Huang, J. Yu, and G. K. Chang, “Polarization Insensitive Wavelength Conversion for 4×112Gbit/s Polarization Multiplexing RZ-QPSK Signals,” Opt. Express, vol. 16, no. 25, pp. 21161-21169, 2008.

[3] K. Uesaka, K. Wang, M. E. Marhic, and L. G. Kazovsky, “Wavelength exchange in a highly nonlinear dispersion-shifted fiber: theory and experiments,” IEEE J. Quantum Electron., vol. 18, pp. 560–568 (2002).

[4] Y. Liu, E. Tangdiongga, Z. Li, H. de Waardt, A. M. J. Koonen, G. D. Khoe, H. J. S. Dorren, X. Shu, and I. Bennion, “Error-free 320 Gb/s SOA-based wavelength conversion using optical filtering,” in Proc. OFC 2006, paper PDP28.

[5] W. Wang, H. N. Poulsen, L. Rau, H. F. Chou, J. E. Bowers, and D. J. Blumenthal, “Raman-enhanced regenerative ultrafast all-optical fiber XPM wavelength converter,” J. Lightwave Technol., vol. 23, pp. 1105–1115 (2005).

[6] L.-S. Yan, A.-L. Yi, W. Pan, B. Luo, and J. Ye, “Simultaneous NRZ-to-RZ format conversion and one-to-six error-free channel multicasting using a single pump in a highly nonlinear fiber,” Opt. Express, vol. 18, no. 20, pp. 21404–21409, September 2010.

[7] X. Wu, J. Wang, O. F. Yilmaz, S. R. Nuccio, A. Bogoni, and A. E. Willner, “Bit-rate-variable and order-switchable optical multiplexing of high-speed

pseudorandom bit sequence using optical delays," Opt. Lett., vol. 35, no. 18, pp. 3042–3044, September 2010.

[8] L. Wang, Y. Dai, K. P. Lei, J. Du, and C. Shu, "All-optical RZ-to-NRZ and NRZ-to-PRZ format conversions based on delay-asymmetric nonlinear loop mirror," IEEE Photon. Technol. Lett., vol. 23, no. 6, pp. 368–370, March 2011.

[9] M. Matsuura, N. Kishi, and T. Miki, "Broadband regenerative wavelength conversion and multicasting using triple-stage semiconductor-based wavelength converters," Opt. Lett., vol. 23, pp. 1026–1028 (2007).

[10] X. Fu, Y. Dai, G. K. P. Lei, and C. Shu, "Bit-rate flexible demodulation of DPSK signals based on phase sensitive gain in cascaded four-wave mixing," IEEE Photon. Technol. Lett., vol. 24, no. 12, 994–996, June 2012.

[11] M. P. Fok, C. Shu, and D. J. Blumenthal, "Dual-pump four-wave mixing in Bismuth-oxide highly nonlinear fiber for wide-band DPSK wavelength conversion," in Proc. OFC/NFOEC 2007, paper JThA52.

[12] G. P. Agrawal, *Nonlinear Fiber Optics*, The Netherlands: Elsevier, Amsterdam, 2009.

[13] K. Inoue, "Four-wave mixing in an optical fiber in the zero-dispersion wavelength region," IEEE J. Lightw. Technol., vol. 10, no. 11, pp. 1553–1561, November 1992.

[14] K. P. Hansen, J. R.. Folkenberg, C. Peucheret, and A. Bjarklev, "Fully dispersion controlled triangular-core nonlinear photonic crystal fiber", in Proc. OFC/NFOEC 2003, Atlanta, March 2003, paper PD2.

[15] E. Mateo, F. Yaman, and G. Li, "Control of four-wave mixing phase-matching condition using the Brillouin slow-light effect in fibers," Opt. Lett., vol. 33, no. 5, pp. 488–390, March 2008.

[16] Y. Okawachi, M. S. Bigelow, J. E. Sharping, Z. Zhu, A. Schweinsberg, D. J. Gauthier, R. W. Boyd, and A. L. Gaeta, “Tunable All-Optical Delays via Brillouin Slow Light in an Optical Fiber,” Phys. Rev. Lett., vol. 94, 153902, April 2005.

[17] J. Hansryd, P. A. Andrekson, M. Westlund, J. Li, and P. Hedekvist, “Fiber-Based Optical Parametric Amplifiers and Their Applications,” IEEE J. Sel. Topics Quantum Electron., vol. 8, no. 3, pp. 506–520, May/June 2002.

[18] A. Loayssa, and F. J. Lahoz, “Broad-band RF photonic phase shifter based on stimulated Brillouin scattering and single-sideband modulation,” IEEE Photon. Technol. Lett., vol. 18, no. 1, pp. 208-210, January 2006.

[19] J. H. Lee, K. Y. Song, H. J. Yoon, J. S. Kim, T. Hasegawa, T. Nagashima, S. Ohara, and N. Sugimoto, “Brillouin gain-coefficient measurement for bismuth-oxide-based photonic crystal fiber under significant beam reflection at splicing points,” Opt. Lett., vol. 34, no. 17, pp. 2670-2672, September 2009.

[20] S. Takasaka, Y. Mimura, M. Takahashi, R. Sugizaki, and H. Ogoshi, “Flat and Broad Amplification by Quasi-Phase-Matched Fiber Optical Parametric Amplifier,” in Proc. OFC/NFOEC 2012, Los Angeles, March 2012, paper OTh1C.4.

[21] N. E. Dahdah, D. S. Govan, M. Jamshidifar, N. J. Doran, and M. E. Marhic, “Fiber Optical Parametric Amplifier Performance in a 1-Tb/s DWDM Communication System,” IEEE J. Sel. Topics Quantum Electron., vol. 18, no. 2, pp. 950–957, March/April 2012.

[22] Z. Tong, C. Lundström, P. A. Andrekson, C. J. McKinstrie, M. Karlsson, D. J. Blessing, E. Tipsuwannakul, B. J. Puttnam, H. Toda, and L. Grüner-Nielsen,

"Towards ultrasensitive optical links enabled by low-noise phase-sensitive amplifiers," Nature Photon., vol. 5, pp. 430–436, June 2011.

[23] T. Tanemura, C. S. Goh, K. Kikuchi, and S. Y. Set, "Highly Efficient Arbitrary Wavelength Conversion Within Entire C-Band Based on Nondegenerate Fiber Four-Wave Mixing," IEEE Photon. Technol. Lett., vol. 16, no. 2, pp. 551–553, February 2004.

[24] D. M´echin, R. Provo, J. D. Harvey and C. J. McKinstrie, "180-nm wavelength conversion based on Bragg scattering in an optical fiber," Opt. Express., vol. 14, no. 20, pp. 8995–8999, October 2006.

[25] Y. Dai, and C. Shu, "Widely Tunable Polarization-Insensitive Nondegenerate Four-Wave Mixing Wavelength Conversion for DPSK Signal," IEEE Photon. Technol. Lett., vol. 22, no. 15, pp. 1138–1140, August 2010.

[26] L. Wang, and C. Shu, "Four-wave mixing bandwidth enlargement using phase-matching control by gain-transparent stimulated Brillouin scattering," in Photonics in Switching Conference, Ajaccio-Corsica, France, September 2012, postdeadline paper 2.

[27] L. Wang, and C. Shu, "Dynamic Control of Phase Matching in Four-Wave Mixing Wavelength Conversion of Amplitude- and Phase- Modulated Signals," IEEE J. Lightw. Technol., vol. 31, no. 9, pp. 1468–1474, May 2013.

[28] T. Hasegawa, K. Inoue, and K. Oda, "Polarization independent frequency conversion by fiber four-wave mixing with a polarization diversity technique," IEEE Photon. Technol. Lett., vol. 5, no. 8, pp. 947–949 (1993).

[29] T. Yang, C. Shu, and C. Lin, "Depolarization technique for wavelength conversion using four-wave mixing in a dispersion-flattened photonic crystal fiber," Opt. Express, vol. 13, no. 14, pp. 5409–5415 (2005).

[30] W. Astar, A. S. Lenihan, and G. M. Carter, “Polarization-insensitive wavelength conversion by FWM in a highly nonlinear PCF of polarization-scrambled 10-Gb/s RZ-OOK and RZ-DPSK signals,” IEEE Photon. Technol. Lett., vol. 19, no. 20, pp. 1676–1678 (2007).

[31] Y. Dai, and C. Shu, “Widely Tunable Polarization-Insensitive Nondegenerate Four-Wave Mixing Wavelength Conversion for DPSK Signal,” IEEE Photon. Technol. Lett., vol. 22, no. 15, pp. 1138–1140 (2010).

[32] X. Li, J. Yu, Z. Dong, and N. Chi, “Wavelength conversion of 544-Gbit/s dual-carrier PDM-16QAM signal based on the co-polarized dual-pump scheme,” Opt. Express., vol. 20, no. 19, pp. 21324-21330 (2012).

[33] K. Inoue, “Polarization independent wavelength conversion using fiber four-wave mixing with two orthogonal pump lights of different frequencies,” J. Lightw. Technol., vol. 12, no. 11, pp. 1916–1920 (1994).

[34] Z. Dong, J. Yu, H. C. Chien, L. Chen, and G. K. Chang, “Wavelength conversion for 1.2Tb/s optical OFDM superchannel based on four-wave mixing in HNLF with digital coherent detection,” in Proc. of ECOC 2011, paper Th.11.LeSaleve.5.

[35] M. P. Fok, C. Shu, and D. J. Blumenthal, “Dual-pump four-wave mixing in Bismuth-oxide highly nonlinear fiber for wide-band DPSK wavelength conversion,” in Proc. OFC/NFOEC 2007, paper JThA52.

[36] R. Ramaswami, and K. N. Sivarajan, “Routing and wavelength assignment in all-optical networks,” IEEE/ACM Trans. Netw. 3(5), 489–500 (1995).

[37] X. Wu, J. Wang, O. F. Yilmaz, S. R. Nuccio, A. Bogoni, and A. E. Willner, “Bit-rate-variable and order-switchable optical multiplexing of high-speed

pseudorandom bit sequence using optical delays," Opt. Lett., vol. 35, no. 18, pp. 3042-3044 (2010).

[38] X. Wu, S. R. Nuccio, O. F. Yilmaz, J. Wang, A. Bogoni, and A. E. Willner, "Controllable optical demultiplexing using continuously tunable optical parametric delay at 160 Gbit/s with <0.1 ps resolution," Opt. Lett., vol. 34, no. 24, pp. 3926-3928 (2009).

[39] Zh. Jiang, D. E. Leaird, and A. M. Weiner, "Line-by-line pulse shaping control for optical arbitrary waveform generation," Opt. Express., vol. 13, no. 25, pp. 10431-10439 (2005).

[40] J. L. Corral, J. Marti, J. M. Fuster, and R. I. Laming, "True time-delay scheme for feeding optically controlled phased-array antennas using chirped-fiber gratings," Photon. Technol. Lett., vol. 9, no. 11, pp. 1529-1531 (1997).

[41] R. Ramaswami, and K. N. Sivarajan, *Optical Networks: A Practical Perspective*, Morgan Kaufmann, 2002

[42] I. Kobayashi and K. Kuroda, "Step-type optical delay line using silicabased planar light-wave circuit (PLC) technology," IEEE Trans. Instrum. Meas., vol. 49, no. 4, pp. 762–765 (2000).

[43] M. M. Kash, V. A. Sautenkov, A. S. Zibrov, L. Hollberg, G. R.Welch, M. D. Lukin, Y. Rostovtsev, E. S. Fry, and M. O. Scully, "Ultraslow group velocity and enhanced nonlinear optical effects in a coherently driven hot atomic gas," Phys. Rev. Lett., vol. 82, pp. 5229–5232 (1999).

[44] M. S. Bigelow, N. N. Lepeshkin, and R. W. Boyd, "Observation of ultraslow light propagation in a ruby crystal at room temperature," Phys. Rev. Lett., vol. 90, no. 11, 113 903 (2003).

[45] K. Y. Song, M. G. Herráez, and L. Thévenaz, “Observation of pulse delaying and advancement in optical fibers using stimulated Brillouin scattering,” Opt. Express., vol. 13, no. 1, pp. 82-88 (2005).

[46] J. E. Sharping, Y. Okawachi, and A. L. Gaeta, “Wide bandwidth slow light using a Raman fiber amplifier,” Opt. Express, vol. 13, pp. 6092–6098 (2005).

[47] D. Dahan and G. Eisenstein, “Tunable all optical delay via slow and fast light propagation in a Raman assisted fiber optical parametric amplifier: a route to all optical buffering,” Opt. Express., vol. 13, no. 16, pp. 6234-6249 (2005).

[48] A. E. Willner, B. Zhang, L. Zhang, L. Yan, and I. Fazal, “Optical Signal Processing Using Tunable Delay Elements Based on Slow Light,” IEEE J. Sel. Topics Quantum Electron., vol. 14, no. 3, pp. 691-705 (2008).

[49] R. S. Tucker, P.-Ch. Ku, and C. J. Chang-Hasnain, “Slow-Light Optical Buffers: Capabilities and Fundamental Limitations,” J. Lightwave Technol., vol. 23, no. 12, pp. 4046-4066 (2005).

[50] M. P. Fok, and C. Shu, “Tunable Optical Delay Using Four-Wave Mixing in a 35-cm Highly Nonlinear Bismuth-Oxide Fiber and Group Velocity Dispersion,” J. Lightwave. Technol., vol. 26, no. 5, pp. 499-504 (2008).

[51] S. R. Nuccio, O. F. Yilmaz, X. Wang, J. Wang, X. Wu, A. E. Willner, “1.16 μs continuously tunable optcal delay of a 100-Gb/s DQPSK signal using wavelength conversion and chromatic dispersion in an HNLF,” in Proceeding of CLEO 2010, paper CFJ2.

[52] E. Myslivets, N. Alic, S. Moro, B. P. P. Kuo, R. M. Jopson, C. J. McKinstrie, M. Karlsson and S. Radic, “1.56-μs continuously tunable parametric delay line for a 40-Gb/s signal,” Opt. Express., vol. 17, no. 14, pp. 11958-11964 (2009).

[53] N. Alic, E. Myslivets, S. Moro, B.P.P. Kuo, R.M. Jopson, C.J. McKinstrie and S. Radic, “1.83-μs Wavelength-Transparent All-Optical Delay,” in Proceeding of OFC 2009, paper PDPA1.

[54] S. R. Nuccio, O. F. Yilmaz, X. Wang, H. Huang, J. Wang, X. Wu, and A. E. Willner, “Higher-order dispersion compensation to enable a 3.6 μs wavelength-maintaining delay of a 100 Gb/s DQPSK signal,” Opt. Lett., vol. 35, no. 17, pp. 2985-2987 (2010).

[55] N. Alic, E. Myslivets, S. Moro, B. P. P. Kuo, R. M. Jopson, C. J. McKinstrie, and S. Radic, “Microsecond Parametric Optical Delays,” J. Lightwave Technol., vol. 28, no. 4, pp. 448-455 (2010).

[56] Y. Dai, Y. Okawachi, A. C. Turner-Foster, M. Lipson, A. L. Gaeta, and C. Xu, “Ultralong continuously tunable parametric delays via a cascading discrete stage,” Opt. Express., vol. 18, no. 1, pp. 333-339 (2010).

7 DYNAMIC CONTROL OF GAIN PROFILE IN FIBER OPTICAL PARAMETRIC AMPLIFIER BY GAIN-TRANSPARENT SBS

Fiber optical parametric amplifier (FOPA) has attracted much research interest since the amplifier can provide a large gain over a relatively wide optical bandwidth [1-5]. Compared to EDFA, FOPA offers low-noise amplification and is now widely used in various applications [6-8]. However, before it is considered as a potential mechanism for amplifying optical waves, its development is halted for almost 15 years [9]. There are several reasons for this: (i) the lack of fibers with high nonlinearity; (ii) difficulty in maintaining phase-matching condition due to longitudinal variations of the fiber zero-dispersion wavelength (ZDW) λ_0; (iii) the lack of high-power and narrow-linewidth CW pump sources. Because of these limitations, in the mid-1980s FOPA could not compare well with other amplifiers, i.e. Raman amplifiers and EDFAs. Especially in the late 1980s, the success in the development of EDFAs made people believe that there was little need for designing an alternate type of optical amplifier and hence the research on FOPA moved forward slowly.

A milestone of FOPA was laid down in 1996 when Marhic et al. demonstrated a single-pump FOPA in a conventional fiber with a gain bandwidth of hundreds of nanometers by tuning the pump wavelength near ZDW [10]. The pump power is in the order of 1 W which is a level attainable nowadays in many laboratories. Such a bandwidth significantly exceeds those of EDFA and Raman amplifiers that are currently used in optical communication systems, indicating that FOPA should have great potential in future optical communications. Later, with the advent of new optical components such as specially designed fibers with high nonlinearities and ZDW around 1550 nm, and tunable lasers and EDFAs for generating high-power and narrow-linewidth pumps, the development of FOPA was resumed in the recent years and has received increasing attention. Spurred by steady advances in the required components and techniques, FOPA is likely to play an important role for different applications in the future.

In this chapter, we will focus on the phase-matching condition in a single-pump FOPA and use gain-transparent SBS to control the relative phase difference among the interacting fields, thus achieve dynamic gain profiles in a FOPA. The principle and experimental realization of the scheme are discussed in Section 7.2, following an introduction to FOPA in Section 7.1.

7.1 Introduction to FOPA

The FOPA exploits nonlinear optical properties of optical fibers originating from the third-order susceptibility $\chi^{(3)}$. It has some important properties listed as follows [9]:

- Gain bandwidth increasing with pump power
- Arbitrary center wavelength
- Large gain
- Wavelength conversion
- High-speed optical signal processing
- Low noise figure

FOPA can be implemented with single-pump configuration or multi-pump configuration. In single-pump configuration, the pump can be set at normal dispersion region or anomalous dispersion region. The difference between them lies in the different phase-matching condition and hence different gain profile. Usually the pump is positioned at anomalous dispersion region and near ZDW λ_0, as shown in Fig. 7.1. One part of the pump energy is transferred to the signal, resulting in OPA gain. The other part is consumed to generate the idler during the parametric process. In the anomalous dispersion region, the nonlinear phase mismatch can be compensated by the linear phase mismatch, leading to a gain profile with two wavelength bands symmetric to the pump wavelength λ_p. Each wavelength band has one peak gain achieved at the signal wavelength with perfect phase matching. Fig. 7.2 shows a typical gain spectrum in a single-pump FOPA with the pump positioned at 1551 nm with a power of 26 dBm. The gain medium is a highly nonlinear fiber (HNLF). It has a nonlinear coefficient of 11.7/(W·km), a zero-dispersion wavelength of 1549 nm, a dispersion coefficient of 0.02 ps/(nm·km), and a dispersion slope of

0.019 ps/(nm^2·km) at ~1550 nm. An M-shaped gain spectrum is observed with two symmetric wavelength band surrounding the pump wavelength. The gain bandwidth and the spacing between the peak gain wavelength and the pump wavelength are determined by both the power of the pump and the spacing between the zero-dispersion wavelength and the pump wavelength.

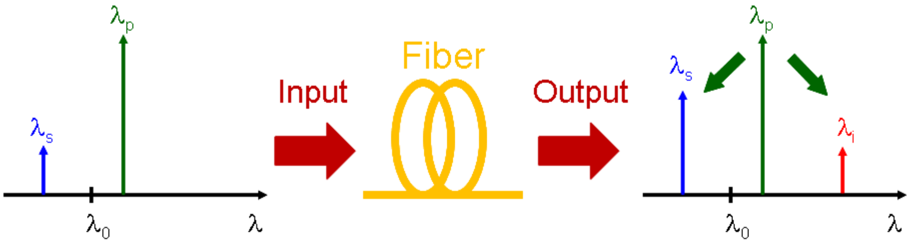

Fig. 7.1 Single-pump fiber optical parametric amplifier (FOPA) with pump positioned at anomalous dispersion region.

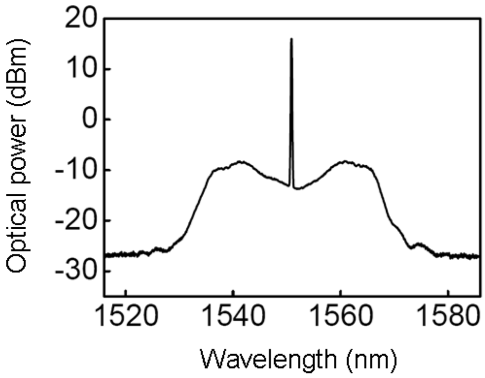

Fig. 7.2 A typical gain spectrum in a single-pump FOPA with pump positioned at 1551 nm. λ_0 of the fiber is 1549 nm and the pump power is 26 dBm.

Unlike the Raman amplifiers and EDFA, the parametric process in a fiber is based on highly efficient FWM rather than energy transitions between energy states. Thus, it results in a flat gain over a wide spectral range [1]. In the previous paragraphs, the FOPA gain we discussed is independent of the initial relative phase difference among the interacting fields, which is referred to as phase-insensitive amplification (PIA). Due to the phase matching condition, the FOPA gain can also be dependent on the initial relative phase difference, and it is known as phase-sensitive parametric amplification (PSA). During PSA, components with the same phase as the signal are amplified, while those with the opposite phase experience no gain. The most important application of PSA is to achieve in-line amplification with an ideal noise figure of 0 dB [1]. As a comparison, for standard phase-insensitive amplifiers or a conventional FOPA, its quantum limited noise figure is 3 dB. Although PSA has lower noise figure, its stringent requirement of the phase relationship among all involved optical fields complicates its implementation compared to that of a conventional FOPA. In this chapter, we mainly focus on the phase-insensitive FOPA which offers high gain, optional wavelength conversion, tunable gain region at an arbitrary wavelength and fast response for ultrafast optical signal processing. The applications of FOPA include in-line amplification [11], [12], return-to-zero (RZ)-pulse generation [13], optical time-division demultiplexing (O-TDM) [14, 15], transparent wavelength conversion [16, 17], all-optical limiters [14, 18], and all-optical sampling [19].

7.2 Dynamic Gain Profile in FOPA Assisted by Gain-Transparent SBS

Although the FOPA has many advantages over other optical amplifiers, its gain performance is often limited by phase mismatch of the interplaying fields. To enhance the FOPA gain, many techniques have been proposed including periodic insertions of single mode fibers [20], adopting dual-pump FOPA [21, 22] and insertions of fiber Bragg gratings (FBGs) [23, 24]. Unfortunately, the technique in [20] has limited gain flatness and dual-pump FOPA requires a higher cost. Although periodic insertions of FBGs can provide a flat and broad gain [23], the gain profile of the FOPA is fixed once the passive devices are deployed. Thus, the technique cannot offer the flexibility in operation. In certain applications, a flexible gain profile in a FOPA can be desirable such that one may choose the optimal profile according to the specific requirements. In this section, we propose and experimentally demonstrate the use of gain-transparent SBS to control the relative phase difference among the interacting fields, thus achieving dynamic gain profiles in a FOPA.

7.2.1 Principle and Experimental Setup

Ref [1], [25], and [27] describe the general SBS and FWM interaction process and show how the index change due to SBS is used to control phase-matching in FWM. This is also described in Chapter 6. As OPA is a FWM process, the signal gain is also determined by the phase-matching condition. It should be noted that the real part of the Brillouin gain contributes to signal amplification and hence will result in a nonlinear phase term that disturbs the phase-matching condition. To achieve dynamic gain profile in a FOPA entirely through the control of phase-matching by SBS induced refractive index change, it is important not to disturb the initial parameters of the FOPA (initial powers of OPA pump and signal). Otherwise, the gain cannot be measured under the same initial conditions. This is the reason why we apply gain-transparent SBS for phase-matching control.

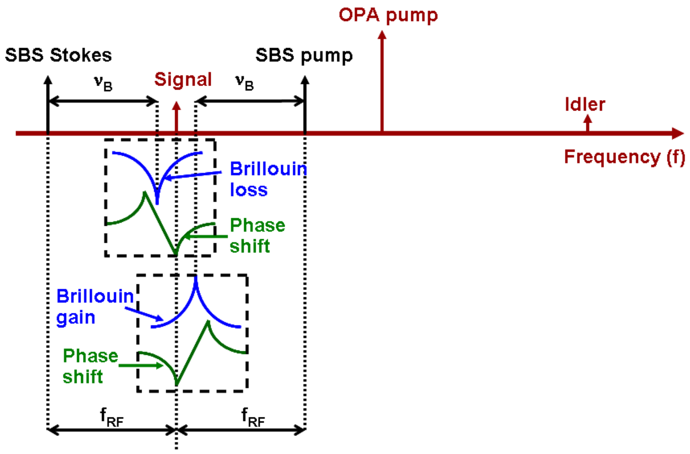

Fig. 7.3 Principle of achieving dynamic gain profile using gain-transparent SBS in a FOPA. ν_B *: Brillouin frequency shift;* f_{RF}*: frequency spacing between SBS pump and signal, and between signal and SBS Stokes wave.*

The principle of our scheme is illustrated in Fig. 7.3. Here, f_{RF} is the frequency spacing between the SBS pump and the signal, and between the signal and the SBS Stokes wave. The signal and the OPA pump co-propagate in an optical fiber and generate an idler wavelength. At the same time, the SBS pump and Stokes waves are launched into the same fiber from the opposite end. Consequently, both optical gain and loss are introduced on the signal by the counter-propagating SBS pump and Stokes waves, respectively. The SBS gain and loss cancel each other, while the phase shifts add up to strengthen SBS induced index change. The total phase mismatch in a FOPA under gain-transparent SBS can be expressed by the following equation:

$$\kappa = \Delta\beta + 2\gamma \overline{P}_{OPA} \pm |\, \mathrm{Im}[g_b(\delta)]\overline{P}_{SBS} / A_{eff} \,| \qquad (7\text{-}1)$$

where $\Delta\beta = \beta_2(\omega_{OPA} - \omega_s)^2$ is the linear phase mismatch with β_2 being the dispersion parameter, ω_{OPA} and ω_s being the frequencies of the OPA pump and the signal, $\overline{P}_{OPA}$ and $\overline{P}_{SBS}$ are the average powers of the OPA and SBS pumps, respectively. $\mathrm{Im}[g_b(\delta)]$ is the imaginary part of the complex Brillouin gain with δ as the normalized frequency detuning, and A_{eff} is the effective mode area of the fiber core. The first two terms in Equation (7-1) remain unchanged once the initial parameters of the OPA process are chosen. The last term represents the SBS induced phase mismatch and can be adjusted by tuning the frequency spacing f_{RF}. Therefore, one can improve/deteriorate the phase-matching condition to maximize/minimize the gain without affecting the initial power of the signal, leading to dynamic control of the gain profile in a FOPA. Moreover, one can easily synthesize any shape of the gain profile in a FOPA through this technique.

Our experimental setup is shown in Fig. 7.4. The output of a tunable laser (TL1) is split into two branches. The upper branch serves as the signal with a power of – 11 dBm. The lower branch is modulated by an EOM biased to suppress the optical carrier and driven at a frequency f_{RF}. The carrier suppression ratio is 23 dB. The two sidebands act as the SBS pump and Stokes waves after amplification by an EDFA. An OPA pump is provided by phase modulation of another tunable laser (TL2) using 10 Gbit/s pseudorandom binary sequence (PRBS) data to increase the SBS threshold [28]. The signal together with the OPA pump are directed to a 1 km highly nonlinear fiber (HNLF) where OPA process takes place in the presence of the counter-propagating SBS pump and Stokes waves. The OPA spectrum is measured by an optical spectrum analyzer (OSA). The HNLF has a nonlinear coefficient of

11.7/(W·km), a zero-dispersion wavelength of 1549 nm, a dispersion coefficient of 0.02 ps/(nm·km), and a dispersion slope of 0.019 ps/(nm^2·km) at ~1550 nm.

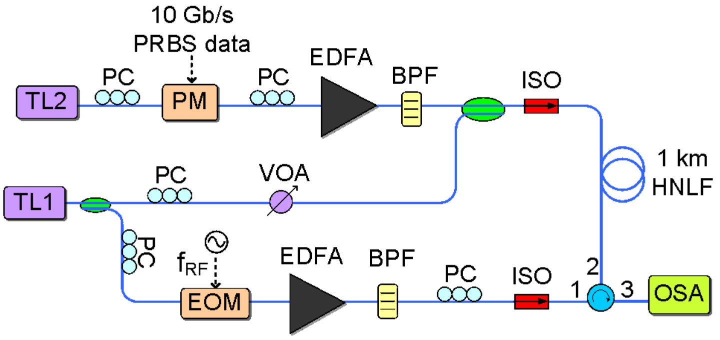

Fig. 7.4 Experimental setup. TL, tunable laser; PM, phase modulator; EOM, electro-optic intensity modulator; EDFA, erbium-doped fiber amplifier; PC, polarization controller; VOA, variable optical attenuator; HNLF, highly nonlinear fiber; BPF, bandpass filter; ISO, isolator; OSA, optical spectrum analyzer; PRBS, pseudorandom binary sequence.

7.2.2 Results and Discussion

The OPA pump wavelength is first set to 1551 nm with a power of 25 dBm. At the beginning, the SBS pump and Stokes waves are turned off. The dark squares in Fig. 7.5 (a) are the measured data points showing a typical M-shaped FOPA gain profile. Table 7.1 lists the measured gain values at four different signal wavelengths (two located close to OPA pump wavelength and the other two located near gain peaks). The two peak gains are achieved at 1540 and 1562 nm where the initial OPA processes are nearly phase-matched. Next, SBS pump and Stokes waves are applied to the setup. The total power is 12 dBm. The signal wavelength is first set to 1561 nm to investigate the influence of the RF frequency. The result is plotted with blue squares in Fig. 7.5 (b). Each RF driving frequency results in a different SBS induced phase term, thus allowing dynamical control of the OPA gain. A maximum gain of 13.31 dB is achieved at a driving frequency f_{RF} =9.584 GHz while a minimum gain of 9.29 dB is obtained at f_{RF} =9.532 GHz. To verify Brillouin gain-transparent operation, the RF frequency dependence of the signal power in the absence of OPA pump is monitored by an OSA. The power variation in Fig. 7.5 (b) is within 1 dB, confirming nearly gain-transparent operation. The slight variation may originate from non-perfect Lorentzian lineshape of the Brillouin gain, resulting in non-ideal

Table 7.1: OPA gains with and without SBS phase control at four different signal wavelengths

Signal wavelength (nm)	Gain (dB)		
	W/O SBS	W/ SBS MAX	W/ SBS MIN
1540	12.03	12.51	9.81
1549	8.84	12.26	4.76
1553	8.96	12.47	5.08
1562	12.86	13.32	9.77

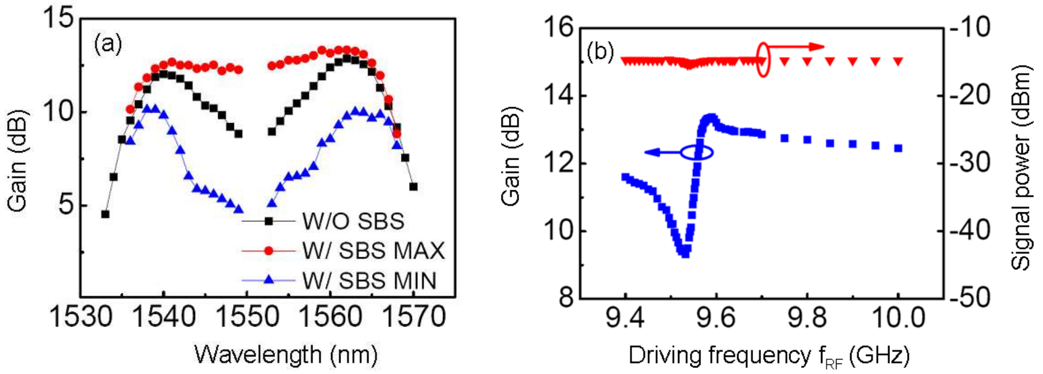

Fig. 7.5 (a) Measured FOPA gain profiles without SBS (W/O SBS), with gain-transparent SBS for maximum gain (W/ SBS MAX) and minimum gain (W/ SBS MIN); (b) OPA gain and signal power (in the absence of OPA pump) as a function of the RF driving frequency f_{RF} at a signal wavelength of 1561 nm. The OPA pump wavelength is 1551 nm.

compensation of SBS gain and loss [29]. Next, we tune the signal wavelength. The driving frequency f_{RF} is adjusted correspondingly for each signal wavelength to obtain both the maximum and the minimum gain. The measured gain profiles under are depicted as red dots and blue triangles in Fig. 7.5 (a). The corresponding gain values at four signal wavelengths are given in Table 7.1. Compared to the OPA gain without SBS at 1540 and 1562 nm, the maximum gain under gain-transparent SBS control leads to slight enhancement of ~0.5 dB due to the aforementioned initial phase-matched OPA processes. Instead, at the signal wavelengths of 1549 and 1553 nm, the maximum gain shows more than 3 dB enhancement. This is because the initial OPA processes at 1549 and 1553 nm are far from phase-matched and the gain-transparent SBS induced phase mismatch helps to re-establish the nearly phase-matched condition. Therefore, the maximum gains at 1549 and 1553 nm can reach a level comparable to those at 1540 and 1562 nm. Similar to the case at 1549 and 1553 nm, the maximum gains at other wavelengths between 1540 and 1562 nm have all been enhanced through the phase control, resulting in a maximum gain profile shown by the red dots in Fig. 7.5 (a). Between 1539 and 1563 nm, the maximum gain profile under gain-transparent SBS shows a flattened gain value of 12.76 ± 0.56 dB. Apart from gain enhancement, the gain can also be dynamically reduced to a minimum level through the phase control. The result is demonstrated in Fig. 7.5 (b). The minimum gains at different signal wavelengths form the minimum gain profile, shown by the blue triangles in Fig. 7.5 (a). The result shows a down-shifted M-shaped gain profile and can be understood from the phase mismatch (κ) distribution along the gain profile. We first consider half side of the gain profile from1553 to 1562 nm. Without SBS, κ has a positive peak value at 1553 nm. As the signal wavelength increases, κ gradually decreases to zero at 1562 nm (assume perfect phase matching at 1562 nm). To obtain the minimum gain profile under gain-transparent SBS, κ at each signal wavelength is maximized by adding the same achievable maximum SBS induced phase mismatch term as in Equation (7-1). Although the values of κ are increased, its distribution trend is the same as that without SBS. Therefore, the minimum gain profile also has a "M" shape but the gain values are reduced. Note that beyond 1562 nm, κ is negative without SBS and the corresponding addition in Equation (7-1) should be the same achievable maximum SBS induced phase mismatch, but with the opposite sign. It is worth mentioning that the operating range of our EDFA is between 1535 and 1565 nm. The output power of the EDFA at different wavelengths are different, leading to non-uniform power of the SBS pump and Stokes waves, especially near the edge of the EDFA amplification band.

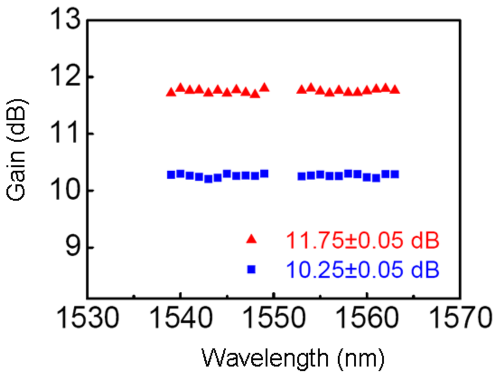

Fig. 7.6 Synthesized FOPA gain profiles at two gain values: 11.75 and 10.25 dB.

As the gain can be dynamically controlled, we can randomly synthesize the shape of the gain profile between the maximum and minimum gain profiles. As an example, Fig. 7.6 shows two synthesized flat gain profiles. The signal wavelength is from 1539 to 1563 nm, and both the gain profiles show flatness with very low ripple (± 0.05 dB).

Additionally, we analyze the effect at a different OPA pump wavelength of 1560 nm in which case the gain bandwidth is reduced and the M-shaped profile is deepened.

Table 7.2: OPA gains with and without SBS phase control at four different signal wavelengths

Signal wavelength (nm)	Gain (dB)		
	W/O SBS	W/ SBS MAX	W/ SBS MIN
1555	9.61	9.37	7.69
1558	7.09	9.25	1.52
1562	7.27	9.17	2.34
1565	9.65	9.34	8.03

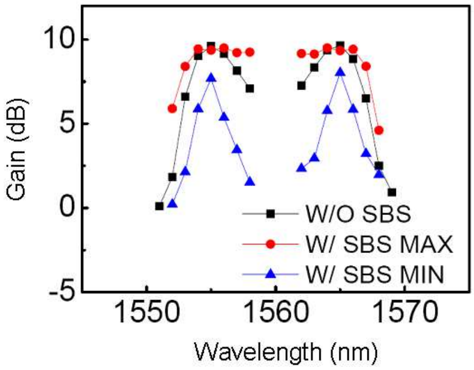

Fig. 7.7 Measured FOPA gain profiles without SBS (W/O SBS), with gain-transparent SBS for maximum gain (W/ SBS MAX) and minimum gain (W/ SBS MIN). The OPA pump wavelength is 1560 nm.

The FOPA gain profiles without SBS and with gain-transparent SBS for maximum and minimum gains are measured. The OPA pump power and input signal power are 22 dBm and – 11 dBm, respectively. The total power of the SBS pump and Stokes waves is 12 dBm. The results are plotted in Fig. 7.7. The gain values at four different signal wavelengths are summarized in Table 7.2. Under gain-transparent SBS phase control, the maximum gain profile shows a gain of 9.32±0.19 dB from 1554 to

1566 nm while the minimum gain profile maintains the conventional “M” shape. Again, the dynamic gain profile offers the flexibility to easily synthesize the gain shape. Moreover, the gain enhancement at the left edge of the maximum gain profile is larger than 4 dB (within EDFA amplification band), implying that the OPA gain bandwidth can be potentially enlarged through our scheme of phase-matching control.

For applications where the signal contains high-speed communication data, the SBS pump and Stokes waves can be introduced on the OPA pump. Effectiveness of the scheme has been examined in our recent work [27]. For multi-channel operation, it is difficult to achieve almost the same gain simultaneously for all the channels as the required optimal SBS induced phase mismatch are different for different signal-pump spacings. To solve this problem, multiple pairs of SBS pump and Stokes waves can be used to control the phase-matching condition for each channel independently. But if communication data are carried on the channels, a compromise can be made in optimization by targeting for the maximum number of channels with almost the same gain. Furthermore, our technique is also applicable for phase-control in dual-pump FOPAs and phase-sensitive amplifiers.

In conclusion, we propose the use of gain-transparent SBS to control the phase-matching condition in OPA process and have experimentally achieved dynamic gain profiles in a single-pump FOPA. The FOPA gain can be dynamically enhanced/suppressed to realize maximum/minimum gain profiles without affecting the initial signal power. The technique provides flexibility in randomly synthesizing the gain profile between the maximum and minimum gain profiles. A synthesized flat gain profile is attained with ± 0.05 dB variation over 24 nm.

References

[1] J. Hansryd, P. A. Andrekson, M. Westlund, J. Li, and P. Hedekvist, “Fiber-Based Optical Parametric Amplifiers and Their Applications,” IEEE Journal of Quan. Electron., vol. 8, no. 3, pp. 506–520 (2002).

[2] M. E. Marhic, K. Y. Wong, and L. G. Kazovsky, “Wide-Band Tuning of the Gain Spectra of One-Pump Fiber Optical Parametric Amplifiers,” IEEE Journal of Quan. Electron., vol. 10, no. 5, pp. 1133–1141 (2004).

[3] T. Torounidis, P. A. Andrekson, and B. Olsson, “Fiber-Optical Parametric Amplifier With 70-dB Gain,” IEEE Photon. Technol. Lett., vol. 18, no. 1, pp. 1194-1196 (2006).

[4] Z. Tong, C. Lundström, P. A. Andrekson, C. J. McKinstrie, *et al.*, “Towards ultrasensitive optical links enabled by low-noise phase-sensitive amplifiers,” Nature Photon., vol. 5, pp. 430–436 (2011).

[5] N. E. Dahdah, D. S. Govan, M. Jamshidifar, N. J. Doran, and M. E. Marhic, “Fiber Optical Parametric Amplifier Performance in a 1-Tb/s DWDM Communication System,” IEEE J. Sel. Topics Quantum Electron., vol. 18, no. 2, pp. 950–957 (2012).

[6] D. Dahan and G. Eisenstein, “Tunable all optical delay via slow and fast light propagation in a Raman assisted fiber optical parametric amplifier: a route to all optical buffering,” Opt. Express, vol. 13, no. 16, pp. 6234–6249 (2005).

[7] R. Slavík, F. Parmigiani, J. Kakande, C. Lundström, *et al.*, “All-optical phase and amplitude regenerator for next-generation telecommunications systems,” Nature Photon., vol. 4, pp. 690–695 (2010).

[8] C. Zhang, X. Wang, X. Xu, P. Chui, and K. Y. Wong, "Simultaneous Demultiplexing of OTDM Channels Based on Swept-Pump Fiber-Optical Parametric Amplifier," in Proc. OFC/NFOEC 2012, Los Angeles, March 2012, paper OM3B.2.

[9] M. E. Marhic, *Fiber optical parametric amplifiers, oscillators and related devices*, Cambridge Univ. Press, 2008.

[10] M. E. Marhic, N. Kagi, T. K. Chiang, L. G. Kazovsky, "Broadband fiber optical parametric amplifiers," "Experimental study on noise characteristics of a gain-saturated fiber optical parametric amplifier," Opt. Lett., vol. 21, pp. 573–575 (1996).

[11] F. S. Yang, M. E. Marhic, and L. G. Kazovsky, "CW fiber optical parametric amplifier with net gain and wavelength conversion efficiency>1," Electron. Lett., vol. 32, pp. 2336–2338 (1996).

[12] J. Hansryd and P. A. Andrekson, "Broad-band continuous-wave-pumped fiber optical parametric amplifier with 49-dB gain and wavelength-conversion efficiency," IEEE Photon. Technol. Lett., vol. 13, pp. 194–196 (2001).

[13] J. Hansryd and P. A. Andrekson, "Wavelength tunable 40 GHz pulse source based on fiber optical parametric amplifier," Electron. Lett., vol. 37, pp. 584–585 (2001).

[14] P. O. Hedekvist, M. Karlsson, and P. A. Andrekson, "Fiber four-wave mixing demultiplexing with inherent parametric amplification," J. Lightw. Technol., vol. 15, pp. 2051–2058 (1997).

[15] J. Hansryd and P. A. Andrekson, "O-TDM demultiplexer with 40 dB gain based on a fiber optical parametric amplifier," IEEE Photon. Technol. Lett., vol. 13, pp. 732–734 (2001).

[16] M.-C. Ho, K. Uesaka, M. E. Marhic, Y. Akasaka, and L. G. Kazovsky, “200-nm-bandwidth fiber optical amplifier combining parametric and raman gain,” J. Lightw. Technol., vol. 19, pp. 977–981 (2001).

[17] M. Westlund, J. Hansryd, P. A. Andrekson, and S. N. Knudsen, “Transparent wavelength conversion in fiber with 24 nm pump tuning range,” Electron. Lett., vol. 38, pp. 85–86 (2002).

[18] W. Imajuku, A. Takada, and Y.Yamabayashi, “Amplitude noise suppression using a high gain phase sensitive amplifier as a limiting amplifier,” Electron. Lett., vol. 32, pp. 677–679 (1996).

[19] J. Li, J. Hansryd, P.-O. Hedekvist, P. A. Andrekson, and S. N. Knudsen, “300 Gbit/s eye-diagram measurement by optical sampling using fiber based parametric amplification,” Optical Fiber Communication Conf. and Exhibit, vol. 4, 2001.

[20] J. Kim, Ö. Boyraz, J. H. Lim, and M.N. Islam, “Gain Enhancement in Cascaded Fiber Parametric Amplifier with Quasi-Phase Matching: Theory and Experiment,” IEEE J. Lightw. Technol., vol. 19, no. 2, pp. 247–251 (2001).

[21] S. Radic, C. J. McKinstrie, R. M. Jopson, J. C. Centanni, Q. Lin and G. P. Agrawal, “Record performance of parametric amplifier constructed with highly nonlinear fibre,” Electron. Lett., vol. 39, no. 11, pp. 838-839 (2003).

[22] J. M. C. Boggio, J. D. Marconi, and H. L. Fragnito, “Double-Pumped Fiber Optical Parametric Amplifier With Flat Gain Over 47-nm Bandwidth Using a Conventional Dispersion-Shifted Fiber,” IEEE Photon. Technol. Lett., vol. 17, no. 9, pp. 1842-1844 (2005).

[23] S. Takasaka, Y. Mimura, M. Takahashi, R. Sugizaki, and H. Ogoshi, “Flat and Broad Amplification by Quasi-Phase-Matched Fiber Optical Parametric

Amplifier," in Proc. OFC/NFOEC 2012, Los Angeles, March 2012, paper OTh1C.4.

[24] H. Zhu, B. Luo, W. Pan, L. Yan, S. Xiang, and K. Wen, "Gain enhancement of fiber optical parametric amplifier via introducing phase-shifted fiber Bragg grating for phase matching," J. Opt. Soc. Am. B, vol. 29, no. 6, 1497–1502, (2012).

[25] E. Mateo, F. Yaman, and G. Li, "Control of four-wave mixing phase-matching condition using the Brillouin slow-light effect in fibers," Opt. Lett., vol. 33, no. 5, pp. 488–390 (2008).

[26] L. Wang, and C. Shu, "Four-wave mixing bandwidth enlargement using phase-matching control by gain-transparent stimulated Brillouin scattering," in Photonics in Switching Conference, Ajaccio-Corsica, France, September 2012, postdeadline paper 2.

[27] L. Wang, and C. Shu, "Dynamic Control of Phase Matching in Four-Wave Mixing Wavelength Conversion of Amplitude- and Phase- Modulated Signals," IEEE J. Lightw. Technol., vol. 31, no. 9, pp. 1468–1474 (2013).

[28] A. Mussot, A. Durécu-Legrand, E. Lantz, C. Simonneau, D. Bayart, H. Maillotte, and T. Sylvestre, "Impact of Pump Phase Modulation on the Gain of Fiber Optical Parametric Amplifier," IEEE Photon. Technol. Lett., vol. 16, no. 5, pp. 1289-1291 (2004).

[29] A. Loayssa, and F. J. Lahoz, "Broad-band RF photonic phase shifter based on stimulated Brillouin scattering and single-sideband modulation," IEEE Photon. Technol. Lett., vol. 18, no. 1, pp. 208-210 (2006).

8 THESIS SUMMARY AND FUTURE WORK

In the previous chapters, we presented our studies on all-optical signal processing using stimulated Brillouin scattering for fiber-optic communications and sensing. In this chapter, a brief summary of the thesis is given in Section 8.1. Some related future work is suggested in Section 8.2.

8.1 Summary

This thesis focuses on all-optical signal processing for optical communications and sensing. The research is mainly based on the effect of stimulated Brillouin scattering in optical fibers. In Chapter 1, an overview of optical signal processing is given. The emergence of various new optical devices and components allows optical signal processing to be readily implemented for both optical communications and sensing.

In Chapter 2, the effect of stimulated Brillouin scattering (SBS) in optical fibers has been discussed. The study includes its physical mechanism, the formulation of the coupled equations governing the phenomenon under steady-state conditions, the Brillouin gain and the threshold of Brillouin scattering in optical fibers.

In Chapter 3, we demonstrate a technique to simultaneously generate multiple delayed signals through four-wave mixing wavelength multicasting in a single-pump SBS based slow light system. The signal delay is achieved with a SBS pump while at the same time the delay is transferred to six other channels by three FWM pumps employed for wavelength multicasting. The time delay performance of the multicasting channels is almost identical to that of the original signal. The maximum delay achieved is about 20 ns, and the maximum delay difference among the channels is 0.89 ns. This slow light multicasting technique may find applications in parallel optical information processing such as simultaneous multichannel synchronization and time division multiplexing.

In Chapter 4, we propose and experimentally demonstrate a new method for temperature sensing using SBS based slow light. The approach relies on temperature dependence of the Brillouin frequency shift in a fiber, hence the time delay of an input probe pulse. By measuring the delay, temperature sensing is realized. We achieve temperature measurement in a 100 m single mode fiber using a CW pump. The main temperature sensing range is ~18 ^{o}C from the room temperature, limited by the SBS gain bandwidth. To apply the technique for measurement of a shorter fiber segment, a pulsed pump is used to introduce SBS slow light. Temperature sensing is achieved in a 2 m SMF with a main sensing range of around ~25 ^{o}C. The scheme is easily implemented, exhibits a relatively high temperature sensitivity with a resolution a resolution of 0.6 to 0.7 ^{o}C depending on the pump power and configuration, and is potentially applicable for distributed sensing.

In Chapter 5, distributed temperature and strain sensing have been achieved by spatially resolved measurement of the probe time delay resulted from SBS based slow light. The temperature or strain of a particular fiber section can be monitored by setting an appropriate relative delay between the pump and probe pulses. By controlling the relative delay, we have achieved distributed profiling of the temperature or strain along the whole sensing fiber. This scheme provides an alternative way for distributed temperature or strain sensing with the potential of real-time temperature or strain monitoring. A spatial resolution of 15 m and a temperature (strain) resolution of 0.7 ^{o}C (13 $\mu\varepsilon$) are obtained. Possible solutions for the enhancement of the spatial, temperature and strain resolutions are suggested. Our scheme is simple to realize and is practical for accurate monitoring of the temperature or strain.

In Chapter 6, we address the problem of phase matching in FWM wavelength conversion with the use of gain-transparent SBS for phase control. We propose and experimentally demonstrate dynamic enlargement and shrinking of degenerate FWM conversion bandwidth based on gain-transparent SBS in a dispersion-flattened highly nonlinear fiber. By introducing self-compensation of optical gain/loss with SBS pump and Stokes waves, the FWM phase-matching condition and hence the conversion efficiency (CE) can be flexibly controlled through SBS induced refractive index change. The phase difference between the interplaying fields is manipulated by modifying the refractive index through SBS without disturbing the initial parameters of the FWM process. The CE has been experimentally enhanced by up to 9.3 dB for an idler wavelength outside the original conversion bandwidth. The 3-dB bandwidth is enlarged from 11.04 nm to 15.62 nm, resulting in 41% increase from its original value. Then we employ this scheme in wavelength conversion of communication signals. The scheme is first applied to wavelength conversion of 10 Gbit/s NRZ-OOK signal. Its performance on phase-transparent wavelength conversion is subsequently examined using 10 Gbit/s NRZ-DPSK signal. Eye diagrams, FWM spectra and BER performances for the converted signals without SBS, with gain-transparent SBS for maximum CE and for minimum CE are analyzed. In the OOK/DPSK wavelength conversion with gain-transparent SBS, the CE has been reduced by 10.7/11.4 dB at a signal-pump spectral spacing of 1.9/1.94 nm; while it has been enhanced by 8.8/7.4 dB at a signal-pump spectral spacing of 4.1/4.07 nm. The pronounced enhancement of the CE at large signal-pump spectral spacing results in enlargement of the 3-dB FWM conversion bandwidth. Limitations in the extent of bandwidth enlargement and noise performance are discussed. Potential use of the scheme in other applications is also described. To further explore the applications of this scheme, we experimentally demonstrate all-optical manipulation of non-degenerate FWM conversion bandwidth based on phase-matching control through gain-transparent SBS. The 3-dB conversion bandwidth reaches a value of 26 nm in the case of maximum CE, corresponding to 44% increase from the original value; while it becomes 15 nm in the case of minimum CE. The CE profile can be potentially and randomly synthesized, resulting in a large tunability in manipulating the bandwidth, which is useful in satisfying different requirements. The practical application of the manipulation of bandwidth is demonstrated by the wavelength conversion of 10 Gbit/s NRZ-OOK signal. Apart from polarization-sensitive wavelength conversion mentioned above, we also investigate the performance of dual-orthogonal-pump FWM on simultaneously achieving both polarization-insensitive and wideband wavelength conversion assisted by the gain-transparent SBS. The gain-transparent SBS is used to control the optical phase of the FWM pump for wideband wavelength conversion. The experimental results show the polarization-insensitive property is well preserved under gain-transparent SBS processing, and only 0.5 dB output power variation of the converted idler is observed. A CE enhancement of 5.1 dB through the phase control at large signal-pump spectral spacing greatly support the potential of this scheme in wideband wavelength conversion. With the phase control, simultaneous polarization-insensitive and wideband wavelength conversion is also feasible in configurations using two co-polarized pumps or a polarization diversity loop. Finally we demonstrate for the first time the extension of the maximum optical delay from a delay line based on FWM wavelength conversion and group velocity dispersion. The FWM bandwidth is enlarged and hence the maximum delay is extended through dynamic phase control by gain-transparent SBS. The maximum achievable delay is increased from 248 ps to 340 ps, a 37% increase from the conventional approach without SBS processing. The technique is applicable in other configurations of tunable delay line based on fiber parametric process and group velocity dispersion.

In Chapter 7, we demonstrate dynamic control of the gain profile in a single-pump fiber optical parametric amplifier (FOPA) assisted by gain-transparent SBS. The FOPA gain can be enhanced/reduced through controlling the phase-matching condition without disturbing the initial parameters of the FOPA. Both the maximum and minimum gain profiles are obtained, offering operational flexibility in randomly synthesizing the profile to satisfy different requirements. Our synthesis can turn the conventional M-shaped profile into spectrally flat gain with ± 0.05 dB ripples over 24 nm. This scheme can be potentially applied to dual-pump FOPA and can benefit other applications of parametric processes.

8.2 Future Work

To improve the performance of the work described in the previous chapters, we have made the following suggestions for future work:

1. In Chapter 3, a technique to simultaneously generate multiple delayed signals through four-wave mixing wavelength multicasting in a single-pump SBS based slow light system is demonstrated. However, in our demonstration the signal used is a pulse with a width of tens of ~ns. Usually the communication data contains optical pulses with a width in the order of ~ps and has a bandwidth much larger than that of the intrinsic Brillouin gain. For practical use of the technique for communication data, the linewidth of the FWM pump should be broadened to allow the SBS slow light system to support ~GHz communication data. There are several methods in broadening the pump linewidth [1-4]. Simultaneous multichannel synchronization and time division multiplexing would then be possible by using this technique.

2. In Chapter 4 and 5, the SBS slow-light-based fiber-optic sensor is proposed and employed to monitor the temperature and strain. Although the temperature and strain can be monitored separately, it is difficult to distinguish the effects of the two parameters on the delay time of the optical pulse. In other words, the change of the delay may originate from the strain, the temperature, or both of them. To address this problem, one possible solution is to use two fibers for sensing. One of the fibers is intentionally loosened to eliminate the strain and is used as a reference.

3. In Chapter 6, the phase matching of FWM is controlled by gain-transparent SBS, for applications in degenerate FWM bandwidth enlargement, wavelength conversion of communication signals, all-optical manipulation of non-degenerate FWM bandwidth, enhanced performance of polarization-insensitive wavelength conversion, and extension of the maximum tunable optical delay. The communication signals used in the experiment are 10 Gbit/s NRZ-OOK and NRZ-DPSK data. To upgrade the implementation to a higher data rate operation, signals at 40 Gbit/s or beyond can be adopted. For high spectral efficiency operation, (differential) quadrature phase-shift keying ((D)QPSK) modulation format should be considered. Furthermore, the scheme for polarization-insensitive and wideband wavelength conversion under gain-transparent SBS processing can be applied to polarization multiplexed DQPSK or QPSK signal which is considered as a standard data format for future 100 Gbit/s optical network. In addition to further investigation on the data rate and format, the phase control of multiple FWM pumps instead of single or dual pumps is also possible by simultaneously using multiple pairs of SBS pump and Stokes waves.

4. In Chapter 7, the dynamic control of the gain profile in a single-pump fiber optical parametric amplifier (FOPA) has been realized with the use of gain-transparent SBS. The SBS gain and loss are introduced on the signal. It is relatively easy to achieve as the signal is a CW wave. For the case where the signal is communication data, it is necessary to apply the gain-transparent SBS to the OPA pump. The demonstration for real data amplification in a FOPA assisted by gain-transparent SBS would be a continuing work. The flat gain performance on real data amplification should be studied in the future.

References

[1] M. G. Herráez, K. Y. Song, and L. Thévenaz, “Aibitrary-bandwidth Brillouin slow light in optical fibers,” Opt. Express., vol. 14, no. 4, pp. 1395-1400 (2006).

[2] Z. Zhu, A. M. C. Dawes, D. J. Gauthier, Lin Zhang, and A. E. Willner, “Broadband SBS slow light in an optical Fiber,“ IEEE J. Lightw. Technol., vol. 25, no. 1, pp. 201-206 (2007).

[3] A. Cheng, M. P, Fok, and C. Shu, “Wideband SBS slow light in a single mode fiber using a phase-modulated pump,” in CLEO 2007, Baltimore, MA, May 2007, Paper JWA49.

[4] B. Zhang, L Yan, L. Zhang, and A. E. Willner, “Multichannel SBS slow light using spectrally sliced incoherent pumping,” IEEE J. Lightw. Technol., vol. 26, no. 23, pp. 3763-3769 (2008).

APPENDICES

Appendix A. List of Publications

Journal papers

1. **L. Wang**, and C. Shu, “Dynamic Control of Phase Matching in Four-Wave Mixing Wavelength Conversion of Amplitude- and Phase- Modulated Signals,” *IEEE J. Lightw. Technol.*, vol. 31, no. 9, pp. 1468-1474, May 2013.
2. **L. Wang**, Y. Chen, H. K. Tsang, and C. Shu, “Generation of Multichannel Delayed Pulses by Four-Wave-Mixing-Assisted Stimulated Brillouin Scattering Slow-Light System,” *IEEE Photonics Journal*, vol. 4, no. 4, pp. 1203-1211, August 2012.
3. **L. Wang**, and C. Shu, “Demonstration of Distributed Strain Sensing with the Use of Stimulated Brillouin Scattering Based Slow Light,” *IEEE Photonics Journal*, vol. 3, no. 6, pp. 1164-1170, December 2011.
4. **L. Wang**, Y. Dai, G. K. P. Lei, J. Du, and C. Shu, “All-Optical RZ-to-NRZ and NRZ-to-PRZ Format Conversions Based on Delay-Asymmetric Nonlinear Loop Mirror,” *IEEE Photon. Technol. Lett.*, vol. 23, no. 6, pp. 368-370, March 2011.
5. **L. Wang**, B. Zhou, C. Shu, and S. He, “Stimulated Brillouin scattering slow-light-based fiber-optic temperature sensor,” *Opt. Lett.*, vol. 36, no. 3, pp. 427-429, February 2011.
6. **L. Wang**, and C. Shu, “Dynamic Gain Profile in Fiber Optical Parametric Amplifier by Gain-transparent SBS,” submitted to *IEEE Photon. Technol. Lett.*.
7. K. Xu, **L. Wang**, K. P. Lei, Z. Cheng, Y. Chen, C. Wong, C. Shu, and H. K. Tsang, “Demodulation of 20 Gbaud/s differential quadrature phase-shift keying

signals using wavelength-tunable silicon microring resonators," *Opt. Lett.*, vol. 37, no. 16, pp. 3462-3464, August 2012.

8. K. Xu, H. K. Tsang, G. K. P. Lei, Y. Chen, **L. Wang**, Z. Cheng, X. Chen, and C. Shu, "OSNR Monitoring for NRZ-PSK Signals Using Silicon Waveguide Two-Photon Absorption," *IEEE Photonics Journal*, vol. 3, no. 5, pp. 968-974, October 2011.

Conference papers

1. L. Wang, and C. Shu, "Reconfigurable Fiber Optical Parametric Amplifier Gain Profile by Phase Matching Control with Gain-Transparent SBS," in *Proc. ECOC 2013*, London, UK, September 2013, paper *P.1.5*.
2. **L. Wang**, and C. Shu, "Enhanced Performance of Four-Wave Mixing Wavelength Conversion Through Dynamic Control of Optical Phase," in *Proc. OFC/NFOEC 2013*, Anaheim, CA, USA, March 2013, paper *JW2A.54*;
3. **L. Wang**, and C. Shu, "Four-wave mixing bandwidth enlargement using phase-matching control by gain-transparent stimulated Brillouin scattering," in *PHOTONICS IN SWITCHING CONFERENCE*, Ajaccio-Corsica, France, September 2012, **Postdeadline** paper 2.
4. **L. Wang**, and C. Shu, "Distributed Fiber Strain Sensor Using Stimulated Brillouin Scattering Based Slow Light," *IEEE Photonics Conference 2011*, Arlington, Virginia, USA, Oct. 2011, paper *ThEE 4*;
5. **L. Wang**, Y. Dai, G. K. P. Lei, Jiangbing Du, and C. Shu, "Delay-Asymmetric Nonlinear Loop Mirror for Bit-Rate Variable RZ-to-NRZ Format Conversion," in *Proc. OFC/NFOEC 2011*, Los Angeles, CA, USA, Mar. 2011, paper *JWA035*;
6. **L. Wang**, B. Zhou, C. Shu, and S. He, "Temperature Sensing Using Stimulated

Brillouin Scattering Based Slow Light," *Asia Communications & Photonics Conference & Exhibition (ACP 2010)*, Shanghai, China, Dec. 2010, paper *FS6*;

Invited Presentation

1. C. Shu, and ***L. Wang***, "Wavelength-Transparent Stimulated Brillouin Scattering Slow Light and its Applications in Fiber Sensing," *The 4th International Photonics and OptoElectronics Meetings (POEM2011)*, Wuhan, China, Nov. 2011, paper *OCSN-5*.

Appendix B. List of Figures